

# Experimental study and modelling of AC characteristics of Resonant Tunneling Diodes

Vom Fachbereich Elektrotechnik und Informationstechnik  
der Technischen Universität Darmstadt  
zur Erlangung der Würde eines  
Doktor-Ingenieurs (Dr.-Ing.)  
genehmigte

## Dissertation

von M. Tech.

**Dibakar Roy Chowdhury**

geboren am 06.08.1976  
in Burdwan (W.B.), India

Referent: Prof. Dr.-Ing. Peter Meissner  
Korreferenten: Prof. Dr.-Ing. Hans. L. Hartnagel  
Tag der Einreichung: 18.02.2008  
Tag der mündlichen Prüfung: 23.06.2008

D17  
Darmstädter Dissertation  
Darmstadt 2008



# Acknowledgements

Getting a PhD is a milestone in my life. While working for it for last four and a half years, I came across many people, who had great or little impact on my academic as well on my life. It is not possible to name all of them here but I greatly acknowledge their efforts and contributions in every possible way.

Foremost, I would like to express my sincere gratitude, to my supervisor Dr. Michael Feiginov, for providing me the opportunity to pursue my doctorate under his guidance. I am extremely indebted to him in many ways. First, I would like to thank him for providing me with his constant intellectual support and motivation for the past years. Second, I am grateful to him for his several critical reviews on my thesis draft. The many scientific discussions I had with him, during the course of my PhD, were always helpful to me to clarify my knowledge in the field of solid state electronics. Moreover, his penetrating insight in solving research problems was always a source of motivation for me. I am also grateful to Prof. Peter Meissner for referring my PhD dissertation and staying in constant touch with my research work during the tenure of my PhD. Actually, I consider myself extremely fortunate to have two supervisors who are strict at the same time amiable.

I am thankful to Prof. Hans. L. Hartnagel, for his keen interest in my work and the encouragements.

I would like to thank Dipl.-Ing. Nicole Bogdan for sharing useful time in laboratories and with the computers.

I acknowledge Prof. Duu Sheng Ong, Dr.-Ing. Kabula Mutamba, Dr.-Ing. Jochen Sigmund, Dr.-Ing. Oktay Yilmazaglu, Dr.-Ing. Cezary Sydlo, Dr.-Ing. Oleg Cojocari, Dr.-Ing. Jens Freese for being always there with their help.

I am thankful to Ben, Thorsten, Sandro, Bouba, Ion, Karolina, Sangyon and all other colleagues, with whom I have spent a good time at the Institute. Particularly, the weekly soccer matches and the barbeques were highly enjoying.

I would like to thank Mr. Peter Kiesslich and Mr. Andreas Semrad for helping me with their technical support in the laboratories.

It could had been much better for my research work, if I had spent my all the time on the

thesis but my friends from Dieburg (where I lived for my whole PhD tenure and it may be a world record for longest stay there), ensured that it shouldn't happen. The group consists of Bhuvan, Manoj, Manish, Satish, Kaustav, Sameer, Imran to name a few, was highly enthusiast and I shared lot of lively and joyous moments with them. Apart from them, the various discussions, I had with Ramu, Mazhar and Dr. Sudip Roy were always interesting and stimulating.

Finally, I feel myself blessed to have a family who were there always with their love and affection. I believe, I couldn't be able to finish this dissertation without the continuous inspiration and motivation, which I received from my mother. I am enormously indebted to my parents for whatever little bit, I have achieved in my life till now.

Darmstadt, 18.02.2008

Dibakar Roy Chowdhury



# Abstract

In this thesis work, the small-signal response of the resonant tunneling diode at different frequencies is studied. It has been shown previously that because of the Coulomb interaction, the inherent limitation of the operating frequency and the charge relaxation (response) time of resonant tunneling diode (RTD) is not due to the resonant state lifetime [1], contrary to the general belief [2, 3]. Here we have experimentally shown that intrinsic response time of RTD is different than the resonant state lifetime and the operating frequencies of RTD is limited neither by the resonant state lifetime nor by the intrinsic response time. In fact we have experimentally demonstrated negative differential conductance (NDC) far beyond the resonant state lifetime limit which clearly proves that resonant tunneling exists at frequencies beyond the resonant state lifetime limit. Using the analytically derived equivalent circuit [1], the measured frequency response of the RTD admittances (conductances and susceptances) as well the special features of RTD capacitances at low frequencies are reproduced well. So we have experimentally shown that the proposed simple equivalent circuit for small signal analysis of RTD is correct and appropriate.



# Contents

<b>1</b>	<b>Introduction</b>	<b>1</b>
1.1	RTD working principles and applications . . . . .	1
1.2	Review of earlier works on AC RTD models . . . . .	6
1.3	Research objectives . . . . .	11
1.4	Overview of the work . . . . .	16
1.5	Research results to be defended . . . . .	18
<b>2</b>	<b>Self-consistent simulation of RTD</b>	<b>19</b>
2.1	Existent RTD models . . . . .	19
2.2	Development of the static simulator . . . . .	21
2.2.1	Current density expressions . . . . .	21
2.2.2	Quantum well electron density . . . . .	22
2.2.3	Tunnel transparency of the barriers . . . . .	24
2.2.4	Non-parabolicity effect . . . . .	25
2.2.5	Screening length . . . . .	27
2.2.6	Resonant state level broadening . . . . .	29
2.2.7	Depletion length . . . . .	30
2.2.8	Effect of strain . . . . .	32
2.2.9	Algorithm of the simulator . . . . .	33
2.3	Verification of the developed simulator . . . . .	36
2.3.1	From literatures . . . . .	36
2.3.2	Our studied RTDs . . . . .	41
2.3.3	Simulation of RTD parameters . . . . .	47
2.4	RTD model when emitter and QW electron mass differs . . . . .	49



2.5	Conclusions . . . . .	57
<b>3</b>	<b>Simulation of dynamic behavior of RTD</b>	<b>58</b>
3.1	Introduction to the developed AC model . . . . .	59
3.2	Behavior of low frequency RTD capacitance . . . . .	61
3.2.1	Theoretical analysis . . . . .	61
3.2.2	Comparison with measurement . . . . .	65
3.3	RTD equivalent circuit with backflow of electrons . . . . .	69
3.3.1	Basic equations . . . . .	70
3.3.2	RTD response time . . . . .	73
3.3.3	RTD Admittances . . . . .	75
3.3.4	Effective RTD capacitance at low frequencies . . . . .	76
3.4	Conclusions . . . . .	80
<b>4</b>	<b>Simulation and measurement of RTD admittances</b>	<b>81</b>
4.1	Device design . . . . .	81
4.1.1	Impact of spacers on NDC of RTD . . . . .	85
4.2	Scattering parameter measurements . . . . .	87
4.3	Evaluation of parasitics . . . . .	88
4.3.1	Measurement of parasitics . . . . .	90
4.3.2	Simulation of parasitics . . . . .	94
4.4	Derivation of RTD admittances . . . . .	98
4.5	Comparison of the measured and simulated AC behaviors . . . . .	107
4.6	Microwave measurement of response time . . . . .	110
4.7	Coulomb interaction effect on escape rates . . . . .	110
4.8	RTD power at THz frequencies . . . . .	116
4.9	Conclusion . . . . .	118
<b>5</b>	<b>Concluding Summary and Future Works</b>	<b>120</b>
5.1	Summary of results . . . . .	120
5.2	Future Works . . . . .	122
<b>6</b>	<b>Appendix</b>	<b>123</b>

<i>CONTENTS</i>	III
6.1 Derivation of emitter-well forward current . . . . .	123
6.2 tunneling co-efficient calculation . . . . .	125
6.3 tunneling co-efficient when effective masses are different . . . . .	128
<b>List of Symbols</b>	<b>131</b>
<b>List of Abbreviations</b>	<b>132</b>
<b>Bibliography</b>	<b>133</b>
<b>Own Publications</b>	<b>140</b>



# Chapter 1

## Introduction

### 1.1 RTD working principles and applications

A double barrier resonant tunneling diode (RTD) consists of a quantum well (QW) sandwiched between two barriers and doped emitter and collector layers. The conduction band potential profile of a typical RTD is shown in figure 1.1. Because of the small size (along z-axis in Fig. 1.1) of the quantum well, quasi-bound-states (resonant states) are formed which accommodate the 2 dimensional electron gas (2DEG). The functionality of RTD is obtained by electron transport through the quasi-bound states ( $E_1$  is the bottom of the first subband and  $E_2$  is the bottom of the second subband in Fig. 1.1) formed in the quantum well. In the following subsections the left electrode is considered to be the emitter (cathode) and the right electrode the collector (anode). This means under the applied voltage the electrons are assumed to move from left to right. The electron energies in emitter, well and collector are considered to be distributed according to the Fermi-Dirac statistics. Although a brief and concise description of the physics of resonant tunneling are available in literature [3, 4, 5, 6] but I give here a short introduction of the mechanism of current conduction in RTD. Based on the material system chosen and the width of the quantum well, one or more resonant subband can exist in the well. Fig. (1.1) shows a typical current-voltage characteristic and the corresponding conduction band structure of a typical RTD at different bias points. Two models are proposed for current conduction in RTD and they are called as sequential tunneling model [7] and coherent tunneling model [8].

The principle of current conduction in RTD according to the sequential tunneling is the

following: Under the applied voltage electrons tunnel from the emitter through the left barrier into the quantum well quasi-bound state (resonant state) and lose the phase memory completely and then tunnel through the right side barrier to the collector. So the transport of electrons across the left barrier and across the right barrier are considered to be two separate processes. At zero bias  $U = 0$  V, the tunneling current from left to right is exactly equal to the tunneling current from right to left because of the same Fermi level position at the emitter and collector of RTD. So the net current density across the device is zero (situation - a - in Fig. 1.1). When voltage is applied, the resonant subband in the QW as well as the Fermi level in the collector side lowers down. So the electrons in the emitter side for which the energy and the momentum in the plane of the barriers (these electrons are called as resonant electrons), are conserved with the QW electronic states tunnel to QW. Those electrons tunnel further from QW to the empty states in collector giving rise to net current density through the RTD. Further increase in bias results in more and more emitter states in resonance with QW state so that the conduction current keeps on increasing and gives rise to positive differential (PDC) region. When the resonant subband in the QW is close to the emitter conduction band edge maximum number of emitter states find themselves in resonance hence the current density is maximum (point -b- in Fig. 1.1,  $J_p$  is called as the peak current density and  $U_p$  as the peak voltage). If voltage is increased further the QW resonant subband goes out of resonance and the current starts decreasing giving rise to negative differential conductance (NDC) region. At voltage higher than  $U_v$  (point c) the current density starts building again because of the tunneling through the higher subbands present in the structure.  $U_v$  is called as valley voltage and the corresponding current density as valley current density ( $J_v$ ). If the QW contains two resonant subbands then the RTD current-voltage characteristic can have two local peaks and valleys.

In case of coherent tunneling model, electrons are considered to be incident on the double barrier structure with a finite tunneling co-efficient. The electrons satisfying the conservation of total energy and the momentum in the plane of the barriers, participate in the resonant tunneling. The electrons are considered to be thermally distributed and the tunneling co-efficient is maximum for those electrons whose energy is equal to the resonant state energy. At zero bias (i.e.  $U = 0$  V) the tunneling current from left to right is equal to the tunneling current from right to left. So no net current flows through the structure

(point -a- in Fig. 1.1). When bias is applied the tunneling current through the structure starts to increase because more electrons in the emitter (see the function  $n_E(E)$  vs.  $E$  in Fig. 1.1) found themselves in resonance with the QW resonant state. Close to the emitter conduction band edge the current reaches maximum since the number of incident electrons satisfying resonance condition reaches maximum (point b in Fig. 1.1). With further increase in applied bias the resonant state lowers down than emitter conduction band edge hence the tunneling current starts to drop giving rise to NDC region of the I-V characteristic. At still higher voltages current conduction through RTD builds again through the higher subbands (point c in Fig. 1.1).

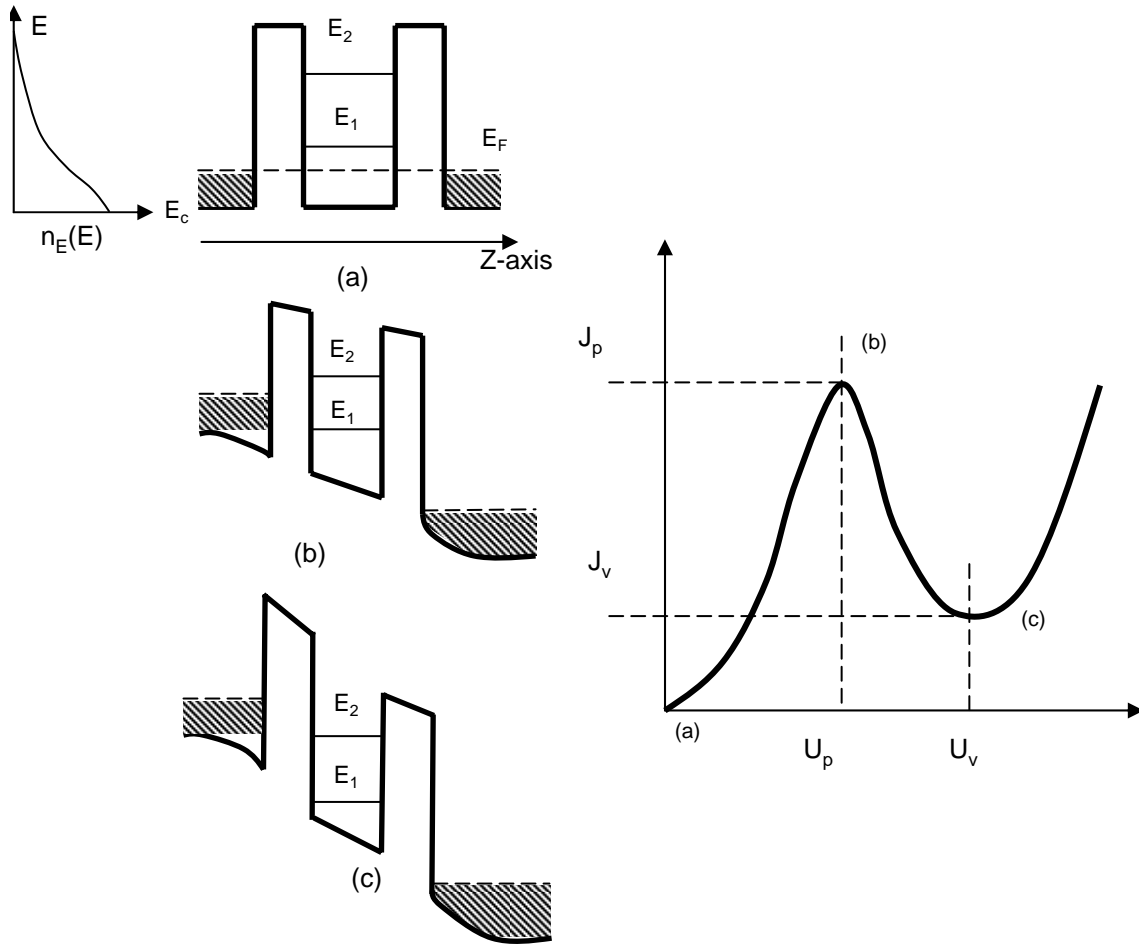


Figure 1.1: Conduction band diagram of RTD at different points of its I-V characteristic. The term  $n_E(E)$  denotes the electron distribution in the emitter, i.e. the multiplication of the density of states in the conduction band of the emitter with the Fermi distribution function of emitter.

Different material systems as GaAs/AlGaAs [9, 10, 11], GaAs/AlAs [12, 13], InGaAs/InAlAs [14, 15] and InGaAs/AlAs [16, 17, 18] are used for the fabrication of intraband RTD. The other variation of double barrier RTD called as interband RTD is achieved by applying the material system InAs/AlSb [19, 20]. In case of intraband RTDs, the mechanism of current conduction is somehow different. The electrons move from emitter to collector through the quantized state in the valence band of the QW (unlike intraband RTD). If bias is increased the tunneling current increases until the resonant state goes down than the emitter conduction band edge. With the further increase in bias the emitter electrons do not find any state in the QW to tunnel so current drops. At some higher voltage the tunneling current starts to rebuild because of the conduction through resonant states in the conduction band of the QW. Figure (1.2) shows a typical band diagram of an interband RTD.

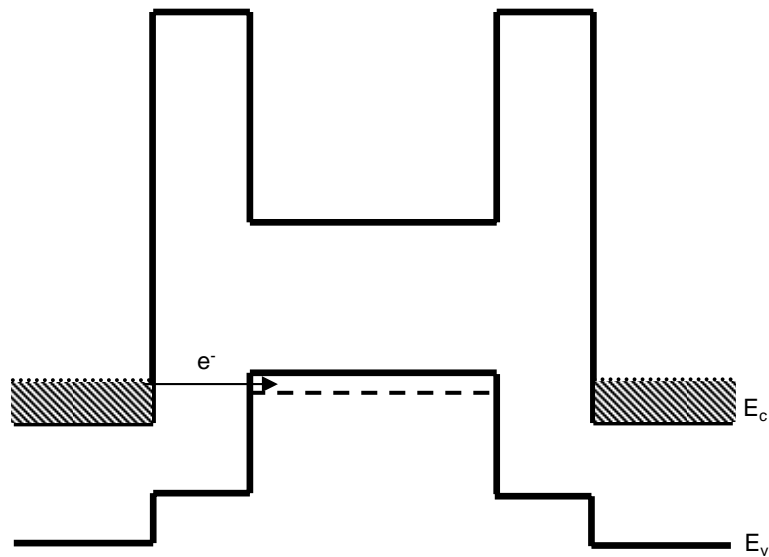


Figure 1.2: Conduction band diagram of a typical interband RTD. The electron transport takes place from emitter to collector via the quantised state in the valence band of the QW. The first interband RTD made of InAs as emitter and collector, AlSb as barrier and GaSb as QW was reported by Söderström et. al. for the first time [19].



RTD can work very fast because of the nanometric device dimensions, fast electron escape rates across the barriers and short RC time constant. The N shaped (Fig. 1.1) current-voltage characteristic (I-V) along with its capability of high speed operation makes it a suitable candidate for various practical applications in the high speed as well as in the functional modes. Because of the high speed of operation along with the presence of NDC in its I-V curve RTD can generate oscillations at very high frequencies when included in a resonant contour (e.g. a RLC circuit). In fact oscillator based on RTD has been demonstrated at sub-millimetre wavelengths in the fundamental [12, 21, 22, 23, 24] as well as in the first harmonic mode [25]. Apart from that the other high speed applications of RTD are frequency multipliers [26, 27] and high speed switch [28, 29, 30]. Because of the strong non-linearity and the anti-symmetry of the I-V characteristic, RTD can generate the odd harmonics [26] without the even harmonics. Rydberg et. al. [27] had reported third harmonic with 1.2 % efficiency at 250 GHz of frequency. Because of the extreme fast response and the presence of NDC characteristic in its I-V, RTD can be used as high speed switch. The best switching time reported from RTD is 1.9 ps [30] till now. The special property of N shaped I-V characteristic allowed RTD to be used as a functional device in binary [31], multiple valued logic circuits [32, 33] as well for memories [34] and even in signal processing [35].

## 1.2 Review of earlier works on AC RTD models

Since the discovery of RTD much work has been done in this field for last three decades. Although the literature on both modeling and experiments are quite large still various open questions are existing related to RTD. Untill now equivalent circuits in several forms are introduced to represent the small signal behaviors of RTD. The simplest equivalent circuit model introduced to represent a double barrier RTD is one with the parallel combination of RTD conductance and capacitance (Fig. 1.3a, this model is used by Orihashi et. al. [24]). The reason this simple model is employed is the following. When bias is applied RTD starts conducting and current flows through the device (Fig. 1.1). At the same time the collector side starts to deplete because of the applied bias. As a result of the applied bias, the conductance  $G_{RTD}$  (due to conduction by RTD) and the capacitance  $C_{RTD}$  (due to depletion of the collector side) appears inside RTD. So intuitively RTD can

be represented by the parallel combination of  $G_{RTD}$  and  $C_{RTD}$  (Fig. 1.3a). But it has been shown experimentally that the real and imaginary parts of RTD admittances (i.e. the measured RTD conductance and capacitance) change with frequency [36, 37, 38], instead of having a constant value. So this simple model is not applicable for RTD although it works very well for many more simple two terminal devices (e.g. varactor, Schottky diode etc.).

The presence of 2DEG in the RTD quantum well suggests that constant conductance and capacitance isn't enough to represent its small signal behaviors. When the applied bias voltage is changed, the current inside RTD takes time to reach the value which corresponds to the changed applied bias. So the conduction current in RTD lags in phase behind the applied voltage which implies RTD should have inductive character. This fact was realized by Gering et. al. [39] for the first time and they introduced an inductance in the RTD equivalent circuit. In their equivalent circuit  $R_s$ ,  $L$ ,  $G_0$  and  $C_{ec}$  are the series resistance, inductance, static or DC conductance and emitter-collector capacitance, respectively (Fig. 1.3b). The parameters  $G_0$  and  $C_{ec}$  are calculated from the static curve and structural parameters of the device, respectively and  $L_s$  is defined by an empirical relationship involving the barrier thicknesses. The same form of the small signal model was employed by Wei et. al. [40] but they considered the connecting bond wires as the origin for the series inductance ( $L_s$ ). So effectively they [40] represented RTD by the simple RC equivalent circuit model.

The fact that voltage leads current inside RTD motivated Brown et. al. [2] to modify the simple GC equivalent circuit by introducing an inductance ( $L$ ) (Fig. 1.3c) in series with the RTD conductance unlike Gering [39] where the inductance is in series with the parallel combination of the RTD conductance and capacitance. Moreover the origin of inductance in Gering's circuit doesn't have any physical background. Brown considered if the applied bias is changed by a step function then the current through RTD needs some time to accommodate the change in bias. The time taken by the RTD current to reach its new value corresponding to the changed applied voltage is nothing but the quasibound state lifetime ( $\tau_d$ ). Since RTD current lags behind the applied voltage so intuitively it is the inductance that should come in series with the RTD conductance. In fact they analytically derived expression for RTD admittance which shows RTD conductance is in series with

the inductance and the whole conductance-inductance combination is in parallel with the RTD capacitance (Fig. 1.3c). According to their derivation the inductance is related to the Nth resonant state lifetime by the following relation  $L = \tau_d/G$ . But their equivalent circuit cannot explain certain experimental results. It has been shown experimentally that RTD capacitance in the positive differential conductance region can be more [41] or less [36] than the emitter-collector ( $C_{ec}$ ) depletion capacitance. But according to Brown's equivalent circuit (Fig. 1.3c), the expression for RTD capacitance is,

$$C_{RTD} = \omega \left[ C_{ec} - \frac{G_0\tau}{1 + (\omega\tau)^2} \right], \quad (1.1)$$

So RTD capacitance is always lesser than emitter-collector capacitance ( $C_{ec}$ ).

In 1989 Sheard et. al. [42] developed another simple equivalent circuit model (Fig. 1.3d) under the sequential tunneling approximation [7] where they represented each barrier of RTD by a parallel RC circuit and then combined them to form the complete equivalent circuit for RTD (Fig. 1.3d). In their derived model they didn't consider the following effects; first, the Coulomb interaction effect of QW charges with the emitter and collector and second, the rate of change of electron escape rates across the barriers with the bias applied on the corresponding barriers. As a result of ignoring these effects, their derived equivalent circuit is much simple and it was decoupled to GC circuit representing each of the barrier (Fig. 1.3d).

Genoe et. al. [43] or Mattia et. al. [36] derived another small signal model (Fig. 1.3e) for RTD based on the theory of sequential tunneling approximation [7]. They considered emitter, well and collector as three different Fermi sea of electrons but each of them are in thermal equilibrium. They established expressions for the current across the emitter-well and well-collector barriers as well as for the quantum well charges. By introducing a small signal excitation on the current and the charge expressions, they derived the small signal equivalent circuit (Fig. 1.3e). Although their equivalent circuit is comprehensive and general but not suitable for analytical analysis and not as simple as like some other circuits [1, 2]. At the same time it is difficult to get an insight on the device operation from their model.

The dynamic model [1, 44] developed in recent past is also based on the sequential tunneling approach (Fig. 1.3f). The important physical effects such as, the current continuity,

charge neutrality, Coulomb interaction effect are taken into account in the model [1, 44]. The only limitation of this model is that it becomes inaccurate at the biases close to the onset of resonant tunneling. Otherwise, the model is valid well in the resonant tunneling regime. The derived equivalent circuit is much simpler and gives a better and clear understanding of RTD operation. In addition to that the model contains only 4 parameters (Fig. 1.3f) whereas the other models [43, 36] contain 7 parameters.

Till now I was describing different dynamic models employed to represent RTD small signal behaviors. Among them some of the models are general and comprehensive [1, 43, 36]. The equivalent circuit derived recently is much simpler [1] than the others [43, 36]. So the question is can the derived simple model [1] correctly represent the small signal AC measurements of RTD? In this work, we have studied the dynamic behaviors of InGaAs/AlAs RTD with the help of the simple equivalent circuit [1] to find the answer.

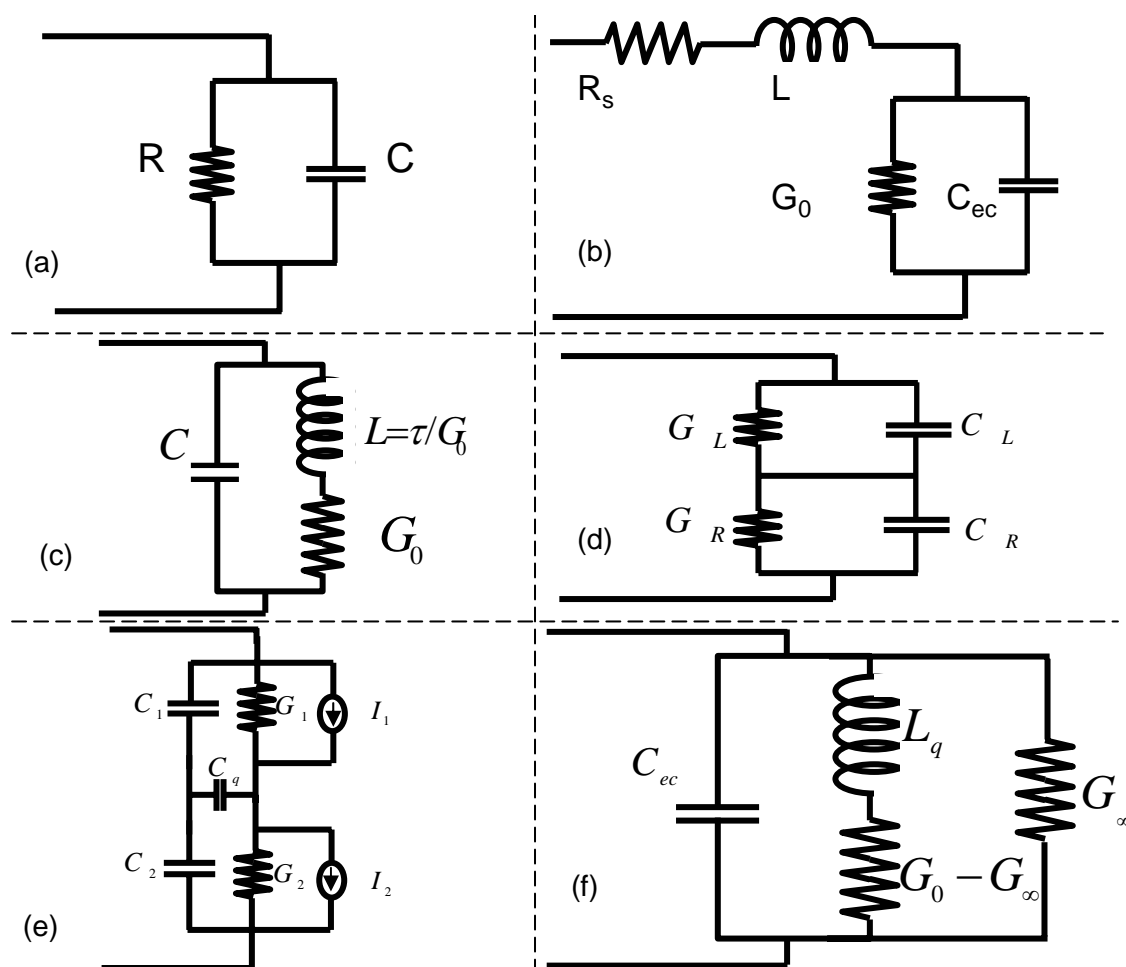


Figure 1.3: (a) simple RC equivalent circuit, (b) RLC equivalent circuit by Gering et. al. [39], (c) RLC equivalent circuit by Brown et. al. [2], (d) equivalent circuit by Sheard and Toomb [42], (e) circuit by Mattia et. al. [36] and (f) Analytically derived equivalent circuit by Feiginov [1]

Another general question related to any electronic device is how fast the device can work and what limits its operation at high frequencies. RTD has shown to work upto the frequency of 3.9 THz in the passive mode of operation [45]. In case of RTD the conduction through the device takes place via the population and depopulation of the two dimensional resonant state in the quantum well. So it is quite normal to assume that the inherent response time of RTD is limited by the lifetime of the resonant state ( $\tau_d$ ) in the QW. Which means the structures are not expected to react when one applies an external perturbation faster than  $\tau_d$ . In that situation (when the external perturbation is faster than  $\tau_d$ ) resonant tunneling should cease to exist [2]. Hence the general perception is RTD cannot respond faster than its quasi-bound-state lifetime [3, 2, 46]. Classically thinking if the externally applied AC bias variation is so fast that QW charges cannot follow (because of the finite lifetime of the electron in the QW) the AC bias then at such a fast bias variation the resonant tunneling current is supposed to be switched off and NDC should vanish. Thus the quasi-bound-state lifetime is supposed to impose the fundamental limitation on the high frequency operation of RTD or in other words RTD cannot able to produce oscillations beyond a certain frequency determined by its quasi-bound state lifetime. As mentioned earlier the highest frequency obtained to date from RTD oscillator is 712 GHz [22] in the fundamental mode. So the question does arise, is it the maximum oscillatory frequency that can be obtained from RTD or can one make RTD to oscillate in the fundamental mode at even higher frequencies?

### 1.3 Research objectives

The main motivation for this thesis work comes from the theoretical results obtained earlier [1, 44, 47]. Our aim in this work is to do the experimental verifications of the published theoretical results [1]. For that purpose we need to design appropriate RTDs so that we can measure them with minimum technical complications using our available laboratory resources.

Theoretically [47] it has been shown that the response time of RTD can be smaller (in PDC region) or larger (in NDC region) than the quasibound state lifetime because of the Coulomb interaction of quantum well electrons with the emitter and collector. The mechanism of Coulomb reduction of RTD response time is illustrated in figure (1.4).

Figures (1.4a - 1.4d) describe response time for the single barrier structure whereas the figures (1.4e - 1.4g) are employed for the double barrier structures. We have defined response time ( $\tau_{resp}$ ) as the time taken by an extra single electron to tunnel out from the quantum well in the presence of Coulomb interaction effect. The Coulomb interaction effect parameter ( $\beta$ ) determines the number of states in the quantum well which are shifted per every additional single electron one puts in the QW (Fig. 1.4). The QW bottom shifts because of the Coulomb interaction of QW charges with the emitter and collector (Fig. 1.4). Hence Coulomb interaction effect changes the number of electrons in the quantum well which are available for tunneling. Now let us explain the charge relaxation mechanism with the help of Figure 1.4. Figure 1.4a defines the situation of the simplest quantum well structure with only one tunnel barrier, here QW resonant state lifetime is  $\tau_d$ . In the stationary-state condition, all the states in the lead and below the Fermi level are filled with electrons (Fig. 1.4b). If we switch the Coulomb interaction between the electrons off ('neutral electron') and move one or  $N$  electrons (marked as square) from the lead to QW, then the electron(s) would occupy one or  $N$  empty states above the Fermi level and it (they) would tunnel out of QW with the time constant  $\tau_d$  (Fig. 1.4c). The leads (for both the cases of single and double barrier) are capable to emit or absorb infinite number of electrons without any change of the position of the respective Fermi levels. Now we switch on the Coulomb interaction, then the bottom of the QW would rise by  $e^2/C$  per every single electron we put into the well. In result, the number of electronic states in QW contributing to the charge relaxation changes by the factor  $\beta$  and  $\tau_{resp}$  becomes equal to  $\tau_d/(1 + \beta)$  (Fig. 1.4d). The important point in figure (1.4d), although  $1 + \beta$  or  $(1 + \beta)N$  states are contributing to the charge relaxation, only 1 or  $N$ , electron(s) have to tunnel out to bring the system to the original stationary-state. Figure 1.4e explains the situation with the biased double barrier resonant tunneling structures. In the absence of Coulomb interaction effect, the relaxation of an additional electron in the QW would be determined by the corresponding resonant state lifetime of the double-barrier structure (Fig. 1.4f). When the Coulomb interaction is switched on, then  $\tau_{resp}$  decreases significantly: the upward shift of QW bottom blocks tunneling of electron from emitter to QW and hence accelerates the charge relaxation (Fig. 1.4g).

Quantitatively the factor  $\beta$  makes response time different than the resonant state lifetime. In PDC region  $\beta$  is positive and can be expressed as  $\beta = e^2\rho_{2D}/C$ .  $\rho_{2D}$  is the 2 dimensional

density of states in the QW and  $C$  is the capacitance of QW with emitter and collector. In the NDC region the expression for  $\beta$  is much complicated and it reduces to negative values [1, 47]. In chapter 4, I have explained the quantitative nature of  $\beta$  more elaborately.

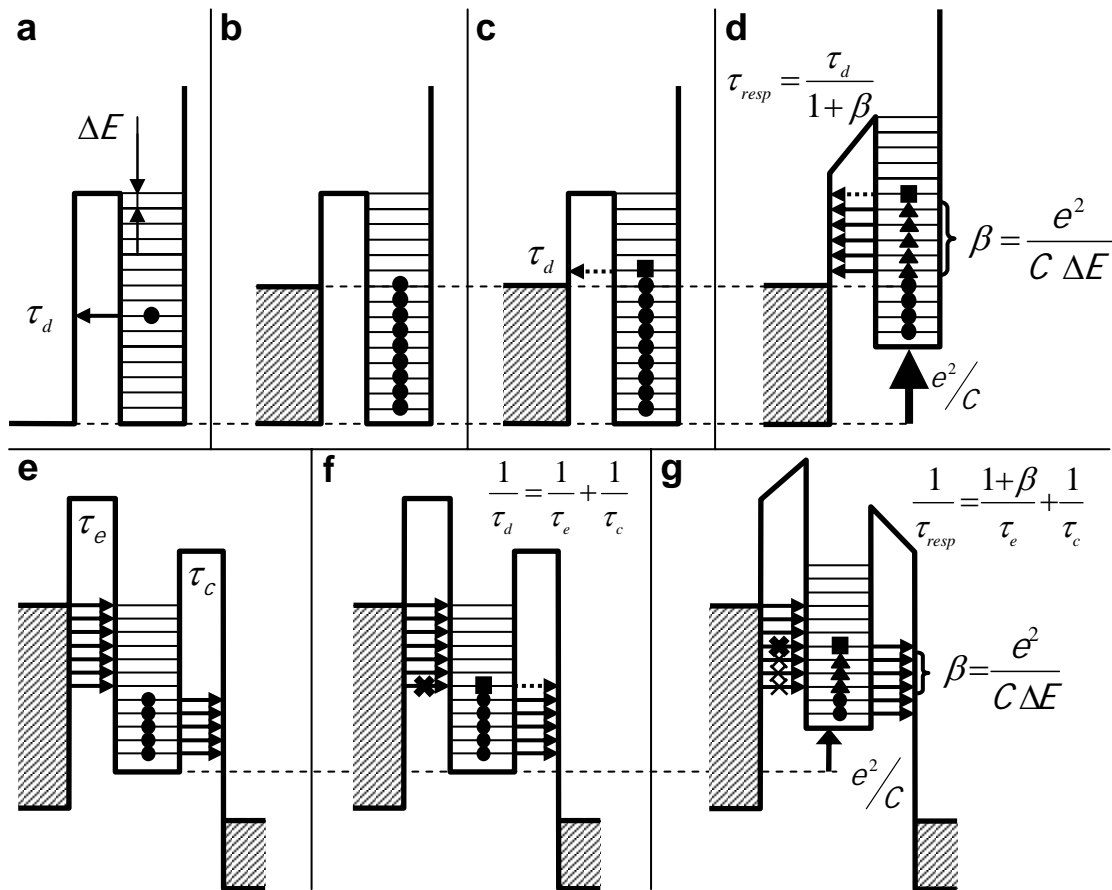


Figure 1.4: Mechanism for Coulomb reduction of the charge relaxation time ( $\tau_{resp}$ ).



Now let us turn to the high frequency behavior of RTD. It has been predicted theoretically [1, 47] that the resonant state lifetime ( $\tau_d$ ) does not impose fundamental limitation on the high frequency operation of RTD and it should be possible to extend the operational frequencies of RTD beyond the resonant state lifetime limit. The fact can be explained in the following way, the general expression for AC current in RTD which is the direct consequence of Shockley-Ramo theorem [48, 49] is,

$$\delta J_{RTD} = \frac{d}{d+l} \delta J_{ew} + \frac{l}{d+l} \delta J_{wc} + C_{ec} \frac{\partial}{\partial t} (\delta V_{RTD}), \quad (1.2)$$

Here  $J_{RTD}$  and  $V_{RTD}$  are the external RTD current and bias respectively.  $J_{ew}$ ,  $J_{wc}$  and  $C_{ec}$  are the emitter-well current, well-collector current and emitter-collector capacitances respectively (Fig. 1.5). The first two terms in the right hand side of equation (1.2) are real and contributes to RTD conductance. Whereas, the last term in the right hand side of equation (1.2) is imaginary and contributes to RTD capacitance. Among the two real current components of RTD (i.e.  $J_{ew}$  and  $J_{wc}$ ),  $J_{ew}$  is the resonant tunneling current and  $J_{wc}$  is the simple tunneling current. Since we are more interested in RTD conductance (or real part of RTD admittance), so we concentrate on the first two terms and exclude the displacement term (i.e. the last term of relation 1.2). The first term in the right hand side of equation (1.2), is resonant tunneling in nature. So in case of PDC region it is positive but in the NDC region it becomes negative. Now let us see the effect of time dependent variation of bias on these two terms. At the low frequency side (when  $\omega\tau_{resp} \ll 1$ ) the QW charges can keep pace with the applied AC bias variation since it's (AC bias) variation with time is slower than the RTD intrinsic response time. So the emitter-well current ( $J_{ew}$ ) and the well-collector current ( $J_{wc}$ ) remain in equilibrium through the QW electron concentrations ( $N_{2D}$ ) and  $J_{RTD} = J_{ew} = J_{wc}$ . Therefore, the measured AC conductance is simply the static conductance ( $\delta J_{RTD}/\delta V_{RTD} = \delta J_{ew}/\delta V_{RTD} = \delta J_{wc}/\delta V_{RTD}$ ). But the situation is different at the high frequency side i.e.  $\omega\tau_{resp} \gg 1$ . When the external AC perturbation is so fast that QW charges cannot follow it, well to collector current is not determined by the QW electron concentration ( $N_{2D}$ ). The well collector current density is defined by

$$J_{wc} = qN_{2D}\nu_c \quad (1.3)$$

Here  $q$  is the electronic charge and  $\nu_c$  is the electron escape rate across the well-collector barrier. If one applies a small variation to  $J_{wc}$  then relation 1.3 becomes,

$$\delta J_{wc} = q(N_{2D}\delta\nu_c + \nu_c\delta N_{2D}) \quad (1.4)$$

At very high frequencies (i.e.  $\omega\tau_{resp} \gg 1$ ),  $N_{2D}$  doesn't change much (because of the finite lifetime of quantum well electron) so  $\delta N_{2D} \rightarrow 0$ . Thus  $\delta J_{wc}$  becomes positive since it is determined by the first term of right hand side in relation (1.4). But the emitter-well current density ( $J_{ew}$ ) doesn't vanish but determined by the emitter-well voltage swing (i.e.  $J_{ew} \propto V_{RTD}d/(d+l)$  [1]). Thus  $J_{ew}$  which is resonant tunneling by origin, exists at high frequencies (i.e.  $\omega\tau_{resp} \gg 1$ ). Now let us turn to relation (1.2) to see the effect of emitter-well length ( $d$ ) and well-collector length ( $l$ ) on the RTD AC conductance at high frequencies when the RTD is operating in the NDC region of I-V characteristic. For the RTDs with long spacers ( $l \gg d$ , a typical example of such RTD can be found in the work of Mattia et. al. [36]) the first term in relation (1.2) is less dominant compared to the second term because of the leverage factors attached to them ( $d/(d+l)$  and  $l/(d+l)$ ), hence making the RTD conductance positive. By decreasing  $l$  the contribution from the first term (in relation 1.2) increases whereas the contribution from the second term (in relation 1.2) decreases. So for RTDs with  $l \approx d$  the first term would be more dominant than the second term in relation (1.2) and NDC should exist even at high frequencies. The fact that RTDs with  $l \approx d$  should demonstrate NDC at high frequencies has been predicted theoretically [1, 44]. The RTDs employed for high frequency applications contains long spacers in the collector side [20, 22, 36, 50] in order to reduce the depletion capacitance. Hence such RTDs when biased in the NDC region the AC conductance rolls up from the negative to the positive values with increasing frequency (relation 1.2). Experimentally such roll up in conductance was observed by Mattia et. al. [36]. So if the condition  $l \approx d$  is satisfied the first term in relation 1.2 would be significant which eventually makes RTD conductance at high frequencies negative in the NDC region of the I-V curve. Therefore resonant state lifetime should not limit the high frequency behavior of RTD and specially designed RTDs (diodes with heavily doped collector so that  $l \approx d$ ) should demonstrate NDC at frequencies far beyond the frequency corresponding to the inverse of quasi-bound-state lifetime.

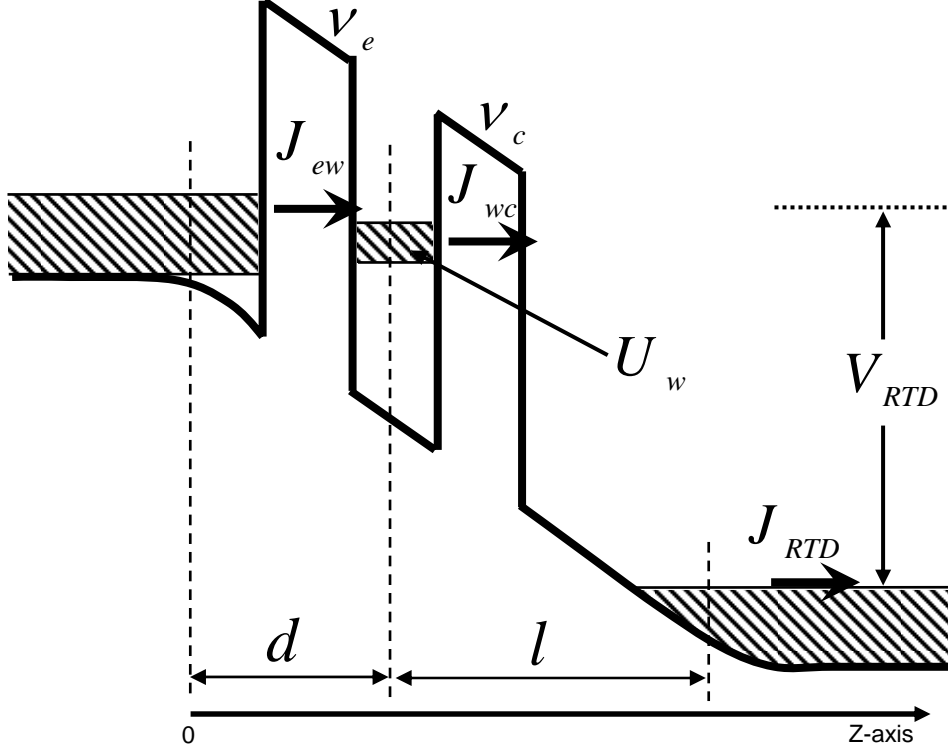


Figure 1.5: The conduction band diagram and the current components inside RTD.  $J_{ew}$  and  $J_{wc}$  are the emitter-well and well-collector current densities respectively. Whereas  $\nu_e$  and  $\nu_c$  are the emitter barrier and collector barrier tunneling rates respectively. In the steady state condition  $J_{RTD} = J_{ew} = J_{wc}$ . The emitter-well distance ( $d$ ) includes the emitter barrier length, half of the QW and the Thomas-Fermi screening length. Similarly, well-collector length ( $l$ ) comprises of half of the QW width, collector barrier length and the depletion length in the collector side.

So the main research objectives in this work are as follows. Firstly, experimental verification of the idea that the resonant tunneling current can exist in RTD beyond the resonant state lifetime limit. Secondly, to demonstrate experimentally the effect of Coulomb interaction effect on RTD response time. Thirdly, the experimental verification of the proposed simple small signal model [1] using the admittance measurements.

## 1.4 Overview of the work

The work done for this dissertation is documented here in the following manner.

In section 2 the development of the self-consistent static simulator under the sequential tunneling approximation is described. The static simulation is an important part of this work because it helps to predict the RTD behaviors before its fabrication at the same time it gives informations about the RTD layer parameters after its fabrication. Later on one can use the same RTD parameters for the AC analysis of the diodes. In order to see the reliability of the simulator we have simulated several RTD static curves from the literatures as well as our studied RTDs. The diodes we studied in this work are designed using the developed static simulator.

Section 3 contains the description of AC behaviors of RTD. In the beginning of this section a small introduction to the existing AC equivalent circuit [1, 44] is mentioned since for the study of AC behaviors of our diodes we are going to use this small signal model.

In the case of RTD with heavily doped collector and if the 2D subband in the QW is very low, one cannot ignore the collector to well backflow of electrons (it is being ignored previously [1, 44, 47]). The example of such diodes can be found in [46, 51]. For such diodes one needs to consider the backflow of electrons from collector to QW in order to describe the RTD admittances accurately. The extension of the already developed small signal model [1, 44] by including the backflow of electrons from collector to the emitter are described in this section. Further the consequences due to such modification are also studied.

It has been shown experimentally that RTD capacitance at low frequency limit (i.e.  $\omega\tau_{resp} \ll 1$ ) in the PDC region can be lesser [36] or higher [43] than the simple emitter-collector depletion capacitance. We have derived an analytical expression based on the developed theoretical model [1, 47] for the low frequency capacitance of RTD in terms of the device parameters which can explain the special experimental observations [36, 43] obtained before. We have also compared the measurement and simulation of bias dependent low frequency RTD capacitance and its (RTD capacitance at low frequency) deviation from emitter-collector capacitance.

The detailed description of the AC measurements and simulations of our studied diodes are presented in section 4. Firstly the small signal measurement and the extraction procedure of the "true" (intrinsic) RTD admittances are explained. The simulation results of the parasitics using CST microwave studio are presented. The comparison of the measurement

and simulation (simulation is done using the existing small signal equivalent circuit [44, 1]) of the RTD admittances are done. In this section, we have further described the role of Coulomb interaction effect parameter ( $\beta$ ) on the intrinsic RTD response time ( $\tau_{resp}$ ) by experiment and simulation. The comparison in between the RTD response time ( $\tau_{resp}$ ) and quasi-bound state lifetime ( $\tau_d$ ) at several bias points are also presented.

Section 5 describes the summary of the results we have achieved during the course of this thesis work and the possible work that can be done in future.

## 1.5 Research results to be defended

The research results of this dissertation work are as follows,

- Experimental demonstration of resonant tunneling beyond the resonant state lifetime limit
- Demonstration of Coulomb interaction effect on RTD response time ( $\tau_{resp}$ ) and resonant state lifetime ( $\tau_d$ ) by experiment and simulation
- Verification of analytically derived RTD small signal equivalent circuit [1, 44] by the following procedures,
  - Simulation and measurements of RTD admittances for the whole frequency range
  - Simulation and measurements of deviation of low frequency ( $\omega\tau_{resp} \ll 1$ ) RTD capacitances from geometrical emitter-collector capacitance
- Demonstration of a small signal AC model for RTD considering the backflow of electrons from collector to QW.

# Chapter 2

## Self-consistent simulation of RTD

### 2.1 Existent RTD models

In 1973 Tsu and Esaki [8] proposed the first theoretical model for double barrier resonant tunneling diode (RTD). In the next year the first RTD was demonstrated [52] although the NDC was hardly prominent. In the following decades, some special properties of III-V compound semiconductors as well as excellent progress in crystal growth and fabrication techniques had allowed to achieve RTDs with peak to valley current ratio (PVCR) of the value of 62 (30) at liquid nitrogen temperature (room temperature) [16]. Comparing to the first reported experimental double-barrier RTD [52] such high value of PVCR is undoubtedly an excellent achievement by the scientific community.

Existing physical models for current transport in RTD are divided into two categories called as coherent model and sequential tunneling model. Coherent model is based on the theoretical work done by Tsu and Esaki [8]. They considered the tunneling electron doesn't experience any phase-coherence breaking events throughout the structure. Later many people [53] accepted this model for the simulation of current-voltage characteristic of RTD. In the year of 1985, Luryi [7] introduced the concept of sequential tunneling for the electron transport in RTD. In contrast to global coherent model electron transport across the device is considered as two step process in sequential tunneling approach. First, the electrons tunnel across the emitter-well barrier resonantly and loses its phase memory completely. Then the second step is simple tunneling of the electrons from quantum well to the collector. In case of thin barrier RTDs the coherent model is appropriate since an electron can tunnel through the whole structure without losing its memory.

Whereas for the thick barrier RTDs the electron lifetime in the QW is long so that it spends sufficient time in the QW and forgets its phase memory. In sequential tunneling the electron distribution is thermalized completely in every region (be it emitter, well or collector).

In addition to the transport mechanism mentioned already, there can be several other channels for electron transport in double barrier RTD depending on the material system considered. If the barriers are low (e.g. GaAs/AlGaAs material system), a significant amount of current can be contributed by the thermionic emission as well as field-assisted tunneling due to the triangular shaping of the barriers. Other current components could be due to the non-resonant tunneling current,  $\Gamma - X$  coupling of energy bands [54] or LO phonon assisted current [55].

To understand the electronic transport and for the sake of device design one needs to have an accurate model for any semiconductor device. Mainly two types of models are used to describe the current transport through RTD or any other semiconducting devices. They are called as (i) physical models [53] and (ii) circuit design models [56]. In the category of physical models different physical effects occurring inside the device are taken into considerations. Physical models carry more importance from scientific point of view. By circuit design model I mean RTD model which can easily be included into a circuit simulator for example in SPICE [56]. A direct relation in between current and voltage is preferable for such type of model instead of dealing with the complicated physical parameters. The physical models for RTD device are classified into two categories called as coherent tunneling and sequential tunneling model (both the models are described before). For circuit design purposes RTDs are described by mathematical models and generally they are represented with robust analytical expressions [56, 57, 58]. Some of these models do not rely on the inherent underlying device physics completely [56, 58] and in many cases they are basically the curve fitting procedures [57]. The models described in references [56, 58] started from the Tsu-Esaki relation [8] but in order to make the I-V model simple and compatible with SPICE they introduced several constants and those constants are derived by fitting the model with the measured I-V characteristics.

## 2.2 Development of the static simulator

The process of wafer growth and semiconductor fabrication technology are very expensive. So accurate simulations and computer aided design can save huge amount of time and money. Unfortunately suitable software packages in the nanometric dimensions as required for RTDs were not available in our hand. Therefore, we constructed our own software tool, applying a very fast way to calculate the current-voltage characteristics. Our developed self-consistent static simulator for resonant tunneling diodes works in the sequential tunneling approximation [7]. We have opted for sequential tunneling model because the RTDs we are going to design for our study of AC behaviors are thick barrier RTDs (the reason of choosing thick barriers for the RTD is described elaborately in chapter 4). In case of thick barrier RTD the electron spends enough time to forget its phase memory and the process of tunneling across the emitter and collector barrier is a two step process. So, sequential tunneling model is appropriate for such RTDs. Now we first describe, the physical effects we considered in our self-consistent static simulation.

### 2.2.1 Current density expressions

We have assumed the current distribution to be homogeneous in the plane of the barriers and the electrons obey Fermi-Dirac distribution. The emitter-well current density across the emitter barrier in the forward direction considering an empty QW (the derivation is shown in the Appendix) is,

$$J_{ewF} = e \int_{U_w}^{\infty} \rho_{2D} f_e(E) \nu_e dE, \quad (2.1)$$

Similarly the reverse current density across the emitter barrier considering empty emitter will be,

$$J_{ewR} = -e \int_{U_w}^{\infty} \rho_{2D} f_w(E) \nu_e dE, \quad (2.2)$$

Here,  $e$  is the electronic charge,  $\rho_{2D}$  is the 2 dimensional density of states,  $k$  is Boltzman constant and  $\nu_e$  is the escape rate across the emitter barrier.  $f_e(E)$  and  $f_w(E)$  are the Fermi functions to define the distribution of electrons in the emitter and QW,



$$f_e(E) = \frac{1}{1 + \exp\left(\frac{E - E_{fe}}{kT}\right)}, \quad (2.3)$$

$$f_w(E) = \frac{1}{1 + \exp\left(\frac{E - E_{fw}}{kT}\right)}, \quad (2.4)$$

$E_{fe}$  and  $E_{fw}$  are the Fermi level positions in the emitter and quantum well, respectively. The net current density across the emitter barrier would be the sum of the emitter-well forward (relation 2.1) and backward (relation 2.2) current densities. After performing the definite integrations in the relations (2.1) and (2.2) considering the Fermi distribution functions (2.3 and 2.4), the net current density across the emitter barrier ( $J_{ew}$ ) is,

$$J_{ew} = e\rho_{2D}kT\left[\ln\left(1 + \exp\frac{E_{fe} - U_w}{kT}\right) - \ln\left(1 + \exp\frac{E_{fw} - U_w}{kT}\right)\right]\nu_e, \quad (2.5)$$

Similarly the well-collector current density is derived as,

$$J_{wc} = e\rho_{2D}kT\left[\log\left(1 + \exp\frac{E_{fw} - U_w}{kT}\right) - \log\left(1 + \exp\frac{E_{fc} - U_w}{kT}\right)\right]\nu_c, \quad (2.6)$$

Here,  $E_{fc}$  is the Fermi level position at the collector,  $\nu_c$  is the electron escape rate across the collector barrier. The first term in equation (2.6) gives the forward current density from well to collector considering the collector is empty. Similarly the second term in the same equation (2.6) calculates the backward well-collector current density by assuming an empty well. So the resultant current density across the collector barrier or the net well-collector current density ( $J_{wc}$ ) is the sum of the two opposite current densities across the collector barrier. Hence the analytical expressions (relation 2.5 and 2.6) for the emitter-well ( $J_{ew}$ ) and well-collector ( $J_{wc}$ ) current densities are derived (current components are shown in Fig. 2.1).

## 2.2.2 Quantum well electron density

In the DC condition the emitter-well current density ( $J_{ew}$ ) would be the same to the well-collector ( $J_{wc}$ ) current density from the steady state current condition or kirchoff's first law. The condition that  $J_{RTD} = J_{ew} = J_{wc}$  gives information about the Fermi level position of the QW ( $E_{fw}$ ). The expression for 2 dimensional concentration ( $N_{2D}$ ) of electrons in side the QW is,

$$N_{2D} = \int_{U_w}^{\infty} \rho_{2D} f(E_w) dE, \quad (2.7)$$

Using the Fermi-distribution of electrons in the QW (relation 2.4), the expression for  $N_{2D}$  is derived as,

$$N_{2D} = \rho_{2D} kT \left[ \log \left( 1 + \exp \frac{E_{fw} - U_w}{kT} \right) \right], \quad (2.8)$$

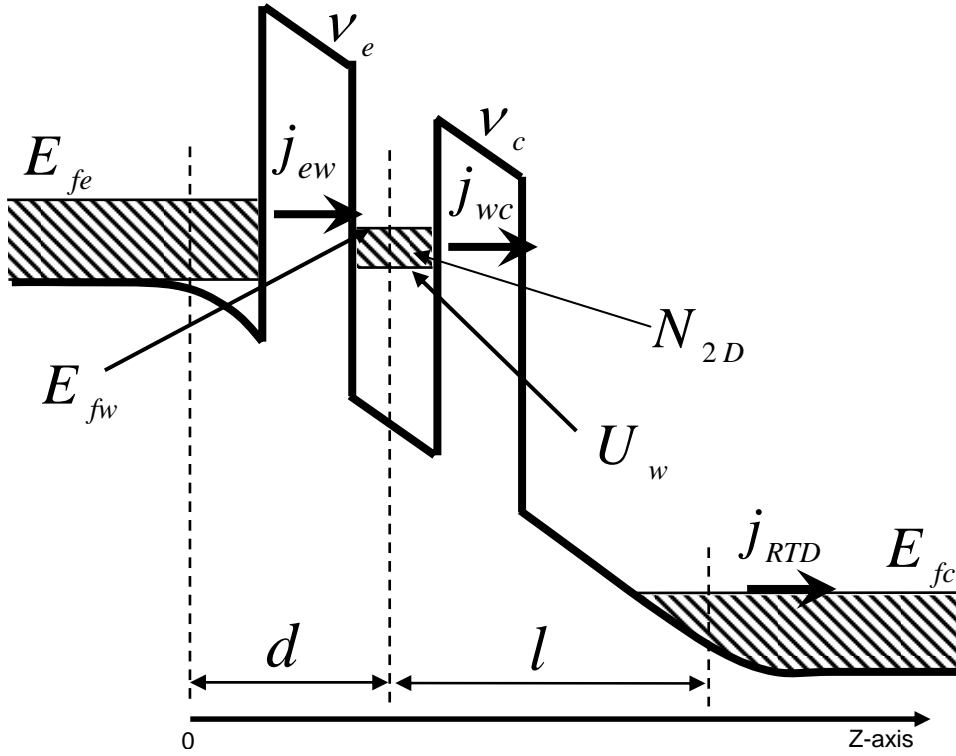


Figure 2.1: The conduction band diagram and the different current components inside RTD.  $E_{fe}$ ,  $E_{fw}$  and  $E_{fc}$  are the Fermi level positions at the emitter, QW and collector, respectively.  $U_w$  is the bottom of the resonant state subband in the QW.

### 2.2.3 Tunnel transparency of the barriers

In order to calculate the emitter-well ( $J_{ew}$ ) and well-collector ( $J_{wc}$ ) current densities, calculation of the transmission rates across the barriers ( $\nu_e$  for emitter barrier and  $\nu_c$  for collector barrier) are required. To solve the tunnel transparencies ( $\nu_e$  or  $\nu_c$ ) analytically, we make some simplifying assumptions to the potential profile in the form of staircase approximation (situation is shown elaborately in Fig. 2.2).

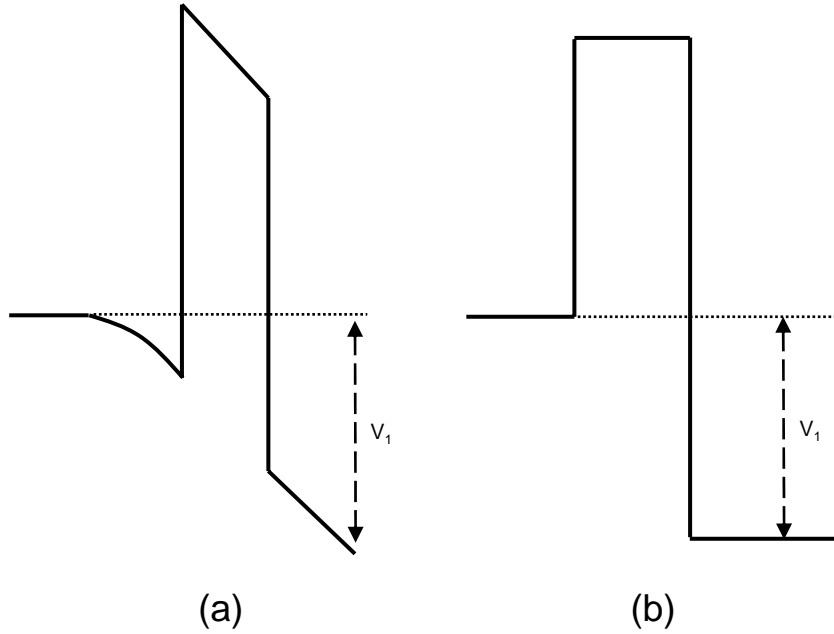


Figure 2.2: Conduction band profile of a typical barrier under bias. (a) actual profile. (b) staircase approximation to the actual profile in order to simplify the analytical calculation of the barrier tunnel transparencies.

The calculation of the tunneling co-efficient ( $D$ ) for the barrier is shown in the appendix. If  $\nu_0$  is the attempt frequency of the electron at the resonant state in the QW then the escape rate of the same electron across the barrier would be  $\nu = D\nu_0$ . By attempt frequency ( $\nu_0$ ), we mean the number of times in one second an electron in the resonant state strikes the wall of the barrier. The expression for attempt frequency is,

$$\nu_0 = \frac{1}{2A_w} \sqrt{\frac{2E_0}{m_w}}, \quad (2.9)$$

$A_w$  is the width of the QW and  $m_w$  is the effective electron mass in the QW.

So the escape rates across the emitter-well ( $\nu_e$ ) and the well-collector ( $\nu_c$ ) barriers will be  $\nu_e = \nu_0 D_e$  and  $\nu_c = \nu_0 D_c$ , respectively. Where,  $D_e$  is the transmission co-efficient for the emitter-well barrier and  $D_c$  is the transmission co-efficient for the well-collector barrier.

### 2.2.4 Non-parabolicity effect

In case of RTDs the simple single band parabolic model for the energy vs. momentum dispersion relationship isn't valid and in reality the energy vs. momentum relationship is highly non-parabolic [14]. In case of single band model, imaginary wave vector goes to infinity as energy goes to negative infinity. Actually the imaginary wave vector connects the conduction and valence bands instead of diverging to negative infinity, hence makes the energy vs. momentum dispersion relationship highly non-parabolic ([14] and Fig. 2.3). We have included the non-parabolicity effect by modifying the electron effective mass relationship in the following manner,

$$m^* = m_c \frac{E'_g}{E_g}, \quad (2.10)$$

where  $m^*$  and  $m_c$  are the electron effective mass considering non-parabolicity and electron effective mass at the conduction band edge. Similarly,  $E_g$  and  $E'_g$  are the bandgap and effective bandgap, respectively.  $E_g$  and  $E'_g$  are defined as  $E_g = E_c - E_v$  and  $E'_g = E - E_v$  (Fig. (2.3)). In order to justify our approximation (relation 2.10), let us consider the energy vs. wave vector relationship,

$$k = \sqrt{\frac{2m^*(E - E_c)}{\hbar^2}}, \quad (2.11)$$

Combining equations (2.10), (2.11) with the expressions for  $E_g$  and  $E'_g$  we get for the wave vector,

$$k = \sqrt{\frac{2m_c (E - E_c)(E - E_v)}{\hbar^2 (E_c - E_v)}}, \quad (2.12)$$

Now in relation (2.12) when  $E = E_c$  or  $E = E_v$ , the wave vector becomes  $k = 0$ . So at the conduction and valence band edges wave vector ( $k$ ) goes to zero value as it was shown already [14]. Hence for our simulation, we will not consider the electron effective mass at

the conduction band edge but the modified effective mass due to non-parabolicity ( $m^*$  as in relation 2.10).

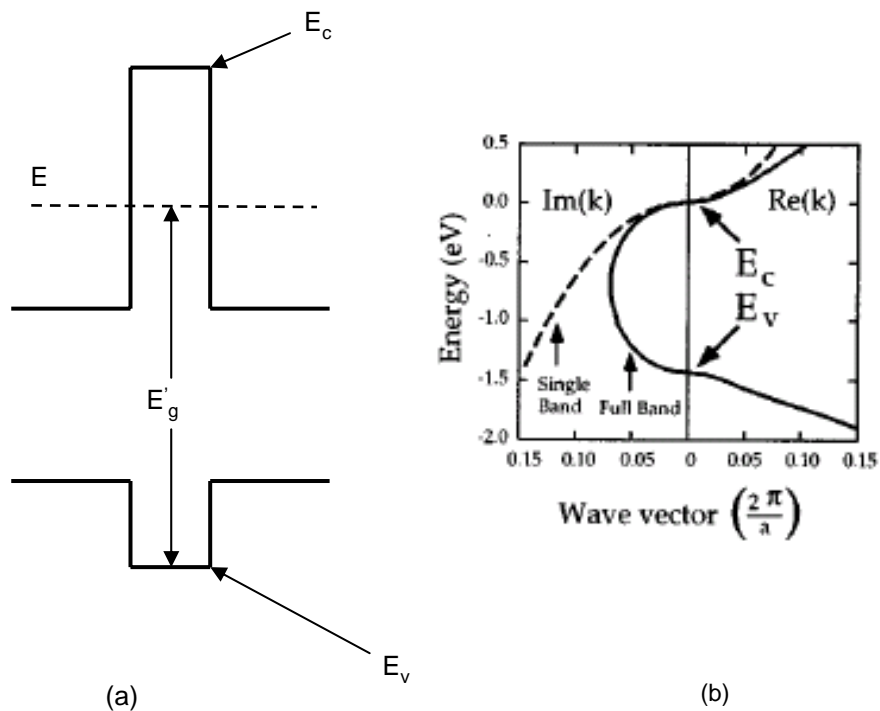


Figure 2.3: Effect of non-parabolicity on the electron effective mass is shown here. In panel (a),  $E_c$  and  $E_v$  are the conduction band edge and valence band edge of the barrier, respectively.  $E$  is the energy of the tunneling electron through the barrier. The dispersion relation in panel (b) is taken from the work of Bowen et. al. [14]. In their work [14], it is clearly shown that the energy band dispersions are non-parabolic in the barrier region as well as in the conduction or valence band region.

### 2.2.5 Screening length

The emitter-well length ( $d$ ) consists of half of QW width, emitter barrier thickness and the Thomas Fermi screening length at the emitter side (Fig. 2.1). The QW width and the emitter barrier thickness are known from the RTD geometrical parameters. So we need to calculate the Thomas Fermi screening length in order to define the emitter-well length. Under the applied bias electrons accumulate in the emitter region close to the barrier. These electrons screen the applied field so that far away from the emitter to barrier interface field ( $F$ ) goes to zero. In order to evaluate the screening length, we solve the Poisson's relation in one dimension (here it is  $z$ -dimension, see Fig. 2.4).

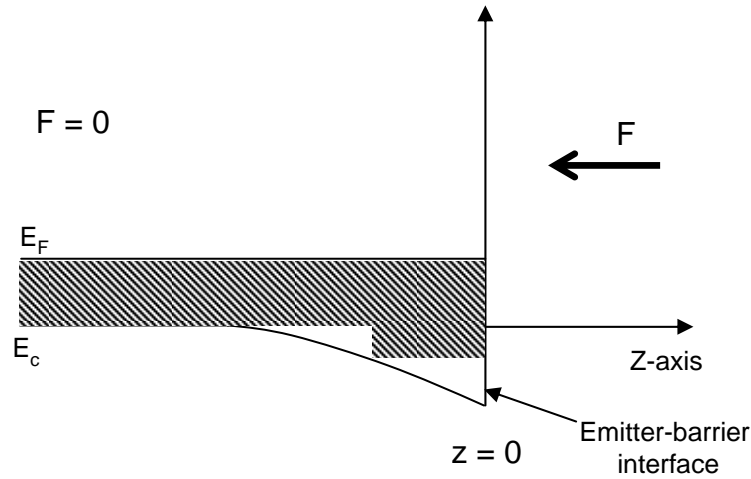


Figure 2.4: Conduction band profile of the emitter region close to the emitter-barrier interface. Field  $F$  diminishes to zero far away from the emitter-barrier interface along the negative  $z$ -direction.

$$\frac{\partial^2 V(z)}{\partial z^2} = -\frac{\rho(z)}{\epsilon}, \quad (2.13)$$

where  $\rho$  is the charge density in  $C/cm^3$ ,  $\epsilon$  is the electrical permittivity of the material ( $\epsilon = \epsilon_r \epsilon_0$ ,  $\epsilon_r$  is the relative permittivity of the material and  $\epsilon_0$  is the permittivity of free space),  $V(z)$  denotes the potential function respectively. The charge density is defined as,

$$\rho(z) = e(-n + N_d), \quad (2.14)$$

$n$  and  $N_d$  are the electronic charges and the doping concentrations in the emitter region respectively. Solving equations (2.13) and (2.14), relation for the potential function ( $V(z)$ ) obtained is,

$$V(z) = C_1 \exp(-z/\lambda_{TF}), \quad (2.15)$$

where  $C_1$  is an arbitrary constant arising due to integration and

$$\lambda_{TF} = \sqrt{\left(\frac{2\pi^2\epsilon}{e^2 E_F^{0.5} 3\sqrt{2}} \left(\frac{\hbar}{m^*}\right)^{1.5}\right)}, \quad (2.16)$$

$\lambda_{TF}$  is termed as Thomas-Fermi screening length. In the emitter side at distance  $\lambda_{TF}$ , the value of the potential diminishes to 0.36 times its value at the interface (relation 2.15). Electric field ( $F$ ) also drops similarly at distance  $\lambda_{TF}$  (Fig. 2.5).

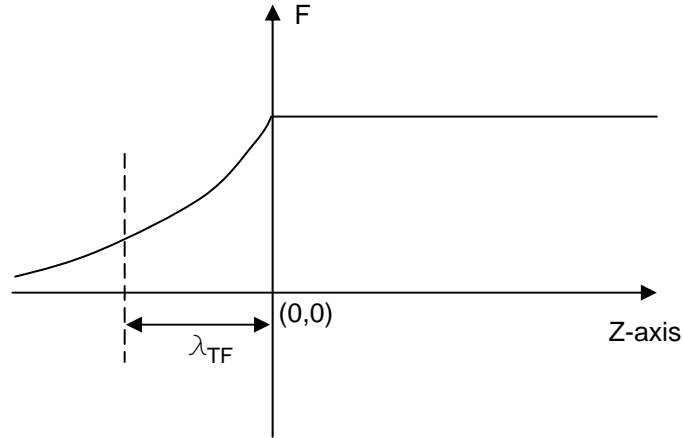


Figure 2.5: The schematic shows how the applied field diminishes in the barrier region. After traversing length  $\lambda_{TF}$  in the negative  $z$ -direction, field drops by 0.36 times to its value at the emitter-barrier interface.

### 2.2.6 Resonant state level broadening

The resonant state level in the QW is broadened in energy because of the finite lifetime of the electron in the QW and due to the roughness of the well to barrier interfaces. Level broadening caused by the finite electron lifetime inside the QW can be calculated using uncertainty principle but the broadening corresponding to the roughness can not be analytically evaluated. The broadening of the QW level directly affects the resonant tunneling transitions across the emitter barrier. Because of the broadening of the level some states in the QW take part in resonant tunneling across the emitter barrier but not the all and the number of states which will participate in RT depends on the applied bias i.e. on the QW resonant level position. The situation is shown elaborately in figure (2.6).

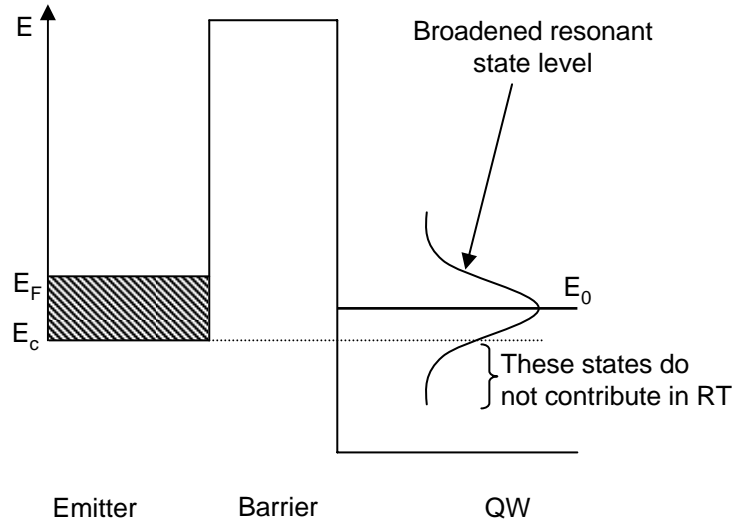


Figure 2.6: The schematic shows the broadening of the resonant state energy level.  $E_0$  is the position of the middle of the broadened resonant state.

If  $\delta(E)$  is the broadening function to represent the level broadening then the broadening function should be normalized for the whole energy range as,

$$\int_{-\infty}^{\infty} \delta(E) dE = 1, \quad (2.17)$$

In order to include the effect of broadening on resonant tunneling across the emitter-well barrier, we use the following technique,



$$D_0(E_0) = \int_{E_c}^{\infty} D(E)\delta(E - E_0)dE, \quad (2.18)$$

The limit of the integration is taken from  $E_c$  since the states below  $E_c$  do not participate in RT. So we exclude the states in the broadened QW resonant state level which do not participate in RT (Fig. 2.6). The form of the broadening function used is,

$$\delta(E - E_0) = \frac{1}{\pi\Delta E} \frac{1}{1 + \left(\frac{E-E_0}{\Delta E}\right)^2}, \quad (2.19)$$

The integral in the right hand side of equation (2.18) is not possible to evaluate analytically, so we use numerical method to calculate  $D(E)$ .

## 2.2.7 Depletion length

The well-collector length ( $l$ , Fig. 2.1) consists of half width of the QW, the collector barrier thickness and the depletion length in the collector side. Our next task is to calculate the depletion length at the collector side ( $L_d$ , Fig. 2.7). So we solve one dimensional Poisson's relation at the collector region close to the well-collector barrier. In figure (2.7),  $V_1$  is the bias across the emitter and the middle of the QW,  $V_{RTD}$  is the total voltage drop inside RTD,  $s$  is the length of the spacer in the collector side and  $L_d$  is the depletion length at the collector side. The well collector length ( $l$ ) is defined as  $l = A_w/2 + A_b + s + L_d$ . The doping density at the collector side is denoted by  $N_D$ .

After solving one dimensional Poisson's relation in the region from  $z = d$  to  $z = d + l$ , we derive the following expression for the depletion length,

$$L_d = \frac{N_{2D}}{N_D} + \frac{\epsilon V_1}{edN_D}, \quad (2.20)$$

and the total voltage drop across RTD is,

$$V_{RTD} = \frac{1}{2} \frac{eN_D}{\epsilon} L_d^2 + \left( (1 + s/d)V_1 + \frac{eN_{2D}s}{\epsilon} \right), \quad (2.21)$$

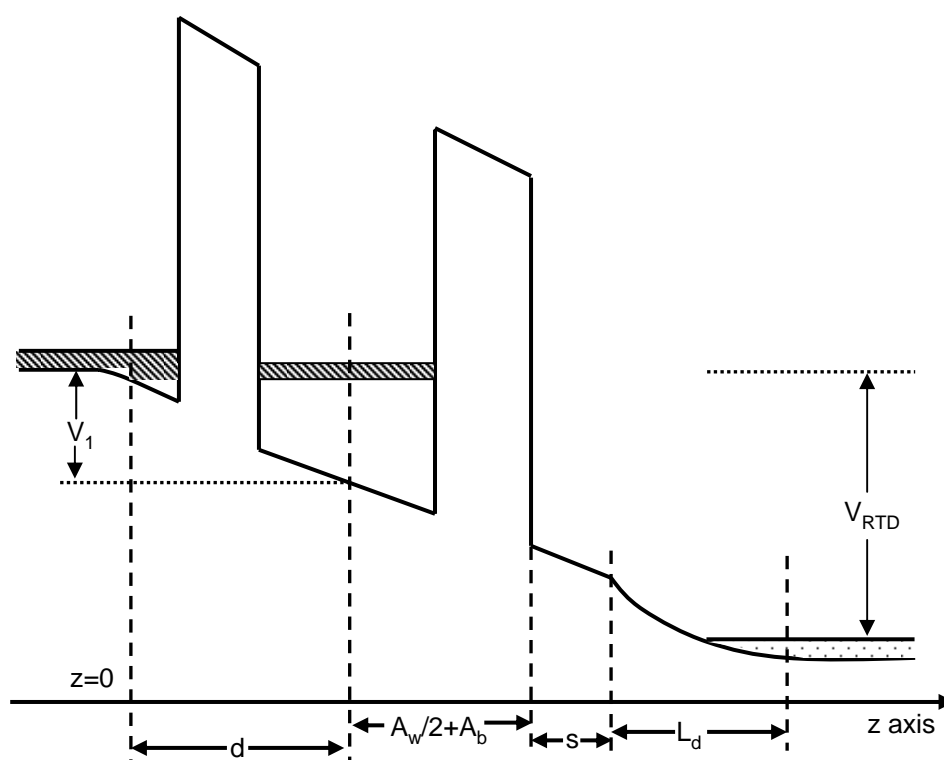


Figure 2.7: The schematic shows the conduction band profile in the  $z$ -direction under the applied bias.

### 2.2.8 Effect of strain

Heterojunctions are formed by using semiconductors of different bandgaps. In case of group III-V compound semiconductors different material systems, e.g.  $GaAs/AlGaAs$ ,  $GaAs/AlAs$ ,  $InGaAs/AlAs$  are used to form the heterostructures. If the corresponding semiconductors forming the heterojunction, have different lattice constants then the grown layers suffer from lattice mismatch. Because of this lattice mismatch compressive or tensile strains can form in the grown layer. There is a certain thickness called as critical thickness, upto which a single heterojunction can be formed without allowing the formation of misfit dislocations [59]. So while growing heterojunctions people always intend to keep the grown layer well below the critical thickness. At the same time because of the presence of strain inside the grown layer the conduction band offset also changes. In our RTDs, we are going to use  $AlAs$  (lattice constant 0.566 nm) as barrier on  $In_{0.53}Ga_{0.47}As$  (lattice constant 0.586 nm) as emitter or collector giving rise to  $\approx 4\%$  of lattice mismatch. Now we calculate the change in conduction band offset when  $AlAs$  epitaxial layer is grown on  $In_{0.53}Ga_{0.47}As$  as substrate considering the effect of strain.

If z-axis is the direction of growth, then the diagonal components of the strain tensor in the perpendicular direction to z-axis are,

$$\epsilon_{xx} = \epsilon_{yy} = (a_{bulk} - a_{epilayer})/a_{epilayer}, \quad (2.22)$$

For  $AlAs$  epilayer grown on  $In_{0.53}Ga_{0.47}As$ , relation (2.22) takes the form,

$$\epsilon_{xx} = \epsilon_{yy} = (a_{In_{0.53}Ga_{0.47}As} - a_{AlAs})/a_{AlAs}, \quad (2.23)$$

Using the values  $a_{In_{0.53}Ga_{0.47}As} = 0.586$  nm and  $a_{AlAs} = 0.566$  nm [60], the value of  $\epsilon_{xx}$  comes out to be 0.0366. The third diagonal component of strain tensor is,

$$\epsilon_{zz} = -2 \frac{C_{12}}{C_{11}} \epsilon_{xx}, \quad (2.24)$$

the values of the elastic stiffness constants  $C_{12}$  and  $C_{11}$  for  $AlAs$  are 5.34 and 12.5 [60], respectively. So we derive  $\epsilon_{zz} = -0.031$ .

The change in conduction band offset is given by the following relation from reference [61],

$$\Delta E_c = (\epsilon_{xx} + \epsilon_{yy} + \epsilon_{zz})A_{AlAs}^c, \quad (2.25)$$

where  $A_{AlAs}^c$  is the deformation potential for AlAs and its value is -5.64 eV [62]. Using the values of  $\epsilon_{ii}$  and  $A_{AlAs}^c$ , we get  $\Delta E_c = -0.22$  eV. The nominal (in the absence of strain) conduction band offset in case of  $In_{0.53}Ga_{0.47}As/AlAs$  heterojunction is 1.26 eV. So conduction band offset in the presence of strain would be 1.04 eV ((1.26 – 0.22) eV).

### 2.2.9 Algorithm of the simulator

After deriving the relevant relations for the physical effects occurring inside the device, we move on to build the static model for RTD. Our self-consistent model works in the following way. The schematic of the algorithm for the model is shown in figure 2.8. We consider uniform voltage drop across the emitter well region i.e. from  $z = 0$  upto  $z = d$ . So the position of the bottom of the 2D subband ( $U_w$ ) inside the QW is first established. With this potential profile the emitter barrier transparency ( $\nu_e$ ) is calculated hence the emitter to well current density is evaluated (equation 2.5). Next it calculates the collector barrier transparency ( $\nu_c$ ) and solves Poisson's relation to evaluate well-collector length ( $l$ ). Further it calculates the two dimensional electron concentration in the QW (relation 2.8) as well as the other current density component (i.e.  $J_{wc}$ ). The first iteration is done by considering  $N_{2D} = 0$  (where  $N_{2D}$  is the electron density in the QW), as a first approximation. Because of the presence of  $N_{2D}$  the conduction band potential profile changes hence the tunnel transparencies across the barriers. So for every iteration, at the particular value of  $U_w$ , the collector barrier escape rate is calculated ( $\nu_c$ ). This self-consistent method of calculating the current components and the potential profile are done iteratively until the convergence in terms of  $N_{2D}$  is achieved.  $\delta N_{2D}$  is the difference of the values of  $N_{2D}$  for two consecutive iterations. The iterations are done until the condition  $\delta N_{2D} < eps$  is achieved where  $eps \approx 1 \times 10^{-9} N_{2D}$ . Once the convergence with the required accuracy is achieved, we record the different RTD parameters (e.g. tunneling current ( $J_{RTD}$ ), voltage drop across the device ( $V_{RTD}$ ),  $\nu_e$ ,  $\nu_c$  etc.) before we go for the next bias point. In this way we have developed a simple and fast but effective single-band model for the calculation of the current-voltage characteristics for RTDs.

Now let us describe qualitatively, the impact of different physical effects on the static

simulation. The simulator is developed by considering the space-charge effects due to the electronic charge accumulation in the quantum-well [63, 64], the non-parabolicity effects on the electron effective mass [14] and the effects of strain on the band-structure of the barriers and quantum-well [65]. The space charge in the QW makes the conduction band bottom inside the well to go up, which in turn changes the potential profile inside the device. So the space charge effect has significant impact on the electrical behavior of RTD and one must consider it. The effective mass of electron in the quantised state or inside the barrier are not same to its value at the conduction band edge because of the non-parabolicity effect. Effective mass has strong impact on tunneling rates and on the position of the resonant state in the QW. Different material systems are used to form heterostructure. Depending upon the difference in lattice constant the epilayers can have different degree of lattice mismatch. In case of InGaAs/AlAs material system the lattice mismatch is around 3.9 percent [60] and it (strain) changes the conduction band off set from 1.26 eV to 1.04 eV, hence affects the tunnel transparencies. So the purpose of considering different physical effects in the simulator is to develop a static model of RTD so that it can reproduce the static measurements as precisely as possible.

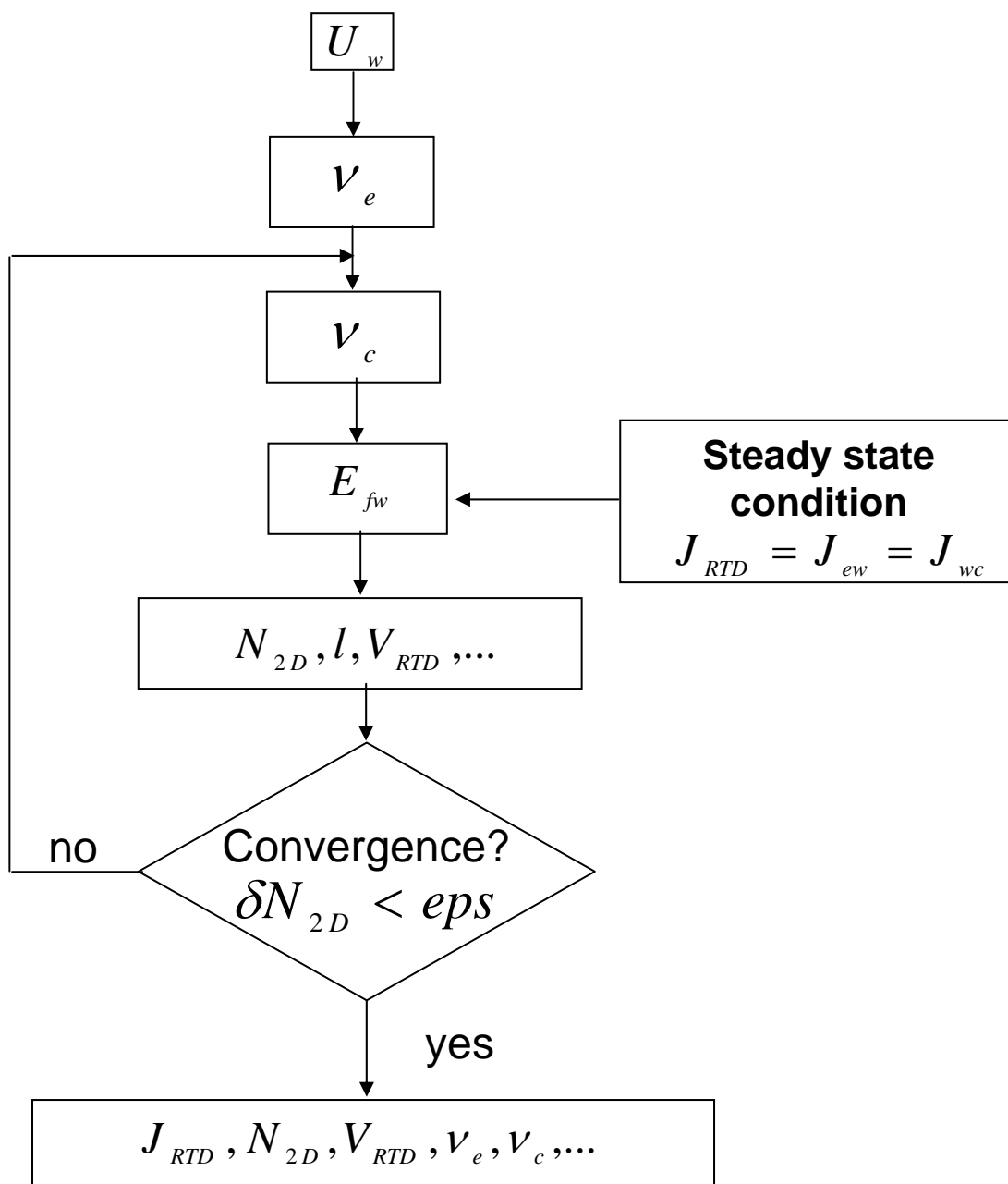


Figure 2.8: The schematic of the algorithm of the developed self-consistent RTD simulator.

## 2.3 Verification of the developed simulator

So the self-consistent static model for RTD is developed. We found our simulator based on the current continuity equation and Poisson's relation, is very effective for different types of RTDs. The developed simulator can reproduce the measured current-voltage characteristics from literatures with reasonably good accuracy using the same layer structures as mentioned there. The diodes we studied for verifications have thin [51] and thick [36] barriers, simple [36] and composite quantum well [51] or multiple resonances in its static characteristic [16]. Later we design the RTDs for our experiments using the developed simulator. We have obtained good agreement in between the simulated and the measured I-V characteristics of the diodes studied in this thesis. The layer structures used for simulation and as revealed by XRD measurements are also in reasonable agreement. The layer parameters needed for device simulations, such as mole fraction (in case of ternary or higher order compound semiconductors), doping density, thickness of the layers are not known exactly. They depend on the temperature and the conditions inside the chamber during the crystal growth. Two similar heterostructures grown in two different systems or even they grow in the same system but at different times can show discrepancies in electrical performances. For example, the uncertainty in the doping concentration or the barrier thickness are of the orders of 10 percent or one monolayer. So keeping these facts in mind the agreement we have achieved in between simulations and measurements, considered to be good enough.

### 2.3.1 From literatures

In order to verify the reliability of the developed solver we simulated I-V characteristics of various kinds of RTDs from literatures [16, 36, 51]. One of the structures we simulated is the relatively simple structure from Mattia et. al. [36]. The diodes they studied had simple quantum well, thick barriers and long spacer in the collector side. Figure 2.9 compares the measured I-V curve by Mattia et. al. with our calculation.

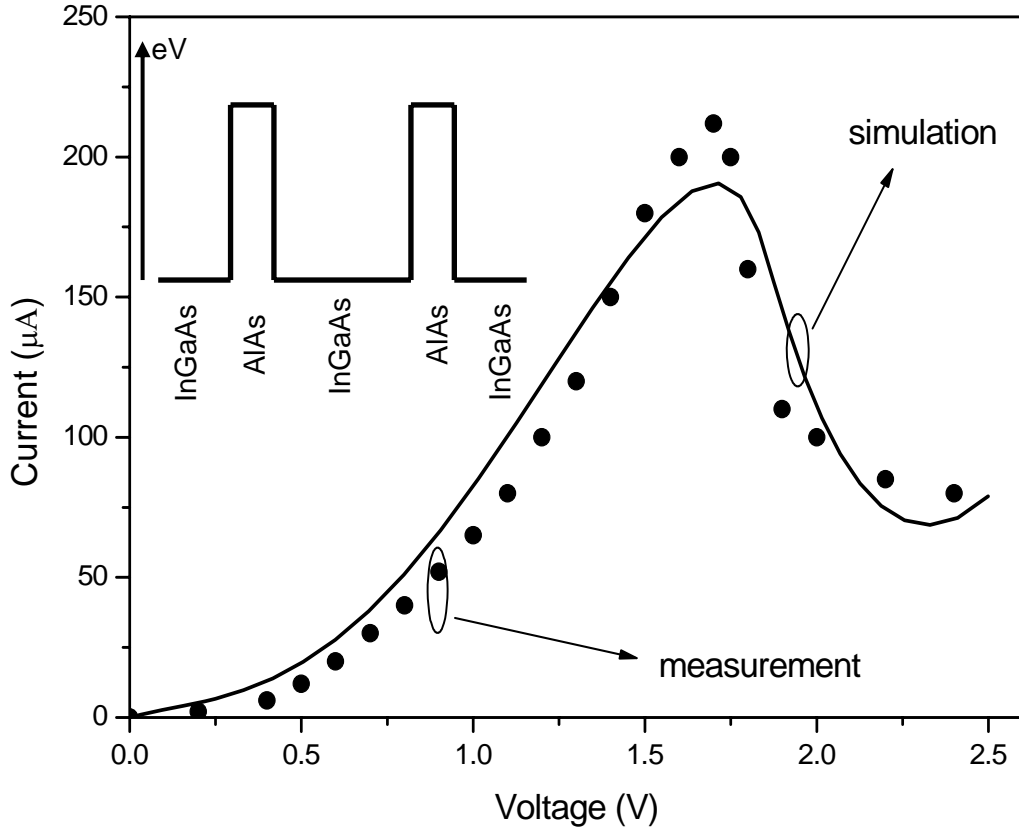


Figure 2.9: The experimental I-V characteristic from Mattia et. al. [36] and our self-consistent simulation. The nominal thickness of the barrier and QW are 4.1 nm and 5.5 nm respectively. But their simulation resulted in a peak current density 2.3 times higher than measurement although the peak voltage was matching well. So in order to match the I-V curves they increase the barrier thickness to 4.5 nm for their simulations. The barrier thickness used in our simulation is 4.0 nm with the QW width of 5.5 nm. Our simulation consider same doping densities in the emitter and collector regions as the reported nominal values. In their diode they have  $2 \times 10^{16} \text{ cm}^{-3}$  doping concentration in the spacers and  $2 \times 10^{18} \text{ cm}^{-3}$  dopants in the emitter and collector. They were using 10 nm spacer in the emitter side and 100 nm spacer in the collector side. Inset shows the conduction band diagram for the studied RTD.



The diode studied by Auer et. al. [51] consists of composite *InGaAs/InAs* materials for QW with short spacers and relatively thin symmetric barriers. Our simulation is compared with their measured static characteristics in figure 2.10.

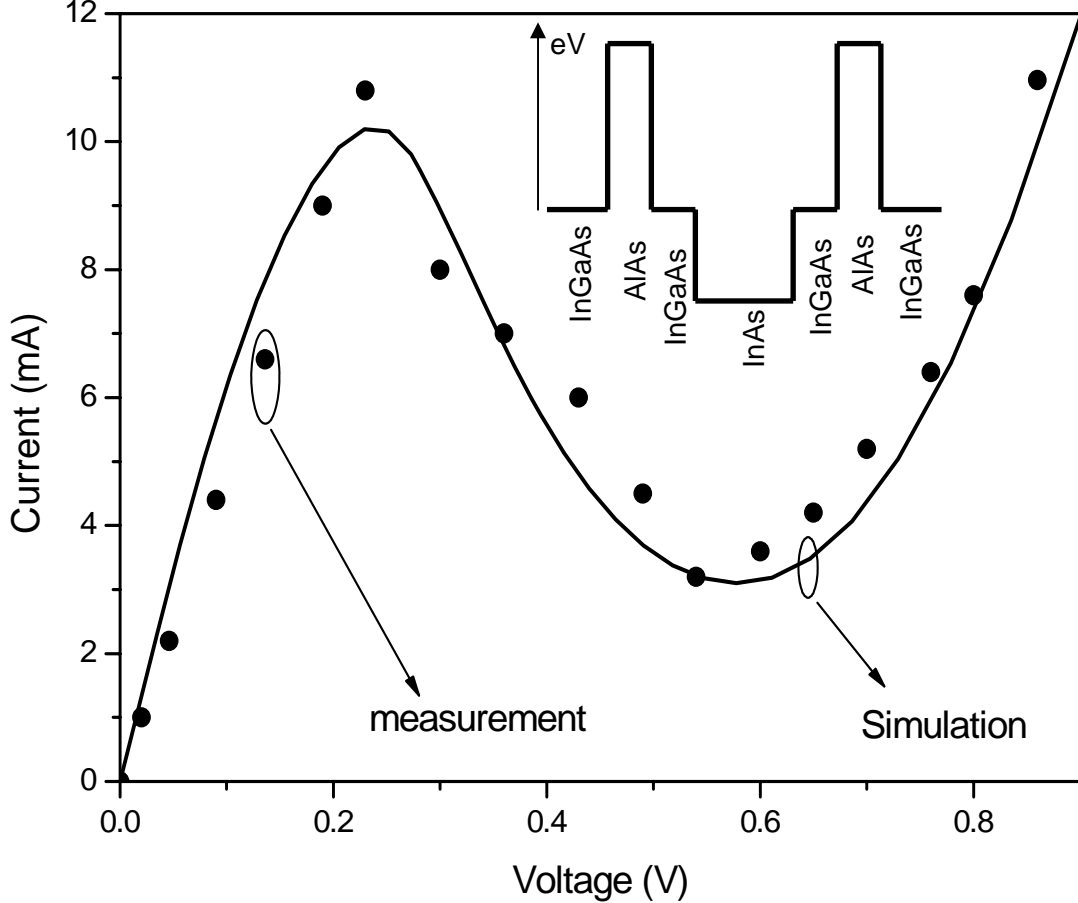


Figure 2.10: Here we represent the comparison of the measured [51] and our simulated static characteristics. The RTD studied by Auer et. al. [51] contains composite quantum well with relatively thin barriers. The active layer of the diode consists of undoped InAs layer as quantum well (2.5 nm) which is symmetrically sandwiched by InGaAs smoothing layers (1.2 nm), AlAs barrier layers (2.2 nm), undoped InGaAs spacers (1.5 nm), and heavily doped ( $1 \times 10^{18} \text{ cm}^{-3}$ ) InGaAs emitter and collector layers. In our simulation we are using the same nominal RTD parameters but the thickness of the barrier is changed to 2.0 nm. In the inset the conduction band diagram is shown.

We have simulated the published current-voltage characteristics from Broekaert et. al.

[16]. They were studying RTDs with assymmetric barriers and the diodes show multiple resonances.

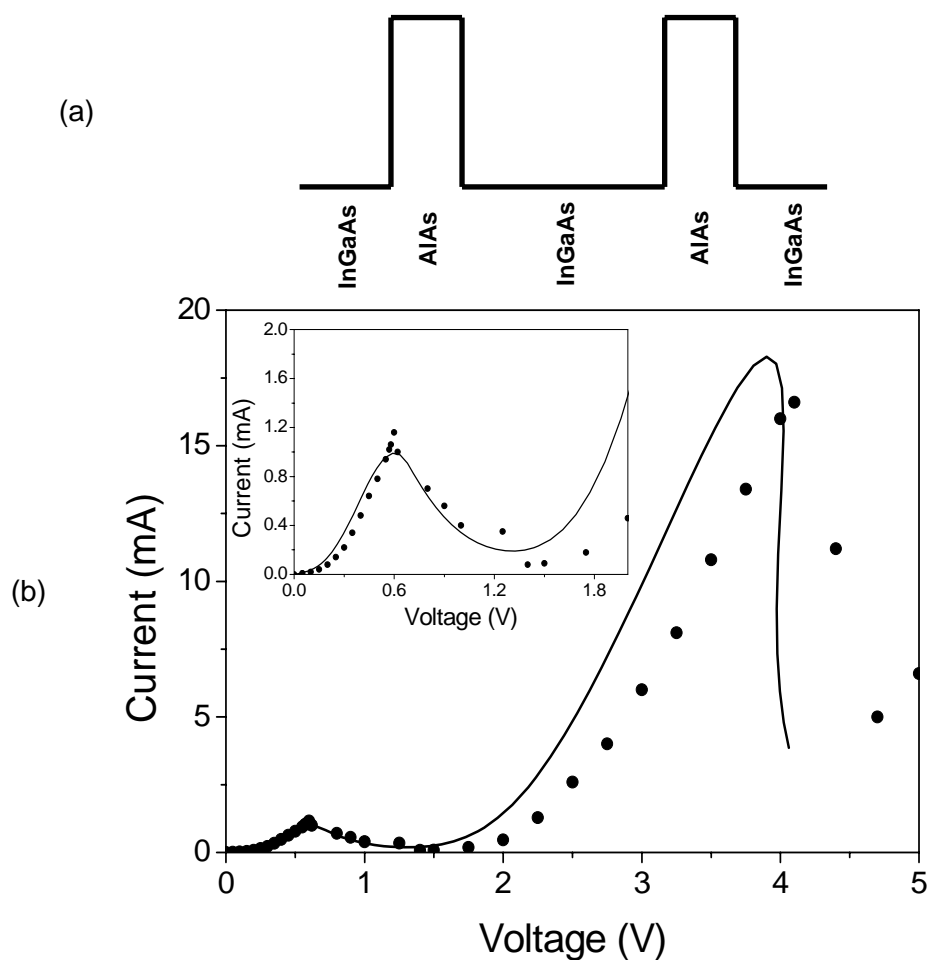


Figure 2.11: In this figure panel (a) shows the conduction band profile of the RTD. In panel (b) the static curves from Broekaert et. al. [16] is compared with our simulation. Their studied RTDs show two resonant peaks and consist of asymmetric barriers. The RTD contains a simple quantum well (5.6 nm  $In_{0.53}Ga_{0.47}As$  layer) with asymmetric barriers made of AlAs (2.4 nm emitter barrier and 3.0 nm collector barrier). The simulation is done with the same layer parameters as they reported. In the inset the simulated and measured first resonance is magnified.

Another RTD we have simulated taken from literatures, is the RTD studied by Eaves et. al. [41]. The RTD is made of GaAs/AlGaAs material system with asymmetric barriers.

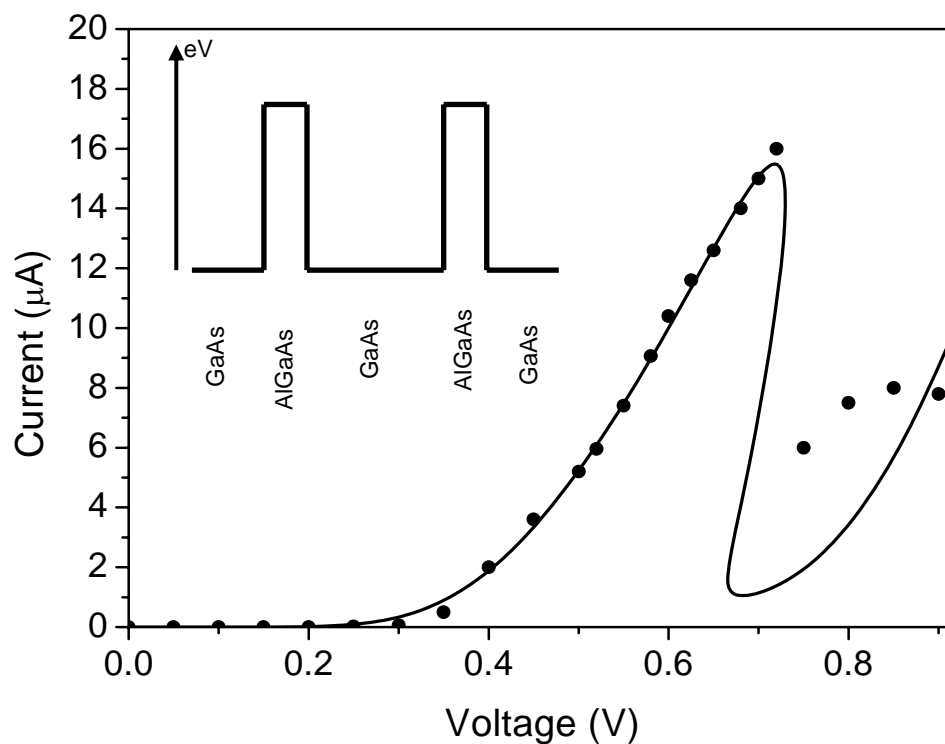


Figure 2.12: In this figure, the RTD studied by Eaves et. al. [41] is compared with our simulation. Their studied RTD is made of assymetric barriers. The RTD contains simple quantum well (5.8 nm *GaAs* layer) with assymmetric barriers made of *AlGaAs* (8.3 nm emiiter barrier and 11.1 nm collector barrier). Our simulation is done with 9.0 nm emitter barrier and 10.8 nm collector barrier. Otherwise the same layer parameters are used as reported in their work [41].

### 2.3.2 Our studied RTDs

Apart from the published RTD I-V characteristics, we have simulated various kind of RTDs those were studied during this thesis. The agreement achieved in between the simulation and measurement of the static curves of our RTDs is very good and simulation can reproduce the second resonance peak (where it exists) quite nicely. Here we report two different batches of RTDs and we call them as RTD1 and RTD2. The X-ray defined parameters and the parameters used for simulations are presented for RTD1 (table 2.1) and for RTD2 (table 2.2). The good match of experimental and simulated I-V curves from the batch of RTD1 allowed us to design the diodes required for our further study. The design criteria were the following. First, the RTDs should be stable in the NDC region of the I-V curve. The RTD currents have to be sufficiently low for that purpose. Second, the characteristic frequency (approximately  $1/\tau_d$ ) in the AC response should be sufficiently low around 1 GHz. We deliberately kept low characteristic frequency so that the devices can be measured without much technical complications using the available laboratory set ups. Our AC measurement set up can work upto 40 GHz of frequencies in case of wafer probe measurements. To satisfy both the conditions the barriers were chosen thick ( $\approx 3.5nm$ ) and the current density rather low. Collector is doped heavily in these diodes to see negative differential conductance at high frequencies [1] which is one of the major aim of this work. Different area devices ranging from  $5 \mu m^2$  upto  $45 \mu m^2$  were fabricated. The simulation and the measurement of current-voltage characteristic curves for the  $45 \mu m^2$  diode are shown (Fig. 2.15 for RTD1 and Fig. 2.16 for RTD2).

Composition	In	Ga	Al	Function	n-doping, $\text{cm}^{-3}$	Thickness (nm) by XRD study	Thickness used in simula- tions, nm
InGaAs	53	47		Contact	$1.0 \times 10^{18}$	50	50
InGaAs	53	47		Spacer		1.5	1.5
AlAs			100	Barrier		3.3	2.9
InGaAs	53	47		well		1.16	0.9
InGaAs	74	26		well		2.54	2.5
InGaAs	53	47		well		0.83	0.9
AlAs			100	Barrier		3.0	2.75
InGaAs	53	47		Spacer		1.5	1.5
InGaAs	53	47		Contact	$1.0 \times 10^{18}$	50	50

Table 2.1: Parameters of the layer structures of RTD1 in Fig. (2.15). The RTD layer structures used for fitting with the experimental I-V curve (Fig. 2.15) and the values as defined by XRD studies are compared here.

Composition	In	Ga	Al	Function	doping, $\text{cm}^{-3}$	Thickness (nm) by XRD study	Thickness (nm) used in simula- tions
InGaAs	53	47		Contact	$1.0 \times 10^{18}$	50	50
InGaAs	53	47		Spacer		1.5	1.5
AlAs			100	Barrier		3.6	3.35
InGaAs	53	47		well		1.96	1.5
InGaAs	74	26		well		3.41	2.8
InGaAs	53	47		well		0.75	1.5
AlAs			100	Barrier		3.5	3.2
InGaAs	53	47		Spacer		1.5	1.5
InGaAs	53	47		Contact	$1.0 \times 10^{18}$	50	50

Table 2.2: Comparison of the XRD defined parameters of RTD2 and the parameters used for the simulations of I-V curve (Fig. 2.16).

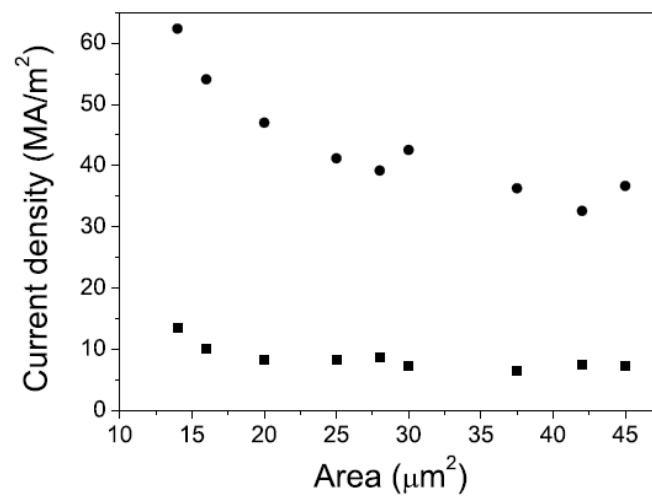


Figure 2.13: The current density vs. area of the diode for the batch of RTD1. The black points are the peak current densities ( $J_p$ ) and the black squares are the valley current densities ( $J_v$ ). RTDs ranging from  $5\mu m^2$  up to  $45\mu m^2$  were fabricated but they suffer from scaling problem. As it is evident from the plot with the decrease in area, the current density increases.

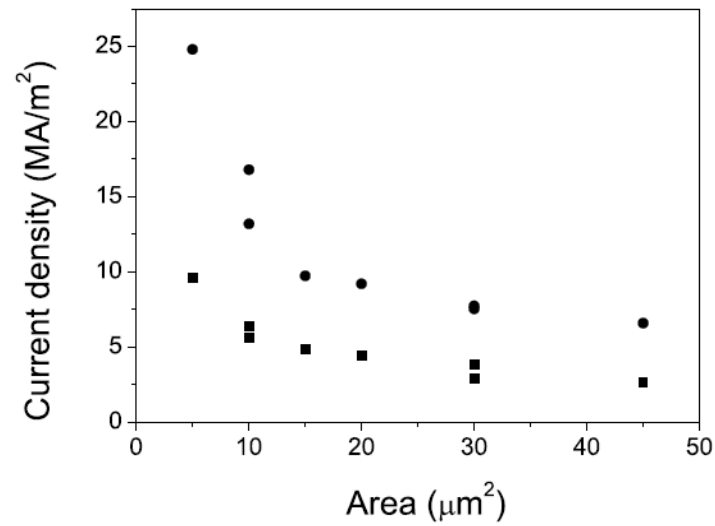


Figure 2.14: Current density of the diodes are plotted against the device area for the batch of RTD2. The black points are the peak current densities ( $J_p$ ) and the black squares are the valley current densities ( $J_v$ ). Different area diodes ranging from  $5\mu\text{m}^2$  upto  $45\mu\text{m}^2$  were fabricated. But these diodes too suffer from the similar current density scaling problem as RTD1.

Both the batches (RTD1 and RTD2) face current density scaling problem. As area of the device decreases the current density through the diodes increases (Fig. 2.13 and 2.14). The RTDs with smaller area has larger current density when compared to the large area RTDs. As it is evident from the plots (figures 2.13 and 2.14) the peak and valley current density both behave in the similiar way. The reasons for such strange behavior of the fabricated RTDs are not clear to us. The scaling problem is more severe for the smaller area diodes. But for the larger area (close to  $45\mu m^2$  diode area) diodes current density remains almost constant (Fig. 2.14). So for consistency we decided to measure the diode with the maximum area. The simulated and measured static characteristics for  $45\mu m^2$  area diodes are shown in figure 2.15 for RTD1 and in figure 2.15 for RTD2. The I-V curves for the batch of RTD2 (Fig. 2.16) show two resonance peaks indicating the current conduction through the second resonant state in the quantum well. Barrier thicknesses in RTD1 (table 2.1) are relatively thinner than RTD2 (table 2.2). So the current density was high and NDC there was not stable (Fig. 2.15).

The level broadening of the QW resonant state, we have considered for our RTDs are around 15 meV. For the batch of RTD2, the time spend by the electron in the QW is around 100 pS (i.e.  $\tau_d$ ). From Heisenberg's uncertainty principle, the resonant state level broadening due to the finite resonant state lifetime is  $\Delta E = \hbar/\tau_d$ . So, calculated value of  $\Delta E$  is  $\approx 0.0066$  meV. In addition to that, the junctions in between the QW and the barriers are not smooth (because of technological limitation) but non-uniform. Because of this non-uniformity of the layers, the energy level broadening is more than the value due to the finite lifetime of the resonant state. There is no direct method to estimate this value of level broadening. For example, in the work of Mattia et. al. [36], they considered approximately 12.5 meV as resonant state level broadening. The value of level broadening, they used includes other factors contributing to level broadening in addition to the finite resonant state lifetime. So, the values we are using in our simulation are quite reasonable. In reality, the electron effective mass in the QW is more than that in the emitter. This fact affects the NDC region of the RTD static characteristic (I have discussed this factor later in this chapter). So, if one considers the effect of the effective mass difference, then the value of the resonant state level broadening should be different than what we have used in the static simulations (Fig. 2.15 and 2.15).



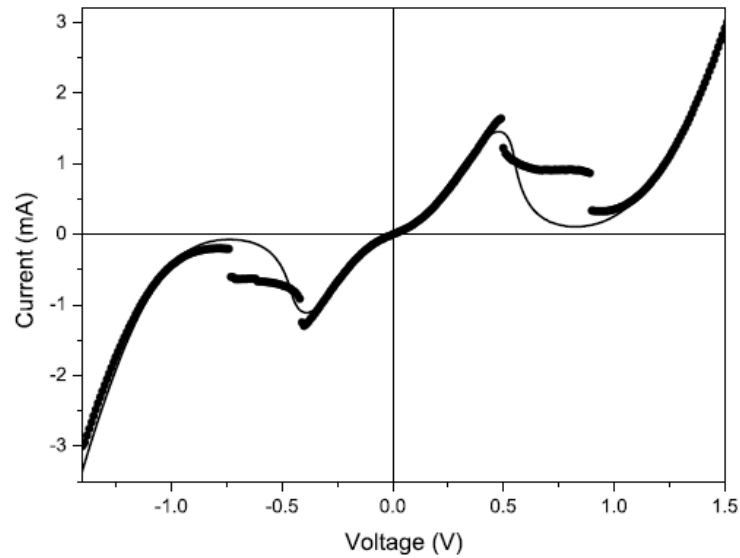


Figure 2.15: The measured and simulated I-V characteristics of the fabricated diodes. The XRD defined RTD layer parameters and the parameters used for simulation are mentioned in table 2.1. The level broadening used for the simulation is  $\approx 20$  meV.

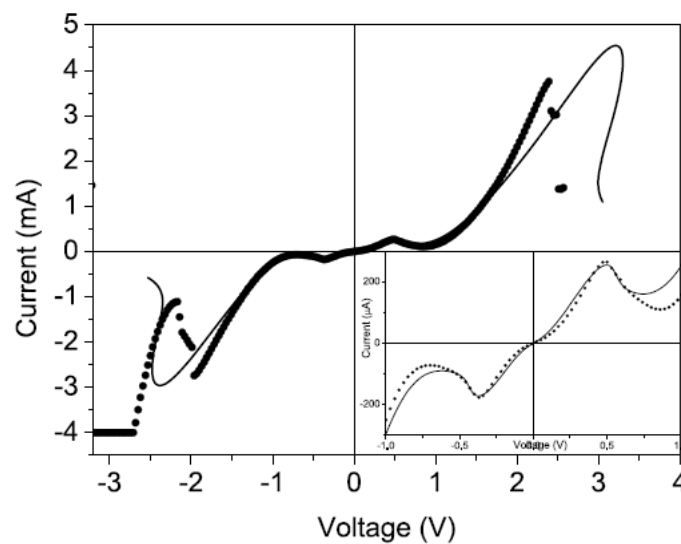


Figure 2.16: Measured and simulated I-V characteristics of our designed diodes. The diodes have two resonance peaks and simulation can reproduce both of them. The first resonance is magnified in the inset. The RTD parameters used for simulations and revealed from XRD study of the calibration test structures are mentioned in table 2.2. The resonant level broadening used is  $\approx 15$  meV.

### 2.3.3 Simulation of RTD parameters

The different parameters involved in the operation of RTD are simulated. The purpose is to see the qualitative nature of the RTD parameters with the applied bias. The example considered here is the batch of RTD2 (Fig. 2.16) in forward bias which contains relatively thick barriers. With the increase in bias the well-emitter escape rate ( $\nu_e$ ) decreases but the well-collector escape rate ( $\nu_c$ ) increases (Fig. 2.17). As more bias is applied the electron trying to cross the emitter barrier faces higher barrier, hence  $\nu_e$  decreases. Whereas the electron trying to cross the collector barrier sees lower barrier which results into increase of  $\nu_c$ .

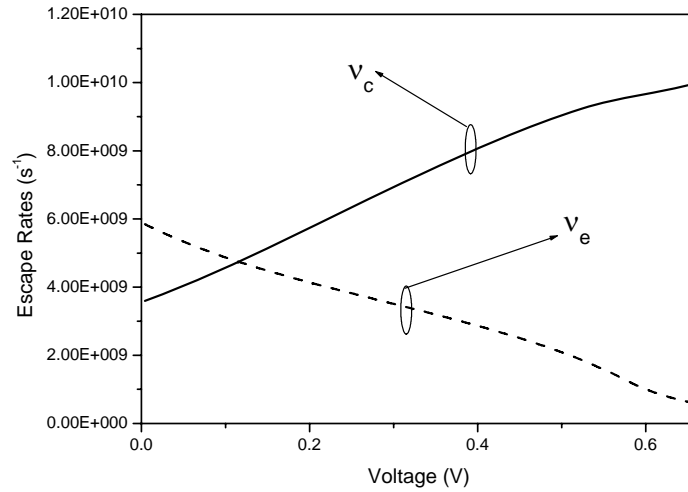


Figure 2.17: The bias dependent quantum well to emitter electron escape rate ( $\nu_e$ ) and the well to collector escape rates ( $\nu_c$ ) for RTD2 (2.16) in the forward biasing conditions.

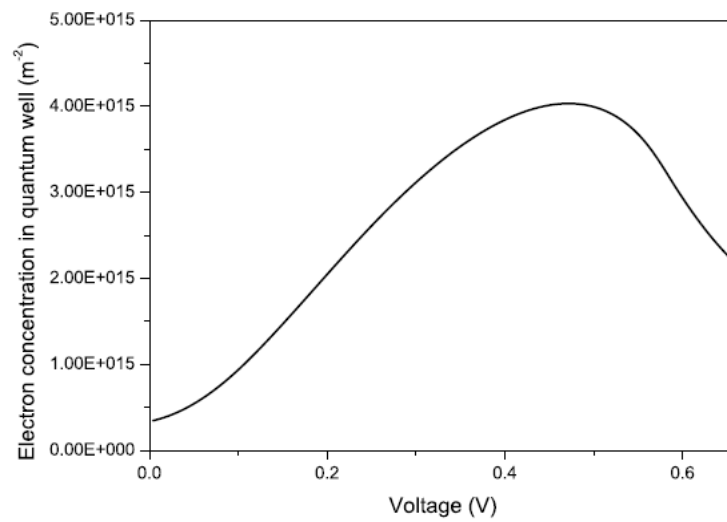


Figure 2.18: Simulation of electron concentration in the quantum well of RTD2 in the forward applied bias (Fig. 2.16).

The bias dependent 2DEG concentration in the quantum well are simulated (Fig. 2.18). Electron concentration in QW ( $N_{2D}$ ) increases with the increase in applied voltage in the PDC region and in the NDC region it starts to decrease with the increase of bias. The behavior of convergence of our simulator is also studied. The number of iterations required to achieve the desired accuracy is bias dependent. Strictly speaking it depends on the concentration of quantum well electrons. More the concentration more iterations are required. For a relative error of  $10^{-9}$  in the concentration of quantum well electrons the number of iterations required is plotted against the applied bias.

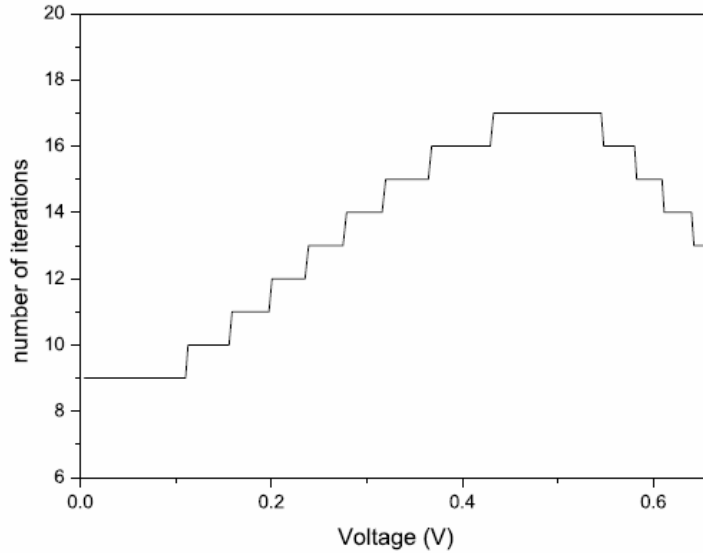


Figure 2.19: Number of iterations required to achieve a relative accuracy of  $10^{-9}$  in terms of electron concentration in the quantum well for RTD2 (Fig. 2.16) in the forward biasing conditions.

## 2.4 RTD model when emitter and QW electron mass differs

The current versus voltage simulation done before in this work considers same electron effective mass in emitter and quantum well. If the material in the emitter and in the well are different then naturally the electron masses are different in those regions. Even if same material is used in the emitter and QW the electronic masses can differ because of

the non-parabolicity effect. For our RTDs the effective electron mass in the emitter is less than the effective electron mass in the QW. In the emitter the effective electron mass is the electron mass at the conduction band bottom. But in the QW the electron effective mass corresponds to its value at the quantum confined state and it is larger because of the increased bandgap (Fig. 2.20). The relation of the electron mass at the quantum confined state with the value at the conduction band edge due to the non-parabolicity is,

$$m^* = m_c \frac{E'_g}{E_g}, \quad (2.26)$$

The situation is illustrated in the figure (2.20).

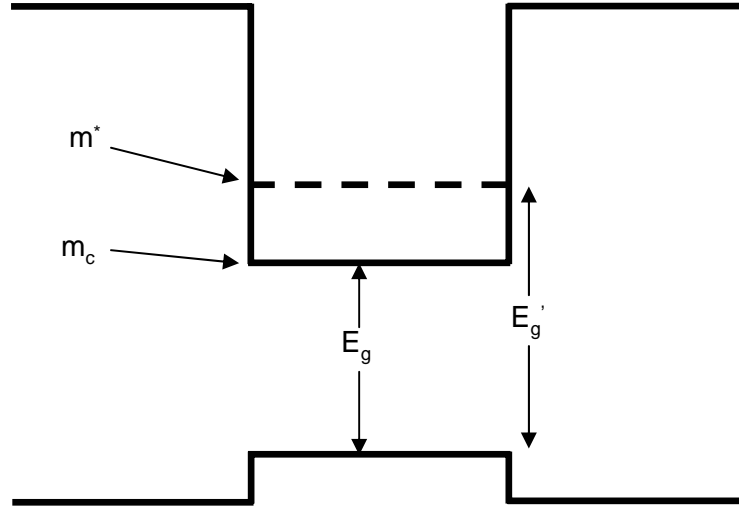


Figure 2.20: Here  $m^*$  and  $m_c$  are the electron effective masses at the quantised state and at the conduction band bottom respectively.  $E_g$  and  $E'_g$  are the effective band gaps at the conduction band bottom and at the quantised state. In the QW,  $E'_g$  is greater than  $E_g$  so effective electron mass ( $m^*$ ) is greater than its value at the conduction band edge ( $m_c$ ).

The effect of different electron effective masses in the QW and in the emitter, are demonstrated in the simulations of Ohno et. al. [66] and by Schulman [67]. Generally in the current voltage simulation the basic assumption is effective electron mass in the emitter and QW are same. The case of same electron effective mass in the emitter and QW is illustrated in the figure 2.21. In the situation  $m_e = m_w$ , all the quantum well states with

energy in the  $z$ -direction equal to  $U_w$  are eligible for tunneling. When  $U_w = E_{fe}$  the electronic states in the QW start to find electronic states in the emitter which are conserved in momentum and energy hence resonant tunneling current starts to flow (situation A of the current-voltage plot from the inset of figure 2.21). The maximum tunneling through RTD takes place in the situation  $U_w \rightarrow 0$  giving rise to peak current (situation B from inset of figure 2.21). If bias is increased further  $U_w$  goes lower than  $E = 0$  and the whole QW dispersion curve goes out from the emitter Fermi sea. Thus making no electronic states in the QW available for tunneling keeping energy and momentum conserved anymore so RTD current drops to zero (situation C of the current-voltage plot from the inset of figure 2.21).

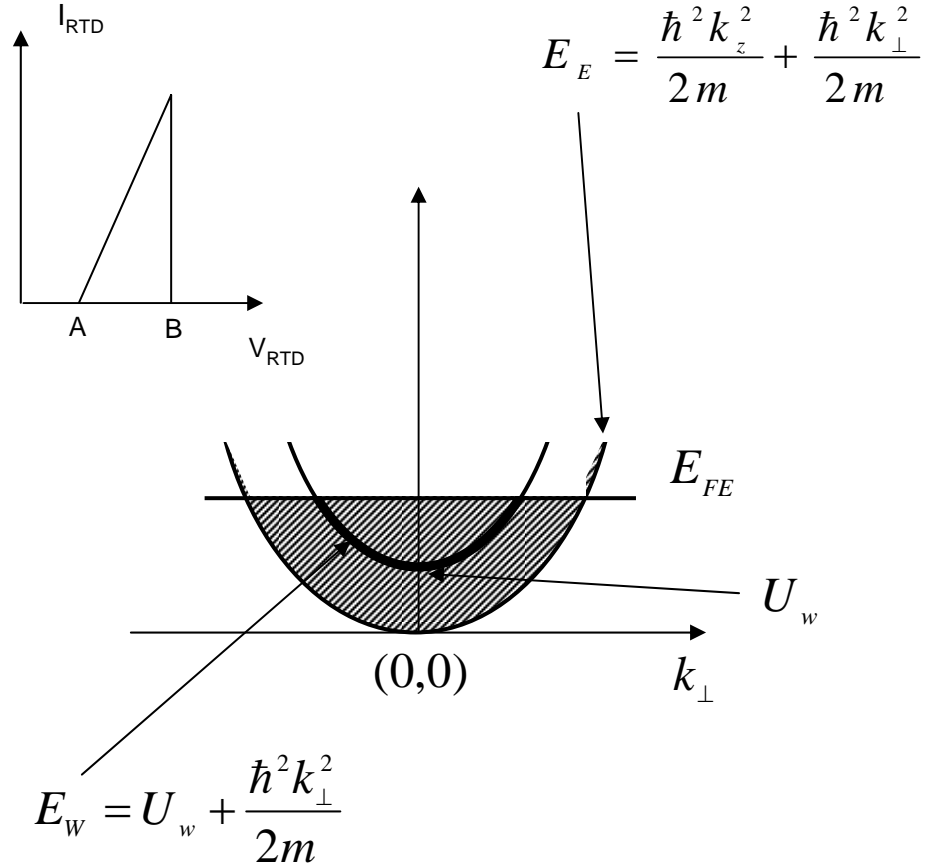


Figure 2.21: Energy versus transverse momentum ( $k_{\perp}$ ) plots for RTDs when the electron effective mass in emitter and QW are same i.e.  $m_e = m_w = m$ . Here  $E_E$  and  $E_W$  stands for the total energy of electron in the emitter and QW. The hashed portion describes the Fermi sea of electrons in the emitter and the thick bold curve describes the electronic states in the QW those are eligible for tunneling. Inset shows the qualitative current voltage characteristic in case of  $m_e = m_w$  without including the effect of resonant state level broadening.

This simple picture isn't applicable when electron effective masses are different in QW and emitter. Because of the difference in electron effective masses the  $E$  vs.  $k_{\perp}$  dispersions are different for emitter and QW electrons. So the number of electrons which can tunnel resonantly changes. The situation is depicted schematically in the figure 2.22. Similar to the situation  $m_e = m_w$  the RTD current starts to flow when  $U_w = E_{FE}$  (situation A of the current-voltage plot from the inset of figure 2.22). But the maximum tunneling through RTD takes place when  $U_w = (1 - m_e/m_w)E_{FE}$  since the maximum number of states in the QW is in resonant condition (situation B of the I-V curve of the inset in figure 2.22). If bias is increased even more  $U_w$  lowers down and number of electronic states in the QW through which resonant tunneling can be permissible reduces so  $I_{RTD}$  decreases. Further increase in bias drops down  $U_w$  below  $E = 0$  so that no electronic states in the QW are available for tunneling anymore hence RTD current drops to zero (situation C of the I-V curve of the inset in figure 2.22). The fact that  $m_e < m_w$  affects the peak voltage of RTD static characteristic (from figures 2.21 and 2.22).



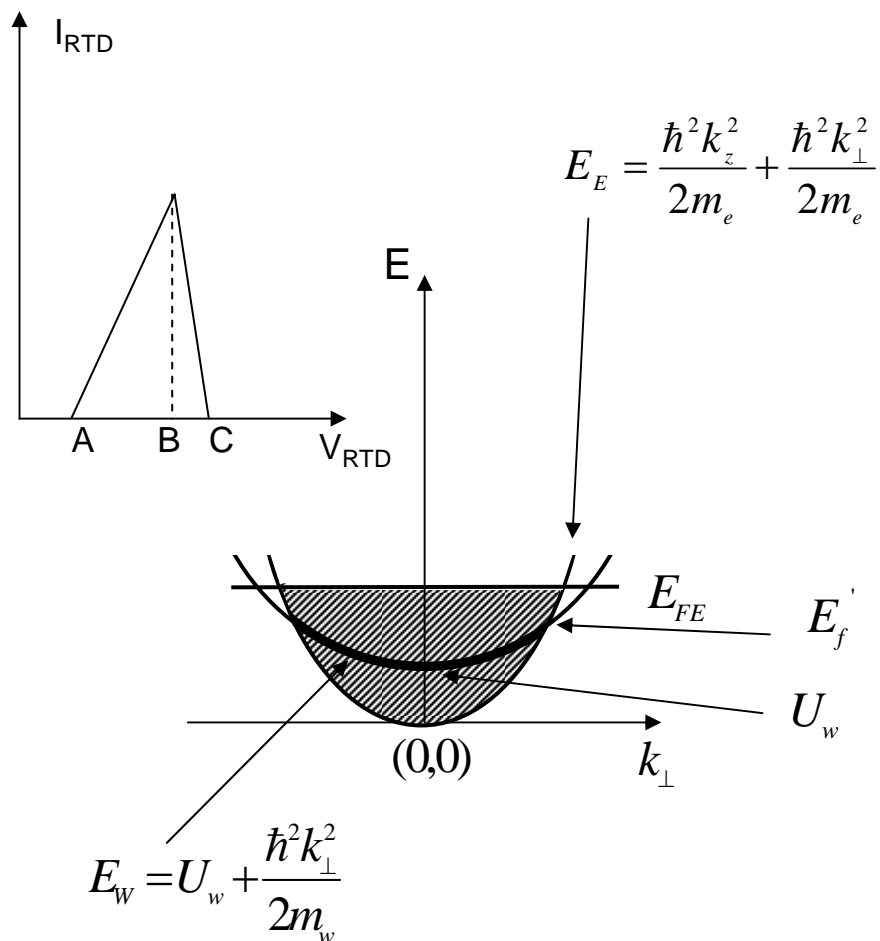


Figure 2.22: Energy versus transverse momentum ( $k_{\perp}$ ) plots for RTDs when the electron effective mass in emitter is less than the electron effective mass in the QW i.e.  $m_e < m_w$ . Here  $E_E$  and  $E_W$  stands for the total energy of electron in the emitter and QW. The hashed portion describes the Fermi sea of electrons in the emitter and the thick bold curve describes the electronic states in the QW that eligible for tunneling.

Next we formulate the current density expression for the emitter to well resonant current density component. Considering the available states in the QW through which tunneling can be possible, the forward emitter to well current density expression is,

$$J_{ewF} = \int_{U_w}^{\infty} e\rho_{2De}f_e(E)\nu_e(E)dE, \quad (2.27)$$

Here  $\rho_{2De}$ ,  $f_e(E)$  and  $\nu_e(E)$  are 2D density of states in the emitter, Fermi distribution function of the emitter electrons and emitter barrier tunnel transparency as a function of energy respectively. But because of the different effective masses in the emitter and QW, all states in the QW are not eligible for tunneling. The states upto  $E'_{fe}$  (Fig. 2.22) are eligible through which tunneling is permissible. The states for which  $E > E'_{fe}$  do not participate in tunneling. So, in the integration of relation 2.27 the upper limit is changed to  $E'_{fe}$  in place of  $\infty$  and we get the emitter to well forward current density as,

$$J_{ewF} = \int_{U_w}^{E'_f} e\rho_{2De}f_e(E)\nu_e(E)dE, \quad (2.28)$$

$E'_f$  is defined as the maximum total energy of the electron upto which the tunneling is possible conserving the in plane momentum and total energy. Quantitatively,  $E'_f$  is defined as the intersection of the two dispersion curves for electrons in the emitter and in the QW. Thus,  $E'_f$  is defined as  $E'_f = U_w / (1 - m_e/m_w)$ .

Similarly, the relation for backward emitter-well current density is,

$$J_{ewR} = \int_{U_w}^{E'_f} e\rho_{2Dw}f_w(E)\nu_e(E)dE, \quad (2.29)$$

Here  $\rho_{2Dw}$  and  $f_w(E)$  are the 2D density of states in the QW and the Fermi distribution of electrons in the QW. Finally, the net current density across the emitter-well barrier becomes,

$$J_{ew} = \int_{U_w}^{E'_f} e\rho_{2De}f_e(E)\nu_e(E)dE - \int_{U_w}^{E'_f} e\rho_{2Dw}f_w(E)\nu_e(E)dE, \quad (2.30)$$

The fact that  $m_e < m_w$  basically modifies the emitter-well resonant current density expression ( $J_{ew}$ ). The well-collector current density ( $J_{wc}$ ) remain same since across the collector barrier simple tunneling takes place.

$$J_{wc} = \int_{U_w}^{\infty} e \rho_{2Dw} f_w(E) \nu_c dE, \quad (2.31)$$

The relation for emitter-well current density can not be solved analytically (eq. 2.30) since  $\nu_e(E)$  depends on energy ( $E$ ) unlike the case when  $m_e = m_w$  (The derivation of  $\nu(E)$  is shown in the Appendix). Hence we solve,  $J_{ew}$  numerically here. The physical effects considered for the static simulation here and the algorithm of the simulator remains same according as our previous static simulation (2.8). Considering the fact that  $m_e < m_w$  the static simulation is done for the measured I-V curve for a  $45 \mu m^2$  diode from the group of RTD2 (Fig. 2.23).

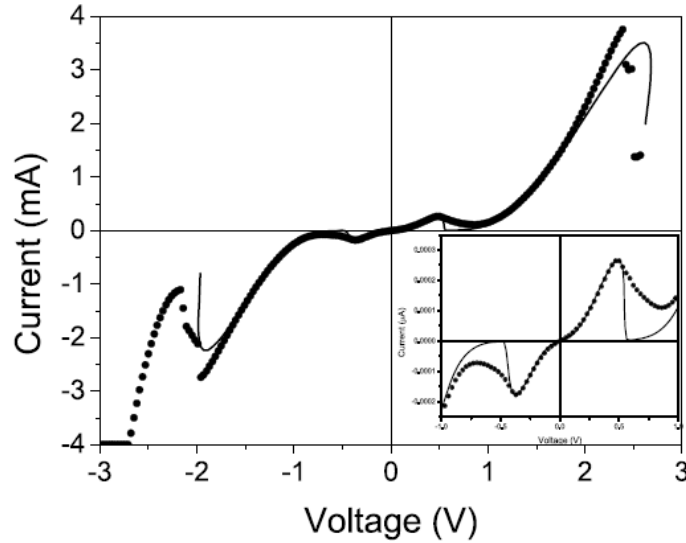


Figure 2.23: Simulation of static characteristics of a  $45 \mu m^2$  diode taken from the batch of RTD2 considering different effective electron mass in the well and emitter. For simulations the RTD parameters are considered to be the same (Fig. 2.16 and table 2.2) except the well width is considered here as 5.6 nm for better match in between the simulation and experiment. Although onset of the 2nd resonances are matching well for both the forward and reverse bias conditions but the NDC isn't reproduced well by the simulation since level broadening isn't considered in this simulation.

## 2.5 Conclusions

In this chapter, we have demonstrated the development of a simple and fast but effective self consistent simulator for RTD depending on sequential tunneling approximation [7]. The various physical effects are considered in our self-consistent model. The developed simulator can reproduce very well the experimental static curves of several RTDs having different features (thin and thick barriers, simple and composite quantum well, single and multiple resonances in I-V characteristics). The diodes used for the verification of the static simulator are taken from literatures and fabricated during the course of this thesis work. The developed static model is further extended for the situation when the electron effective mass in the emitter and QW are different.

## Chapter 3

# Simulation of dynamic behavior of RTD

This chapter describes the AC behavior of RTD. First, we will describe the existing theoretical small signal model [1, 44]. For the AC analysis of our present diodes (AC behavior are studied in details in chapter 4), we will use this existing model [1, 44]. Because of the presence of 2DEG in the QW the experimental low frequency capacitance of RTD has some special features. It (low frequency RTD capacitance) can be less [36] or more [41, 43] than the simple emitter-collector depletion capacitance in the PDC region and has a peak in the NDC region (in Fig. 3.1 the low frequency capacitance measurements by Eaves are shown). We have formulated a simple analytical expression in terms of the geometrical parameters of RTD for low frequency RTD capacitance in the PDC region of I-V characteristic where the derived analytical expression is a direct consequence of the old model [1, 44]. The derived small signal model [1, 44] doesn't consider the backflow of electrons from collector to quantum well. This assumption is valid well when collector contains long spacer and Fermi level in the collector side is lower than the ground state of the QW. In case collector side Fermi level is higher than the bottom of the 2D subband in the QW then one needs to consider the backflow of electron from collector to QW. Examples of such type of RTDs are available in literatures [46, 51]. In order to model the dynamic behaviors of such RTDs accurately, we have consider the backflow of electrons from collector to QW and extended the already developed small signal model [1, 44]. Further we will discuss in this chapter the consequences of such extension.

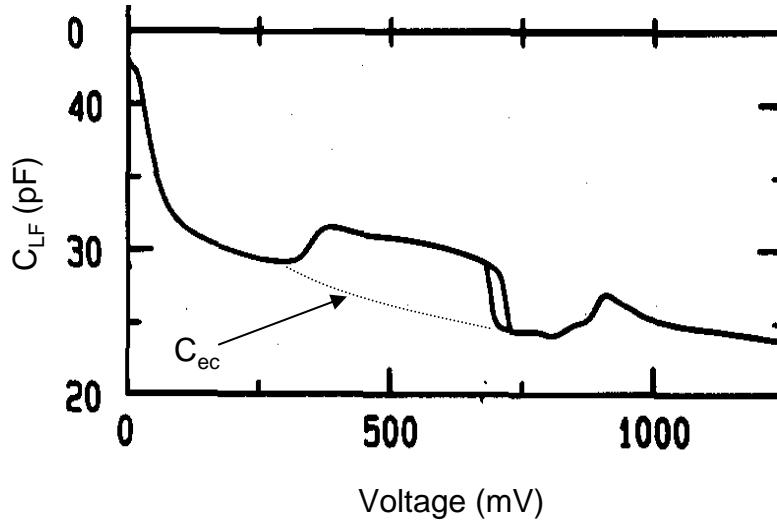


Figure 3.1: The low frequency capacitance measurement of the RTDs from Eaves et. al. [41]. In the PDC region, the measured capacitance is more than the simple emitter-collector geometrical capacitance ( $C_{ec}$ ).

### 3.1 Introduction to the developed AC model

Huge number of equivalent circuits [1, 39, 2, 46, 42, 36, 43] are proposed for RTD in last several decades. Most of the models suffer from some shortcomings. Gering et. al. [39] introduced an inductance in the RTD equivalent circuit but the origin of the inductance isn't clear. The model from Brown became very famous [68] and many people later used it but the fact that RTD capacitance at low frequency can be less or more than emitter-collector capacitance cannot be reproduced by this model. The small signal model derived by Sheard et. al. does not consider the Coulomb interaction effect and the variation of tunnel transparencies with bias is also ignored. One of the recently developed model [46] is basically same with the model derived by Brown [2]. The small signal model of Genoe et. al. [43] are comprehensive and general but the model is not simple for analytical analysis. The analytically derived model [1, 44] is very simple and it also gives a better insight on RTD operation. The model is derived considering the sequential tunneling mechanism. There are mainly three important outcome of this theoretical model. First, it says resonant tunnelling exist beyond the inverse of quasi-bound-state lifetime limit against the general perception; second, RTD response time isn't limited by the quasi-

bound-state (resonant state) lifetime which is a consequence of Coulomb interaction of electrons in RTD; and third, a simple small signal equivalent circuit model is proposed for RTD (Fig. 3.2). For the admittance simulations of our RTDs we are going to use this small signal model (Fig. 3.2).

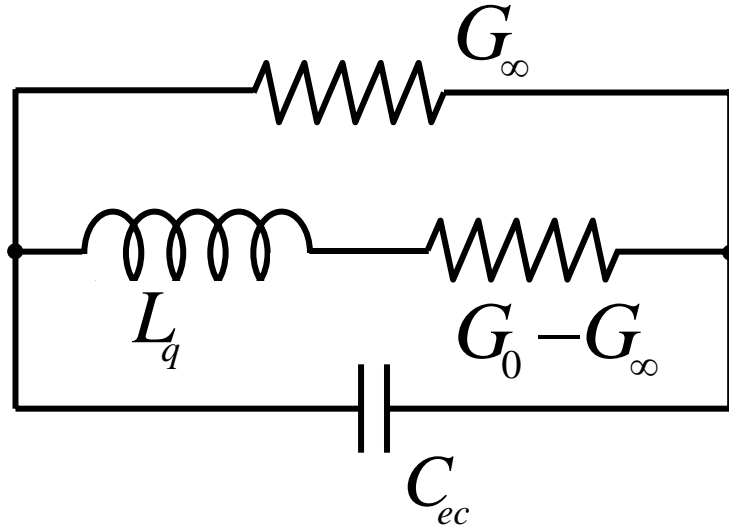


Figure 3.2: The derived small signal equivalent circuit of RTD [1, 44]. This equivalent circuit is used for the simulation of AC measurements done.  $G^0$  and  $G^\infty$  are the static and high frequency conductances of RTD, respectively.  $C_{ec}$  is the emitter-collector depletion capacitance.  $L_q$  is the quantum inductance and it is defined as  $L_q = \tau_{resp}/(G^0 - G^\infty)$ .

The admittance of the theoretically developed simple RTD equivalent circuit (Fig. 3.2) is represented as [1],

$$G(\omega) = G^0 + \frac{G^0 - G^\infty}{1 + i\omega\tau_{resp}} + i\omega C_{ec}, \quad (3.1)$$

where  $G^0$  and  $G^\infty$  are static conductance and high frequency conductance of RTD, respectively.  $\tau_{resp}$  is the RTD response time and  $C_{ec}$  is the emitter-collector capacitance.

The expressions for  $\tau_{resp}$ ,  $G^0$  and  $G^\infty$  are as follows [1],

$$\frac{1}{\tau_{resp}} = \nu_e + \nu_c + \beta(\nu_e - (E_{fe} - U_w - \frac{N_{2D}}{\rho_{2D}})\nu'_e(V_{we}) + \frac{N_{2D}}{\rho_{2D}}\nu'_c(V_{wc})), \quad (3.2)$$

$$G^0 = \nu_c C_{wc} \left(1 - \frac{\tau_{resp}}{\tau_d}\right), \quad (3.3)$$

$$G^\infty = \frac{d}{d+l} C_{wc} \left(\frac{1}{\tau_{resp}} - \frac{1}{\tau_d}\right) + \frac{l-d}{l+d} e^2 N_{2D} \nu'_c(V_{wc}), \quad (3.4)$$

here  $C_{ec} = \epsilon/(d+l)$  is emitter-collector capacitance per unit area and  $C_{wc} = \epsilon/l$  is the well-collector capacitance per area.  $\epsilon$  is the permittivity of the material and defined as  $\epsilon = \epsilon_r \epsilon_0$  where  $\epsilon_r$  and  $\epsilon_0$  are the relative permittivity and the permittivity of the free space, respectively.  $\nu'_e(V_{we})$  is the variation of emitter barrier transparency ( $\nu_e$ ) with the bias across the emitter barrier ( $V_{we}$ ) and  $\nu'_c(V_{wc})$  variation of collector barrier transparency ( $\nu_c$ ) with the bias across the collector barrier ( $V_{wc}$ ).

## 3.2 Behavior of low frequency RTD capacitance

### 3.2.1 Theoretical analysis

The RTD equivalent circuit derived [1] before is general and applied for all frequencies. In the low frequency limit (i.e.  $\omega\tau_{resp} \ll 1$ ) the equivalent circuit can be simplified to a simple RC circuit as,

$$G_{LF} \approx G^0 + i\omega[C_{ec} + \tau_{resp}(G^\infty - G^0)], \quad (3.5)$$

where the effective low frequency capacitance is,

$$C_{LF} = C_{ec} + \tau_{resp}(G^\infty - G^0), \quad (3.6)$$

The above expression for capacitance in the low frequency limit is general and valid in the PDC as well as in the NDC region of I-V characteristics. But for the time being we concentrate on its analysis in the PDC region because it has been experimentally shown that the low frequency RTD capacitance in the PDC region can be more [41, 43] (Fig. 3.1) or less [36] than the simple emitter-collector capacitance ( $C_{ec}$ ). Here we formulate a simple analytical relation for RTD capacitance at low frequencies depending on the previously developed model (relation 3.1) [1].



It has been shown, previously [1] that for the PDC region the approximations  $\nu_e \gg (E_{fe} - U_w - \frac{N_{2D}}{\rho_{2D}})\nu'_e$  and  $\nu_c \gg \frac{N_{2D}}{\rho_{2D}}\nu'_c$  are valid well. Hence, the response time (relation 3.2) can be approximated as,

$$\frac{1}{\tau_{resp}} = \nu_e + \nu_c + \beta\nu_e, \quad (3.7)$$

So the low frequency conductance ( $G^0$ ) and the high frequency conductance ( $G^\infty$ ) in the PDC region take the following forms,

$$G^0 = \nu_c C_{wc} \frac{\beta\nu_e}{\nu_e + \nu_c + \beta\nu_e}, \quad (3.8)$$

and

$$G^\infty = \frac{d}{d+l} C_{wc} \beta\nu_e + \frac{l-d}{l+d} e^2 N_{2D} \nu'_c, \quad (3.9)$$

The high frequency conductance ( $G^\infty$ ) can be further written in another form as,

$$G^\infty = \frac{d}{d+l} \beta C_{wc} \nu_e \left( 1 + \frac{l^2 - d^2}{d^2} \frac{N_{2D} \nu'_c}{\rho_{2D} \nu_c} \right) \quad (3.10)$$

In case of RTDs with  $d \approx l$ , the second term in relation 3.10 can be neglected compared to unity (i.e. the first term). In the opposite situation i.e.  $l \gg d$ , the ratio of the second term to the first term is 0.08, for  $l/d \approx 5$  (e.g. Mattia's RTD [36] where they used long spacer in the collector side). Hence for the PDC region high frequency conductance can reasonably simplified as,

$$G^\infty = \frac{d}{d+l} \beta C_{wc} \nu_e, \quad (3.11)$$

Using the simplified expressions for  $\tau_{resp}$  (relation 3.7),  $G^0$  (relation 3.8) and  $G^\infty$  (relation 3.11) along with the low frequency RTD capacitance expression (relation 3.6) we get,

$$C_{LF} = C_{ec} + \frac{C_{wc}\beta}{\beta + \gamma + 1} \left[ \frac{d}{d+l} - \frac{\gamma}{\beta + \gamma + 1} \right], \quad (3.12)$$

Here  $\gamma$  is the ratio of collector barrier transparency to emitter barrier transparency i.e.  $\gamma = \nu_c/\nu_e$ . So, low frequency RTD capacitance ( $C_{LF}$ ) is represented with a simple expression and in terms of RTD physical parameters (relation 3.12). From RTD capacitance relation

(3.12), it clearly seen that the RTD capacitance in the PDC region differs from the simple emitter-collector ( $C_{ec}$ ) geometrical capacitance (Figure 3.3 shows the deviation of low frequency capacitance in case of the RTD studied by Mattia et. al. [36]). Now let us examine the different limiting cases with the help of the expression for RTD low frequency capacitance (3.12). The ratio of  $C_{LF}/C_{ec}$  is the following,

$$\frac{C_{LF}}{C_{ec}} = 1 + \frac{\beta}{\beta + \gamma + 1} \left[ \frac{d}{l} - \frac{d+l}{l} \frac{\gamma}{\beta + \gamma + 1} \right], \quad (3.13)$$

In the case of  $\gamma \rightarrow 0$ , the ratio ( $C_{LF}/C_{ec}$ ) takes the form,

$$\frac{C_{LF}}{C_{ec}} = 1 + \frac{\beta}{\beta + 1} \frac{d}{l}, \quad (3.14)$$

When  $\gamma = (1 + \beta)d/l$ , the ratio of  $C_{LF}/C_{ec}$  (from relation 3.13) becomes unity (it means measured low frequency capacitance is equal to  $C_{ec}$ ).

The ratio  $C_{LF}/C_{ec}$  has a minimum when  $\gamma = (1 + \beta)(1 + 2d/l)$ , and the minimum value is,

$$\frac{C_{LF}}{C_{ec}} = 1 - \frac{1}{4} \frac{\beta}{\beta + 1} \frac{l}{d+l}, \quad (3.15)$$

At the other extreme situation, when  $\gamma \rightarrow \infty$ , from relation (3.13),

$$\frac{C_{LF}}{C_{ec}} = 1, \quad (3.16)$$

that means the measured RTD low frequency capacitance ( $C_{LF}$ ) is again the emitter-collector ( $C_{ec}$ ) capacitance. The variation of low frequency capacitance for different emitter-well ( $d$ ) and well-collector ( $l$ ) lengths are shown in figure (3.3).

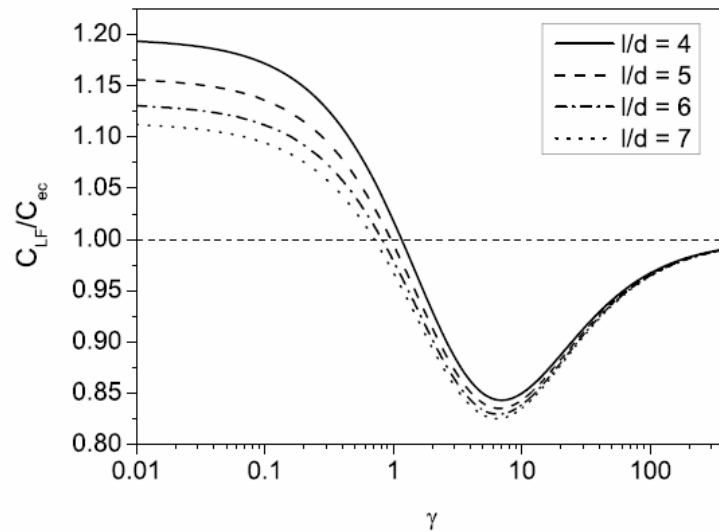


Figure 3.3: The ratio of low frequency capacitance ( $C_{LF}$ ) with emitter-collector capacitance ( $C_{ec}$ ) is plotted against  $\gamma$  ( $= \nu_c/\nu_e$ ) from our analysis (eqn. 3.12) for the RTD studied by Mattia et. al. [36] for different ratio of  $d/l$ .

### 3.2.2 Comparison with measurement

In the low frequency limit, RTD admittance can be approximated by a simple RC circuit (relation 3.5), where the susceptance part can be represented as a capacitance. This low frequency effective capacitance of the batch of RTD2 (static curves are shown in Fig. 2.16) for forward and reverse biasing conditions are studied by measurement and simulation (Fig. 3.4) and (3.5). The capacitance simulations are done here considering the developed RTD AC model ( Fig. 3.2, [1, 44]), using the same RTD layer parameters (table - 2.2) as used for the static characteristic simulations (Fig. 2.16).

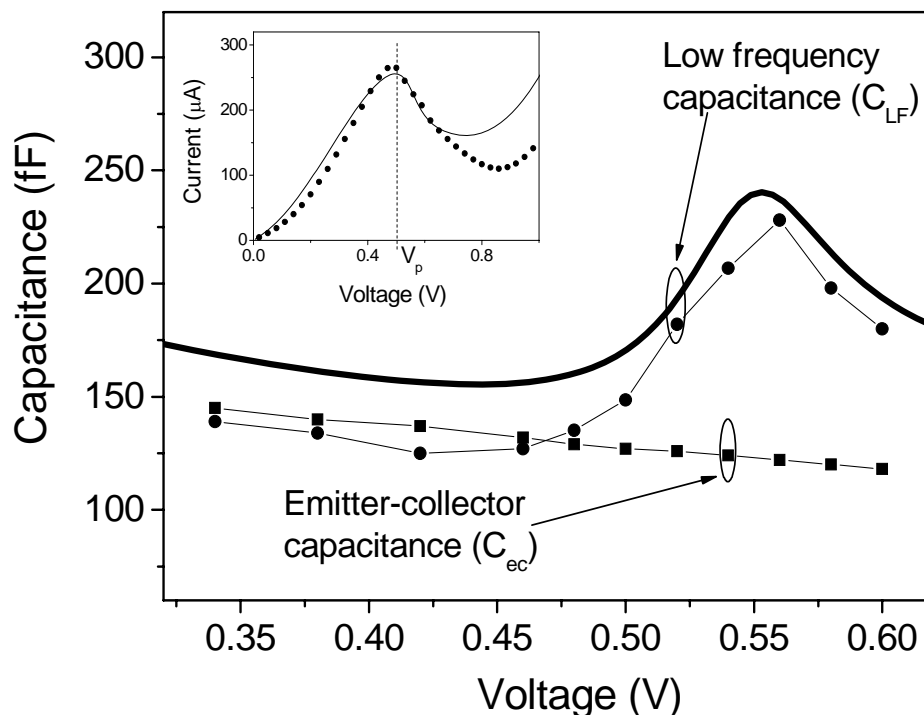


Figure 3.4: The measured and simulated RTD capacitance at different voltages in the forward biasing conditions for RTD2. The continuous line is the outcome of our self consistent simulation for low frequency capacitance, the dots are the measured low frequency capacitance and the squares are measured emitter-collector ( $C_{ec}$ ) capacitance. In the inset, the simulated and measured static curves in the forward bias are shown. The same layer parameters are used for capacitance simulation as used for the static simulations (table - 2.2). The plot clearly shows the deviation of low frequency capacitance from the emitter-collector capacitance. We have studied this deviation further and more elaborately.

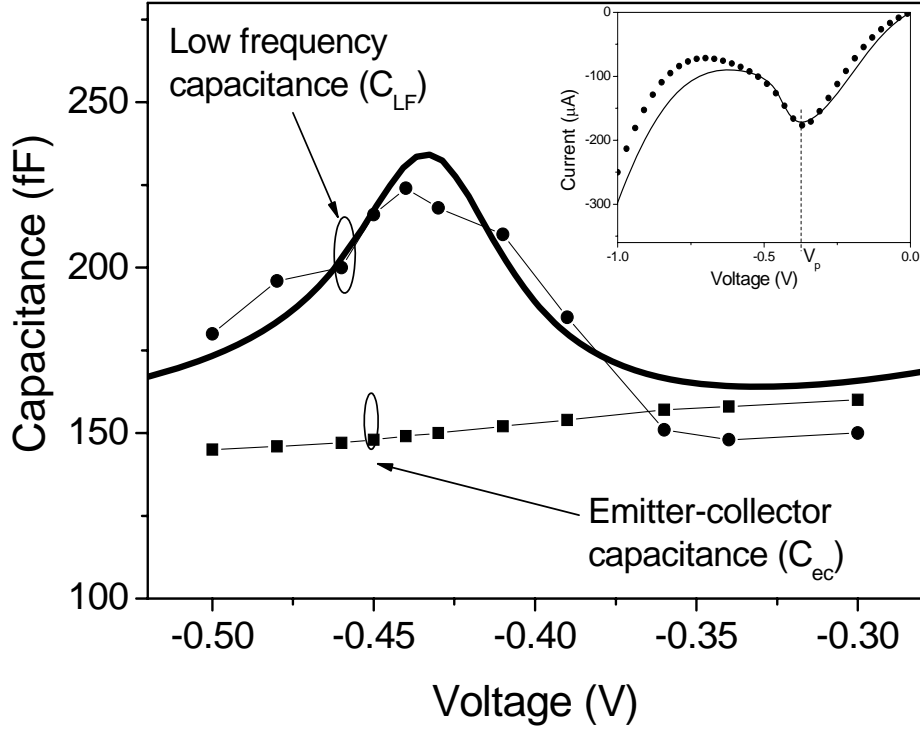


Figure 3.5: The measured and simulated low frequency RTD capacitance at the reverse biasing conditions. The continuous line is the outcome of our self consistent simulation for low frequency capacitance, the dots are the measured low frequency capacitance and the squares are measured emitter-collector ( $C_{ec}$ ) capacitance. Inset shows the measured and simulated I-V characteristics in the reverse biasing conditions. Layer parameters used for the capacitance simulations are same as used for static simulations (table - 2.2).

The effective RTD capacitance at low frequencies isn't same but deviates from the simple emitter-collector geometrical capacitance. From the plot of the RTD capacitances (Fig. 3.4 and 3.5), it is difficult to conclude if RTD capacitance is in reality different than the emitter-collector capacitance particularly in the PDC region since they are pretty close. To examine RTD capacitance more accurately and carefully, we have studied the deviation of low frequency RTD capacitance from the geometrical emitter-collector capacitance ( $C_{ec}$ ). Eventually this deviation of RTD capacitance is bias dependent. The experimental emitter-collector capacitance ( $C_{ec}$ ) is evaluated from the RTD susceptance at very high frequencies (i.e. when  $\omega\tau_{resp} \gg 1$ ). The extraction procedure of RTD admittances are explained in details in chapter 4. Since  $\omega\tau_{resp} \approx 10$  at 12 GHz of frequency so  $C_{ec}$  is

calculated at 12 GHz. The low frequency capacitance is calculated from the measured susceptance when the condition  $\omega\tau_{resp} \ll 1$  is satisfied i.e. at frequencies lower than 1-2 GHz. The measured and simulated deviations of low frequency capacitances for forward as well as reverse biasing conditions are represented in the following figures.

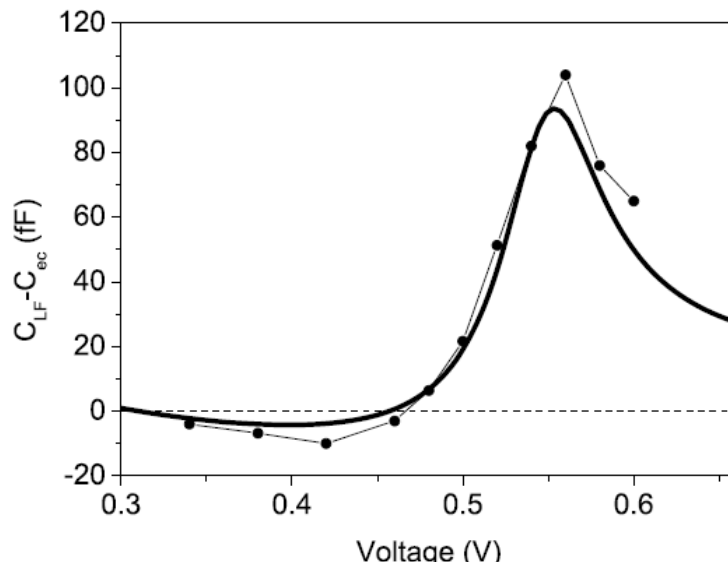


Figure 3.6: The measured and simulated deviation of low frequency RTD capacitance from emitter-collector geometrical capacitance at different voltages in the forward biasing conditions. The deviation of capacitance is defined as  $C_{LF} - C_{ec}$ . The simulation is done with the same RTD parameters (table - 2.2) as used for the I-V characteristic simulations (Fig. 2.16). The continuous line is the outcome of the self-consistent simulation and dots are the measurements.

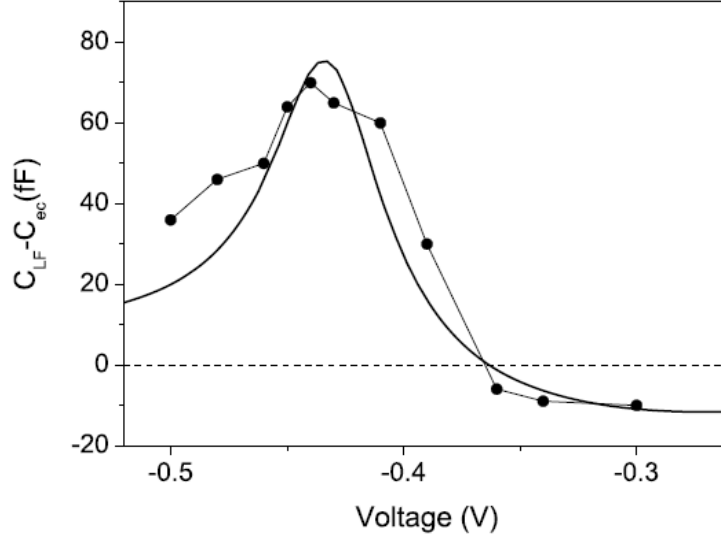


Figure 3.7: The measured and simulated deviation of low frequency RTD capacitance from emitter-collector geometrical capacitance at different voltages in the reverse biasing conditions. The deviation of capacitance is defined as  $C_{LF} - C_{ec}$ . The simulation is done with the same RTD parameters (table - 2.2) as used for the I-V characteristic simulations (Fig. 2.16). The continuous line is the outcome of the self-consistent simulation and dots are the measurements.

The deviation of low frequency capacitance from the emitter-collector capacitance for RTD2 are simulated (same simulation parameters are used as used for static simulation and the low frequency capacitance simulation, table 2.16) using the developed analytical RTD equivalent circuit [1, 44]. The match in between the measurements and the simulations are pretty good in both the PDC and the NDC regions as well for both biasing conditions (Fig. 3.6 and Fig. 3.7). The fact that the simulation of the bias dependent  $C_{LF} - C_{ec}$  match well with the experimental values, proves that the developed simple AC model for RTD [1] is correct.

### 3.3 RTD equivalent circuit with backflow of electrons

The dynamic model of RTD [1, 44, 46] does not consider the back injection of electrons from the collector to the quantum well. Normally, the RTDs used nowadays for high frequency applications has long spacer in the collector side and the Fermi level in the



collector side stays much lower than the bottom of the 2D subband inside the QW. Since the collector side Fermi level is much lower than the 2D subband bottom inside the QW so the QW electrons find empty states in the collector to tunnel. Hence the approximation is well justified for the traditional type of RTDs, but in some cases when the depletion layer on the collector side of RTD is small and the Fermi-level in the collector is close to or higher than the bottom of the 2D-subband in the quantum well, the back injection needs to be taken into account in order to represent RTD admittance correctly. Such type of RTDs are studied in references [46, 51]. Some dynamic models [36, 43] do consider the back injection of electrons but the equivalent circuit derived is complicated. We have developed an analytical model for such type of RTDs. The form of the equivalent circuit (Fig. 3.2) is same as it was for the traditional RTDs [1, 44] although consideration of backflow changes significantly the circuit parameters (inductance and conductances in Fig. 3.2).

### 3.3.1 Basic equations

We considered the RTD in the sequential tunnelling approximation [7]. The current is normal to the barriers and assumed to be homogeneous in the cross-section of the RTD. The conduction band diagram of RTD is shown in figure 3.8, Now we consider the steady state equations require to analyse the dynamic behaviors of RTD,

$$U_w - U_e = U_{w0} + \frac{e^2}{C} N_{2D} + \frac{d}{l+d} (E_{fc} - E_{fe}), \quad (3.17)$$

$$U_w - U_c = U_{w0} + \frac{e^2}{C} N_{2D} - \frac{l}{l+d} (E_{fc} - E_{fe}), \quad (3.18)$$

Here  $U_e$  and  $U_c$  are the conduction band bottoms in the emitter and collector.  $U_w$  and  $U_{w0}$  are the positions of the 2D subband bottom in the QW at applied bias and at zero applied bias, respectively.  $d$  is the emitter-well length which contains the effective Thomas-Fermi screening length, emitter barrier and half width of the QW (Fig. 3.8).  $E_{fe}$ ,  $E_{fw}$  and  $E_{fc}$  are the Fermi level positions in the emitter, well and collector respectively.  $N_{2D}$  is the electron concentration in the QW.  $C = \epsilon(l+d)/ld$  is the capacitance of the QW per unit area. The equations (3.17) and (3.18) are derived from Poisson's relation considering the

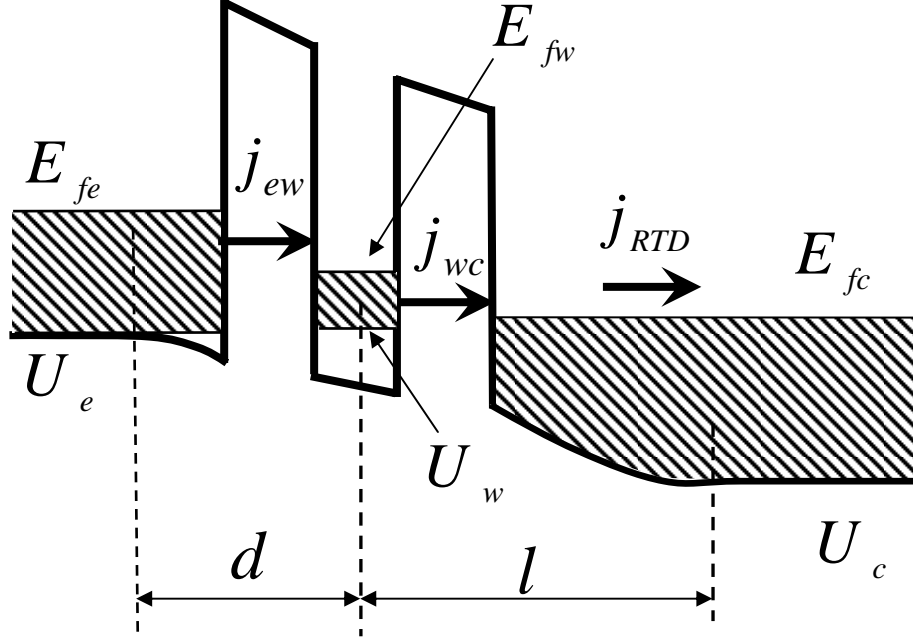


Figure 3.8: Conduction band energy diagram of RTD with heavily doped collector.

Coulomb interaction of QW electrons with emitter and collector. If Coulomb interaction isn't present then the emitter-well potential drop,  $U_w - U_e$  (in equation 3.17) would be just the leverage factor of total potential drop ( $E_{fc} - E_{fe}$ ). Because of the Coulomb interaction of QW electrons with emitter and collector bottom of 2D subband ( $U_w$ ) goes upwards by  $e^2 N_{2D}/C$ . Well-collector voltage drop ( $U_w - U_c$ ) is calculated in the same way in equation (3.18) by considering Coulomb interaction effect.

$$J_{ew} = -e \left\{ \left[ \rho_{2D} kT \ln \left( 1 + \exp \frac{E_{fe} - U_w}{kT} \right) - \rho_{2D} kT \ln \left( 1 + \exp \frac{E_{fw} - E_{fc}}{kT} \right) \right] \nu_e \right\}, \quad (3.19)$$

$$J_{wc} = -e \left\{ \left[ \rho_{2D} kT \ln \left( 1 + \exp \frac{E_{fw} - U_w}{kT} \right) - \rho_{2D} kT \ln \left( 1 + \exp \frac{E_{fc} - U_w}{kT} \right) \right] \nu_c \right\}, \quad (3.20)$$

Here  $J_{ew}$  and  $J_{wc}$  are the emitter-well and well-collector current densities. The 2 dimensional density of states in the QW is denoted by  $\rho_{2D} = m^*/\pi\hbar^2$  where  $m^*$  is the electron

effective mass in the QW.  $\nu_e$  and  $\nu_c$  are emitter and collector barrier tunnel transparencies, respectively (Fig. 3.8). The equations for emitter-well ( $J_{ew}$ ) and well-collector ( $J_{wc}$ ) current densities are valid at any finite temperature. The first term in the right hand side of equation (3.19) defines the emitter to well forward current component if the QW is completely empty. The second term in the same expression defines the well to emitter backward current component if the emitter is completely empty. So the net current density across the emitter barrier (i.e.  $J_{ew}$ ) is the resultant of the emitter to well forward and the well to emitter backward current densities. Similarly the equation 3.20 is derived for the well to collector current density ( $J_{wc}$ ). Although the relations (3.19) and (3.20) are valid for any temperature but they are difficult to handle. So to simplify them further we consider the zero temperature approximation ( $kT \rightarrow 0$ ).

$$J_{ew} = -e \{ \rho_{2D}(E_{fe} - U_w) - \rho_{2D}(E_{fw} - U_w) \} \nu_e, \quad (3.21)$$

$$J_{wc} = -e \{ \rho_{2D}(E_{fw} - U_w) - \rho_{2D}(E_{fc} - U_w) \} \nu_c, \quad (3.22)$$

The concentration of 2DEG in the quantum well ( $N_{2D}$ ) considering the Fermi-Dirac distribution is,

$$N_{2D} = \rho_{2D} \int_{U_w}^{\infty} \frac{dE}{1 + \exp(1 + \frac{E - E_{fw}}{kT})}, \quad (3.23)$$

The integration over E is considered here with lower limit of  $U_w$  (i.e. bottom of the subband) and upper limit of  $\infty$ . Performing the above integration and considering the zero temperature approximation ( $kT \rightarrow 0$ ) relation 3.23 simplifies to

$$N_{2D} = \rho_{2D} (E_{fw} - U_w), \quad (3.24)$$

So the emitter-well (relation 3.21) and well-collector (relation 3.22) current relations can be further simplified to,

$$J_{ew} = -e \{ \rho_{2D}(E_{fe} - U_w) - N_{2D} \} \nu_e, \quad (3.25)$$

$$J_{wc} = -e \{ N_{2D} - \rho_{2D}(E_{fc} - U_w) \} \nu_c, \quad (3.26)$$

Finally we are ready with the simplified expressions for the emitter-well ( $J_{ew}$ ) and well-collector current densities ( $J_{wc}$ ). Using the continuity equations for the charges at the QW,

$$-e \frac{\partial}{\partial t} N_{2D} = J_{ew} - J_{wc}, \quad (3.27)$$

By applying a small variation (represented as  $\delta$ ) to the set of equations (3.17, 3.18, 3.25, 3.26 and 3.27) in the vicinity of a stationary state we achieved the following linearized relations,

$$\delta U_{we} = \frac{e^2}{C} \delta N_{2D} + \frac{d}{l+d} \delta E_{fc}, \quad (3.28)$$

$$\delta U_{wc} = \frac{e^2}{C} \delta N_{2D} - \frac{l}{l+d} \delta E_{fc}, \quad (3.29)$$

$$\delta J_{ew} = -e \delta [\{\rho_{2D}(E_{fe} - U_w) - N_{2D}\} \nu_e], \quad (3.30)$$

$$\delta J_{wc} = -e \delta [\{N_{2D} - \rho_{2D}(E_{fc} - U_w)\} \nu_c], \quad (3.31)$$

$$-e \frac{\partial}{\partial t} \delta N_{2D} = \delta J_{ew} - \delta J_{wc}, \quad (3.32)$$

Here  $\delta U_{we} = \delta(U_w - U_e)$  and  $\delta U_{wc} = \delta(U_w - U_c)$ . In addition to these equations, we consider another relation for the total AC current density of RTD which includes both the real and displacement parts,

$$\delta J_{RTD} = \frac{d}{l+d} \delta J_{ew} + \frac{l}{l+d} \delta J_{wc} + \frac{C_{ec}}{e} \frac{\partial}{\partial t} (\delta E_{fc}), \quad (3.33)$$

The equation (3.33) is a consequence of Schockley-Ramo [48, 49] theorem.

### 3.3.2 RTD response time

The expression for the linear response of RTD on the bias variation of  $\delta E_{fc}(t)$  is derived from the relations (3.28, 3.29, 3.30, 3.31 and 3.32),

$$\left[ \frac{\partial}{\partial t} + \frac{1}{\tau_{resp}} \right] \delta N_{2D}(t) = k \delta E_{fc}(t) \quad (3.34)$$

where

$$\kappa = \rho_{2D} \left[ -\frac{d}{l+d} \left( \nu_e - (E_{fe} - E_{fw}) \nu'_e(V_{we}) \right) + \frac{l}{l+d} \left( \nu_c - (E_{fc} - E_{fw}) \nu'_c(V_{cw}) \right) \right] \quad (3.35)$$

and

$$\frac{1}{\tau_{resp}} = \nu_c + \nu_e + \beta \left[ \left( \nu_c - (E_{fc} - E_{fw}) \nu'_c(V_{cw}) \right) + \left( \nu_e - (E_{fe} - E_{fw}) \nu'_e(V_{ew}) \right) \right] \quad (3.36)$$

Here  $\nu'_e(V_{ew})$  defines the variation of  $\nu_e$  with respect to the variation of  $V_{ew}$ . Similarly  $\nu'_c(V_{cw})$  is the variation of  $\nu_c$  with respect to the variation of  $V_{cw}$ .

The response time  $\tau_{resp}$  signifies the tunnel relaxation time of the charge fluctuations in the QW. Response time is the time that the quantum well charge takes to adopt with the sudden change in the applied bias. The first two terms in relation (3.36) define relaxation due to the electron tunneling to collector and emitter, respectively, and they give rise to electron dwell time in the QW:

$$\frac{1}{\tau_d} = \nu_c + \nu_e \quad (3.37)$$

If  $N_{2D}$  changes then position of the quantum well bottom ( $U_w$ ) changes due to the Coulomb interaction of the electron's in the QW with emitter and collector. Hence number of free states available for tunneling into the QW and collector also changes which gives rise to an additional contribution in  $J_{ew}$  and  $J_{wc}$  (third and fifth term in relation 3.36). In addition to these components current changes due to the variation of  $\nu_e(V_{we})$  and  $\nu_c(V_{cw})$  (the fourth and sixth term in relation 3.36) which in turn contributes to the RTD response time. If one neglects the Coulomb effects (the limit of  $C \rightarrow \infty$  i.e.  $\beta \rightarrow 0$ ), then  $\tau_{resp} = \tau_d$ . In the previous model [1, 44], the collector was completely free for the QW electrons to tunnel and backflow of electrons across the well-collector barrier was not taken into account (the approximation is valid well for the typical RTDs). If the case of electron backflow from collector to QW is taken into consideration, then the analytical expression for the

intrinsic response time of RTD is different than that derived before [1]. The derived RTD response time (relation 3.36) here contains an additional term as  $(\nu_c - (E_{fc} - U_w)\nu'_c)$  when compared with the old model [1]. This extra term was missing before [1] because the well-collector back current was not considered there. In the present case, this extra term is originating due to the fact that the electron backflow from collector to well is also participating in the process of charge fluctuations in the QW, so affecting the RTD response time ( $\tau_{resp}$ ). In the PDC region  $\tau_{resp}$  can be further simplified to (see appendix),

$$\frac{1}{\tau_{resp}} = \nu_c + \nu_e + \beta(\nu_e + \nu_c) \quad (3.38)$$

Already it has been shown theoretically [1, 47] and experimentally [37, 38, 69] that the RTD response time in the PDC region is less than the resonant state lifetime ( $\tau_d$ ). In case of RTDs considering backflow of electrons from collector to well the response time ( $\tau_{resp}$ ) in the PDC region contains an extra term ( $\beta\nu_c$  in relation 3.38) when compared with RTD where the electron backflow from collector to QW is not significant. This fact makes the RTD response time even lesser than before [1, 47] for the PDC region. So the RTDs with backflow of electron from collector to well should respond faster than the traditional ones when operated in the PDC region of I-V characteristic.

### 3.3.3 RTD Admittances

From the relations (3.28, 3.29, 3.30, 3.31, 3.32 and 3.33), the expression for the differential conductance of RTD is derived as:

$$G_{RTD}(\omega) = \frac{e\delta J_{RTD}}{\delta E_{fc}} = i\omega C_{ec} + G_{RTD}^{\infty} + \frac{G_{RTD}^0 - G_{RTD}^{\infty}}{1 + i\omega\tau_{resp}} \quad (3.39)$$

where  $C_{ec} = \epsilon/(l + d)$  is the emitter-collector capacitance,  $G_{RTD}^0$  and  $G_{RTD}^{\infty}$  are the real part of the admittance at static condition and at high frequencies, respectively. The basic forms of  $G_{RTD}^{\infty}$  and  $G_{RTD}^0$  are:

$$G_{RTD}^{\infty} = e^2\rho_{2D} \left( \frac{d}{d+l} \right)^2 \left[ \nu_e - (E_{fe} - E_{fw})\nu'_e(V_{we}) \right] +$$

$$e^2 \rho_{2D} \left( \frac{l}{d+l} \right)^2 \left[ \nu_c - (E_{fc} - E_{fw}) \nu'_c (V_{cw}) \right] \quad (3.40)$$

and

$$\begin{aligned} G_{RTD}^0 &= \beta C \left[ \left( \frac{d}{d+l} \right)^2 (\nu_e - (E_{fe} - E_{fw}) \nu'_e) + \left( \frac{l}{d+l} \right)^2 (\nu_c - (E_{fc} - E_{fw}) \nu'_c) \right] \\ &+ e^2 \kappa \tau_{resp} \left[ \frac{d}{d+l} \nu_e - \frac{l}{d+l} \nu_c \right] + e^2 \kappa \beta \tau_{resp} \\ &\times \left[ \left( \frac{d}{d+l} \right) (\nu_e - (E_{fe} - E_{fw}) \nu'_e) - \left( \frac{l}{d+l} \right) (\nu_c - (E_{fc} - E_{fw}) \nu'_c) \right] \quad (3.41) \end{aligned}$$

After doing some more algebra,  $G_{RTD}^\infty$  and  $G_{RTD}^0$  can be further represented in a more compact form,

$$G_{RTD}^\infty = \frac{d}{l+d} C_{wc} \left( \frac{1}{\tau_{resp}} - \frac{1}{\tau_d} \right) + e^2 \rho_{2D} \frac{l-d}{l+d} [\nu_c + (E_{fw} - E_{fc}) \nu'_c] \quad (3.42)$$

and

$$\begin{aligned} G_{RTD}^0 &= C_{wc} \nu_c \left( 1 - \frac{\tau_{resp}}{\tau_d} \right) + e^2 \rho_{2D} (\nu_c + (E_{fw} - E_{fc}) \nu'_c) \\ &\times \left[ 1 - \frac{d}{l+d} \frac{\tau_{resp}}{\tau_d} - \nu_c \tau_{resp} - \beta \tau_{resp} (\nu_c + (E_{fw} - E_{fc}) \nu'_c) \right] \quad (3.43) \end{aligned}$$

where  $C_{wc} = \epsilon/l$  is the well-collector capacitance. So the admittance for RTDs when backflow of electron from collector to the QW is inevitable is derived (relation 3.39). The form of the equivalent circuit (relation 3.39 and Fig. 3.2) remains same although the circuit elements in terms of the RTD parameters differ when backflow of electrons from collector to quantum well is taken into account.

### 3.3.4 Effective RTD capacitance at low frequencies

In the case of low frequencies ( $\omega \tau_{resp} \ll 1$ ) the RTD admittance can be simplified and represented by a simple RC circuit (Fig. 3.9),

$$G_{RTD} = i\omega C_{LF} + G_{RTD}^0 \quad (3.44)$$

where

$$C_{LF} = C_{ec} + \tau_{resp} (G_{RTD}^\infty - G_{RTD}^0) \quad (3.45)$$

The expression for the effective RTD low frequency capacitance  $C_{LF}$  is;

$$\begin{aligned} C_{LF} &= C_{ec} + e^2 k \tau_{resp}^2 \left( -\nu_e \frac{d}{d+l} + \nu_c \frac{l}{d+l} \right) + e^2 k \tau_{resp}^2 \beta \\ &\times \left( -\frac{d}{l+d} (\nu_e - (E_{fe} - E_{fw}) \nu_e') + \frac{l}{d+l} (\nu_c - (E_{fc} - E_{fw}) \nu_c') \right) \end{aligned} \quad (3.46)$$

The analytical relations for the effective RTD capacitance ( $C_{LF}$ ) at low frequencies is valid well for both the PDC and NDC region of I-V characteristic. In the PDC region, the approximations  $\nu_e \gg (E_{fe} - E_{fw}) \nu_e'(V_{we})$  and  $\nu_c \gg (E_{fw} - E_{fc}) \nu_c'(V_{cw})$  are valid reasonably (from appendix). So low frequency effective capacitance of RTD in the PDC region can be simplified to,

$$C_{LF} = C_{ec} + C \frac{\beta}{\beta+1} \left( \frac{\frac{d}{l+d} - \frac{l}{l+d} \gamma}{1+\gamma} \right)^2 \quad (3.47)$$

The effective RTD capacitance at low frequencies is represented analytically in terms of the device geometrical parameters and the tunnel transparencies (relation 3.47) and expression clearly shows RTD capacitance at the low frequency limit is not same but deviates from emitter-collector geometrical capacitance ( $C_{ec}$ ).

The ratio of low frequency capacitance ( $C_{LF}$ ) with the emitter collector capacitance ( $C_{ec}$ ) is,

$$\frac{C_{LF}}{C_{ec}} = 1 + \frac{d}{l} \frac{\beta}{\beta+1} \left( \frac{1 - \frac{l}{d} \gamma}{1+\gamma} \right)^2 \quad (3.48)$$

Now let us see the different limiting cases for the ratio of  $C_{LF}/C_{ec}$ . When  $\gamma \rightarrow 0$ , the ratio takes the following form,



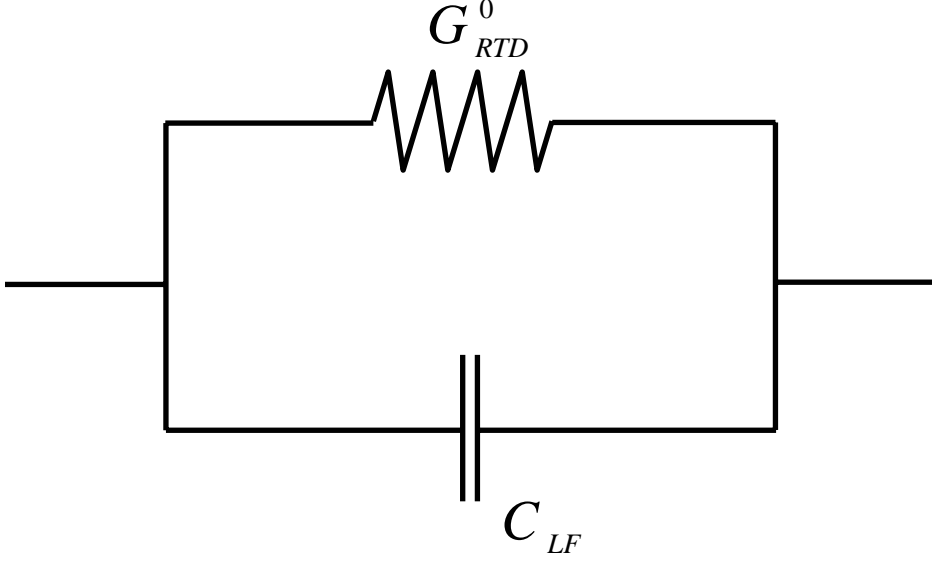


Figure 3.9: RTD equivalent circuit in the low frequency limit ( $\omega\tau_{resp} \ll 1$ ).  $G_{RTD}^0$  is the RTD static conductance and  $\tilde{C}$  is the low frequency RTD capacitance represented by the expression 3.46.

$$\frac{C_{LF}}{C_{ec}} = 1 + \frac{\beta}{\beta + 1} \frac{d}{l} \quad (3.49)$$

In the case of  $\gamma \rightarrow d/l$ ,

$$\frac{C_{LF}}{C_{ec}} = 1 \quad (3.50)$$

So the low frequency RTD capacitance is simple emitter-collector capacitance. At the other extreme limit, i.e. when  $\gamma \rightarrow \infty$ ,

$$\frac{C_{LF}}{C_{ec}} = 1 + \frac{\beta}{\beta + 1} \frac{l}{d} \quad (3.51)$$

In figure 3.10, low frequency capacitance in the PDC region for the RTD studied by Auer et. al. RTD with the ratio of collector to emitter barrier transparency is plotted. Consequence of relation 3.47 is for the RTDs where backflow of electron is inevitable, the low

frequency capacitance in the PDC region is always more than the emitter-collector geometrical capacitance (figure 3.10). The low frequency capacitance of these type of RTDs behave differently than the traditional RTDs where backflow of electron from collector to QW is not significant (for example the RTD studied by Mattia et. al. [36]).

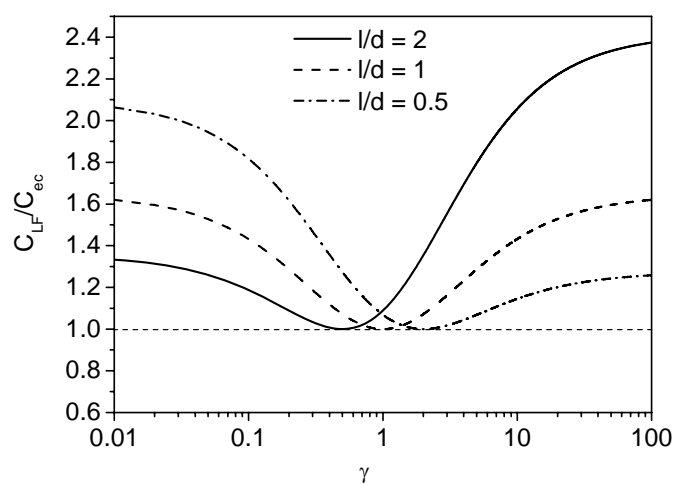


Figure 3.10: Plot of effective capacitance at low frequencies ( $C_{LF}$ ) vs.  $\gamma$  in the PDC region for the RTD studied by Auer et. al. [51] when ratio of the emitter-well ( $d$ ) to well-collector ( $l$ ) lengths are different.

### 3.4 Conclusions

This chapter deals with the dynamic behaviors of RTD. The special property of RTD low frequency capacitance lies in its deviation from emitter-collector geometrical capacitance ( $C_{ec}$ ), particularly in the PDC region it can be more or less than  $C_{ec}$ . A simple analytical model for RTD capacitance in terms of RTD parameters for the PDC region, is derived depending on the RTD dynamic model obtained earlier [1, 44]. For our RTDs, the deviation of low frequency capacitance from the emitter-collector capacitance is studied by experiment and simulation. The analytical model [1, 44] for the dynamic behaviours of RTD is extended further by considering the backflow of electrons from collector to QW. For some RTDs [46, 51], the backflow of electron is significant. Although the form of the equivalent circuit remains the same with the previous model [1] where backflow was not taken into considerations, but the different circuit elements in terms of the RTD parameters are changed. We have shown analytically that in the PDC region of I-V curve, the intrinsic response time of RTDs where electron backflow is taking place, is shorter compared to the RTDs without the collector to QW electron backflow. Another consequence of the extended model is, the low frequency deviation of RTD capacitance from the emitter-collector capacitance in the PDC region is always positive because of the electron backflow from collector to QW, whereas for the RTDs where backflow isn't significant the same deviation can have positive or negative values depending upon the diode parameters.

# Chapter 4

## Simulation and measurement of RTD admittances

In this chapter we present the small signal measurements on our RTDs. Our studied diodes have several parasitic elements around the mesa. The procedure to eliminate the parasitics are explained. The simulation and measurement of the RTD conductances (real part of admittance) and susceptances (imaginary part of admittances) at different applied bias are presented. We have shown a way to extract the intrinsic response time of RTD from microwave measurements of the devices and later self-consistent simulations are compared with the measurements.

### 4.1 Device design

One of the aims of this work is to experimentally demonstrate that resonant tunneling exists in RTD beyond the resonant state lifetime limit. Theoretically it has been shown that resonant state lifetime doesn't impose limitation on the high frequency operation of RTD [1, 44] and there were indirect experimental data also which support the same fact [36]. The general perception is beyond resonant state lifetime limit resonant tunneling current can not exist [2, 3]. The direct consequence of this fact is NDC should vanish when applied bias variation with time is faster than the resonant state lifetime (i.e.  $\omega\tau_d \gg 1$ ). So the direct proof of resonant tunnelling beyond resonant state lifetime limit would be the existance of NDC at frequencies beyond the resonant state lifetime limit. It has been shown theoretically [1, 44] that specially designed (i.e. RTDs with heavily doped collector)

RTD should demonstrate NDC beyond the resonant state lifetime limit.

Our aim in this work is to characterize RTDs in the PDC as well in the NDC region of the current-voltage characteristics. For that purpose we need to consider several factors while designing RTD for our AC measurements. The RTDs we designed for our experiments should have the following properties: good peak to valley current ratio (PVCR) and stable NDC. But devices with high PVCR are hard to stabilize in the NDC region. So while designing the diodes we had to make trade off among these above mentioned factors. We need to design devices with stable NDC region (which is must for characterization in the NDC region), so we sacrificed PVCR and we opted for thick barrier RTDs. By introducing a sub-well inside the quantum well, we could increase the separation between the quantised (resonant state) levels to improve the PVCR. Hence our designed RTD consists of thick barriers and composite quantum well along with the heavily doped collector. The purpose of doping collector heavily is to observe NDC at frequencies beyond the resonant state lifetime limit [1, 44].

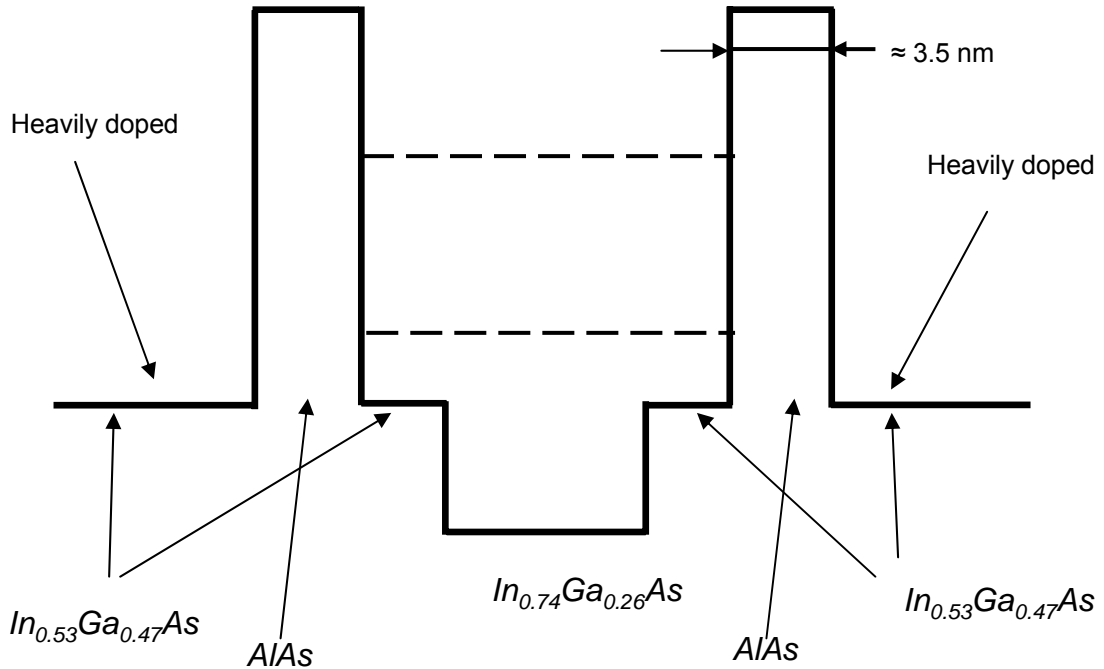


Figure 4.1: Conduction band diagram for the nominally designed RTD (table 4.1).

We have chosen *InGaAs/AlAs* material system on the InP substrate for our diodes. Conduction band offset of *AlAs/In<sub>0.53</sub>Ga<sub>0.47</sub>As* is around 1.1 eV with the *AlAs* as barrier. We have chosen high barrier height so that we can prevent the thermionic current over the barrier as well as the non-resonant tunnelling current. Further we have introduced a subwell inside the QW (Fig. 4.1) in order to increase the separation in between the 2D subbands in the QW so that the higher resonant current turn on could be delayed with respect to the applied bias. Such adjustments of the materials helped us to reduce the current components besides the resonant current through the first QW subband hence increases the PVCR and static RTD conductance. The conduction band profile for the nominally designed RTD layer parameters are shown in figure (4.1). Table (4.1) represents the relevant data for the layers.

Composition	In	Ga	Al	As	Thickness	Function	n-doping, cm <sup>-3</sup>
InGaAs	53	47		100	50	contact layer	$1.0 \times 10^{18}$
InGaAs	53	47		100	1.5	spacer	
AlAs			100	100	3.5	barrier	
InGaAs	53	47		100	1.2	well, smoothing	
InGaAs	74	26		100	2.5	well	
InGaAs	53	47		100	1.2	well, smoothing	
AlAs			100	100	3.5	barrier	
InGaAs	53	47		100	1.5	spacer	
InGaAs	53	47		100	50	contact layer	$1.0 \times 10^{18}$

Table 4.1: Nominal parameters for our designed RTD. Conduction band profile is shown in Fig. (4.1).

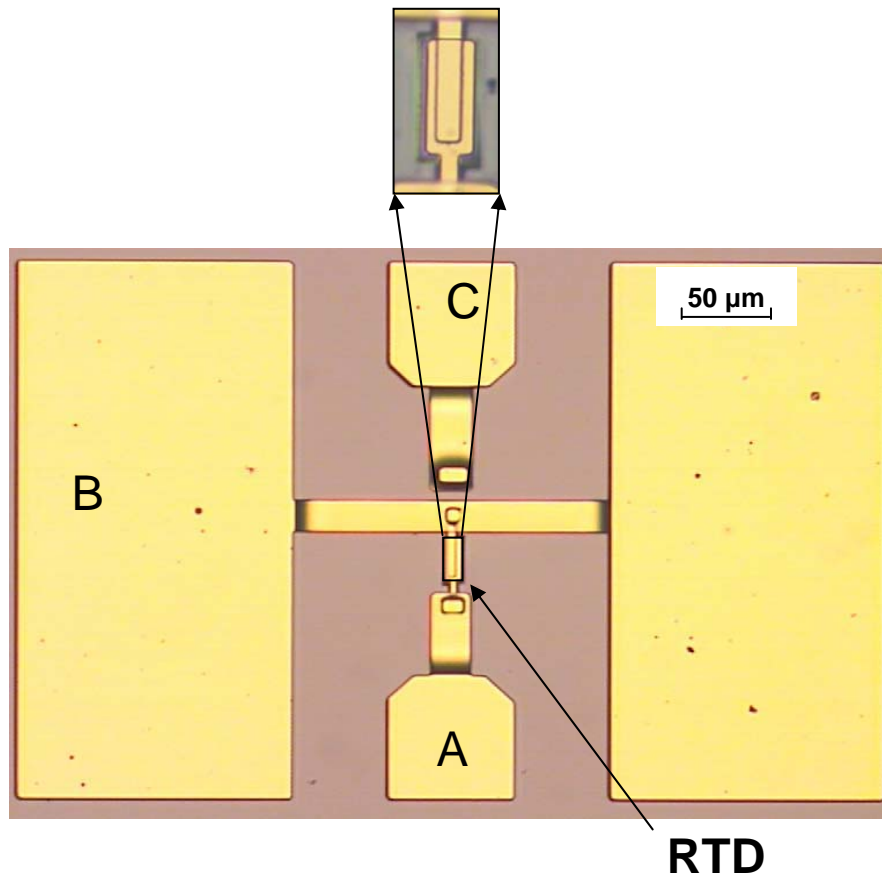


Figure 4.2: Microscope picture of the fabricated diode. The diode is connected to the contact pads using air-bridges and several metal lines. The measurement pads (A) and (B) are the contacts for the two terminals of the RTD. The pad (C) is not connected to the diode. The mask used for the fabrication of RTDs is designed for HBT (Heterostructure Barrier Transistor) processing where pad (C) is made to make the collector contact. For the fabrication of our diodes the process is stopped after RTD fabrication. So contact pad (C) is isolated from the diode. The magnified picture of fabricated RTD is shown in the inset.

### 4.1.1 Impact of spacers on NDC of RTD

Generally RTDs used for high frequency applications have long spacer layer [20, 22, 36, 50] in the collector side. Objective of using long spacer layer is to reduce the capacitave contribution hence the RC time constant of the diodes. For example the RTDs studied by Mattia et. al. [36, 50] have long spacer (100 nm) in the collector side which makes the conductance to roll-off from negative values at low frequencies to positive values at high frequencies. But it has been shown theoretically [1, 44] that the RTDs with well-collector length of the same order of emitter-well length ( $d \approx l$ ) should demonstrate NDC even at frequencies much much greater than the inverse of resonant state lifetime. The idea is against the general perception [3, 2]. The figure (4.3) shows how the frequency response of RTD conductance depends on the well-collector length or in other words on the doping of the collector. We are considering here RTD1 (Fig. 2.16 and table 2.2) but the spacer in the collector side is changing from 2 nm upto 100 nm. For long spacers the effective well-collector lengths ( $l$ ) are much greater than the effective emitter-well ( $d$ ) lengths hence making the high frequency conductance positive. When the well-collector lengths ( $l$ ) is of the same order of emitter-well lengths ( $d$ ), the high frequency conductance of RTD becomes negative.



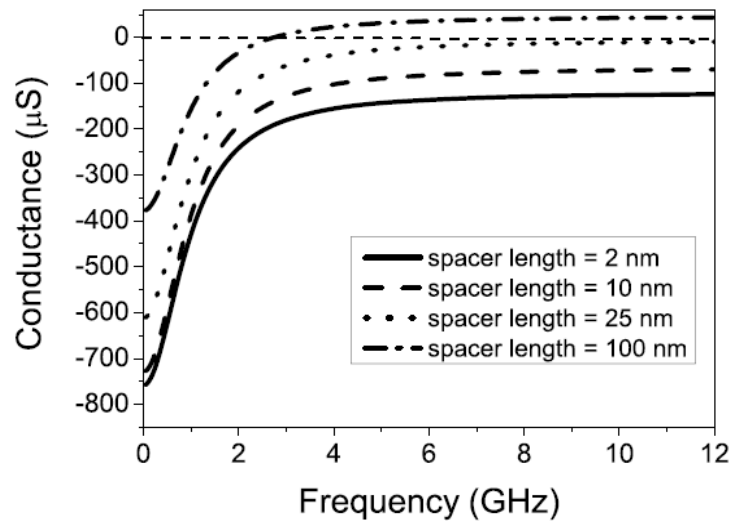


Figure 4.3: Frequency response of real part of RTD admittance (conductance) when the device is biased at NDC for different spacer lengths. The diode simulated here is similar to RTD1 studied in this work (Fig. 2.16 and table 2.2) except the spacers used in the collector side differs in lengths. In the inset to the figure corresponding spacer lengths are shown.

## 4.2 Scattering parameter measurements

In order to find the the AC response of the diodes, we performed reflection measurements. Well accepted on wafer measurement technique is used for our AC measurement which is suitable for microwave frequencies (particularly for frequencies less than 40 GHz). Fig. (4.4) shows a schematic diagram for the small signal AC measurement setup. The AC signal and the DC bias are delivered to the diodes by the coplanar microwave probe. The reflection coefficients ( $S_{11}$ ) are measured using an Anritsu 37397C vector network analyzer at frequencies ranging from 40 MHz upto 12 GHz. After knowing the parameter  $S_{11}$  a transformation is applied to derive the admittances.

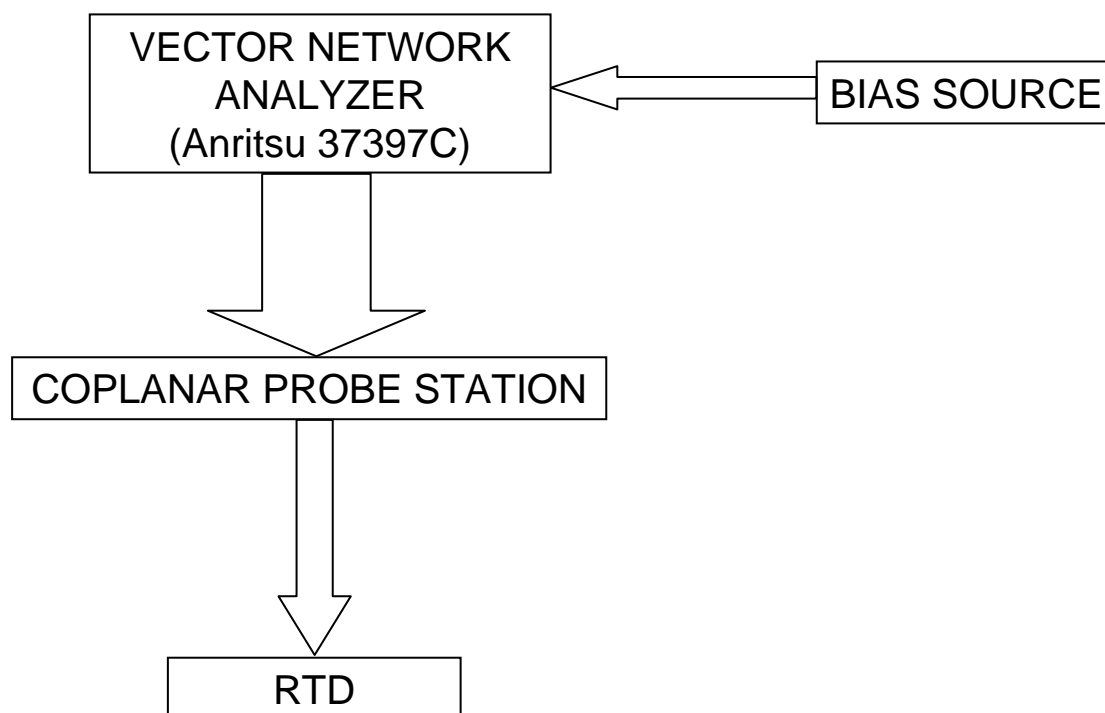


Figure 4.4: Schematic of the experimental set up used to measure the reflection co-efficient using network analyzer. The bias source provides the dc bias for the diode through the network analyzer.

The network analyzer is calibrated using the standard open-short-load calibration technique using a commercially available substrate. The incident power used for measurement is -30 dBm which corresponds to a peak to peak AC voltage swing at the device less than 25 mV. The DC bias is delivered using a standard digital power source.

AC measurements are done at several bias points in the PDC and NDC region. The complete range of frequencies are scanned by as much as 1600 points to get as much as possible accurate trend of the measurements. A plot of the measured admittances including the parasitics at 0.42 V forward bias is shown in Fig.(4.5).

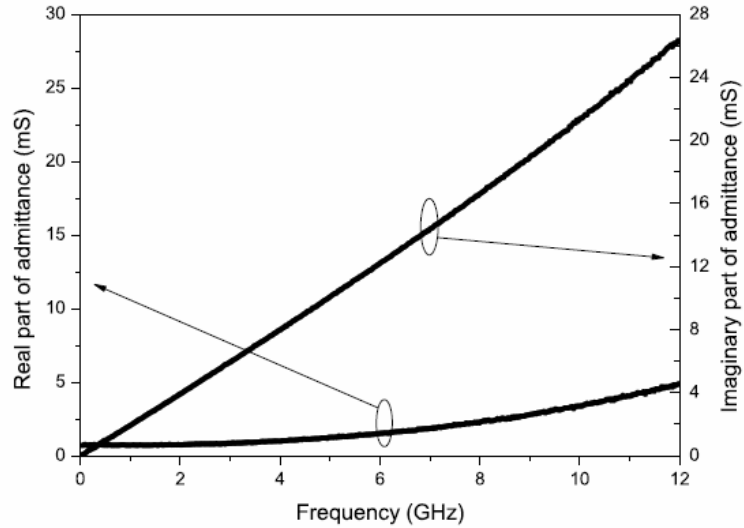


Figure 4.5: The measured raw admittance of a  $3 \times 15 \mu m^2$  diode at 0.42 V forward bias. The measured diode belong to the batch of RTD2. The admittance response shown here includes the contribution from the parasitics too. Elimination of the parasitics is required in order to extract the true (intrinsic) RTD admittances.

### 4.3 Evaluation of parasitics

The admittances thus measured include the contribution from the parasitics. In order to extract the intrinsic ('pure') RTD admittance from the measurement, we must identify the electrical parasitics. The fabricated devices have planar structures where the emitter and collector are connected to the measurement pad via the air bridges. Because of the

presence of the metallisations around the device, they lead to parasitic inductances and capacitances.

The whole combination of RTD together with the parasitics can be represented by the small signal equivalent circuit as described in Fig.(4.6). The similar method was adopted by Auer et. al. [51] although they considered the parasitics ( $L_s$  and  $C_{ex}$ ) to be frequency dependent in order to match their experimental AC data with theory. In their work the RTD part was represented by the simple RC circuit. In case of the simple RC circuit the delay in RTD current with voltage is ignored. That could be a possible reason that the parasitics there [51] are frequency dependent. In this section we will describe the measurements and simulations of the parasitics around our RTDs.

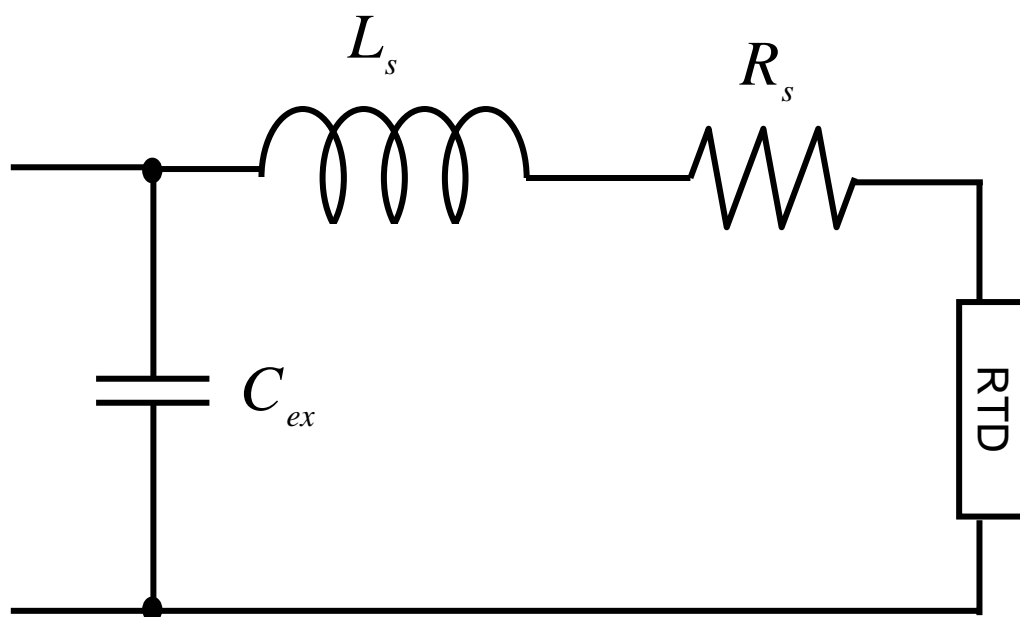


Figure 4.6: The lumped equivalent circuit model for RTD together with the frequency independent parasitics surrounding the diodes.

### 4.3.1 Measurement of parasitics

To evaluate the parasitic capacitance and inductance experimentally and as much as precisely possible, we studied some test structures called as open circuit (Fig. 4.7a) and short circuit devices (Fig. 4.7b). By short circuit device we mean all the metallisations, air bridges surrounding the device remaining same only the device is substituted by a short-cut. Similarly, in case of an open circuit device, the device is replaced by an open circuit all other metal lines remaining the same.

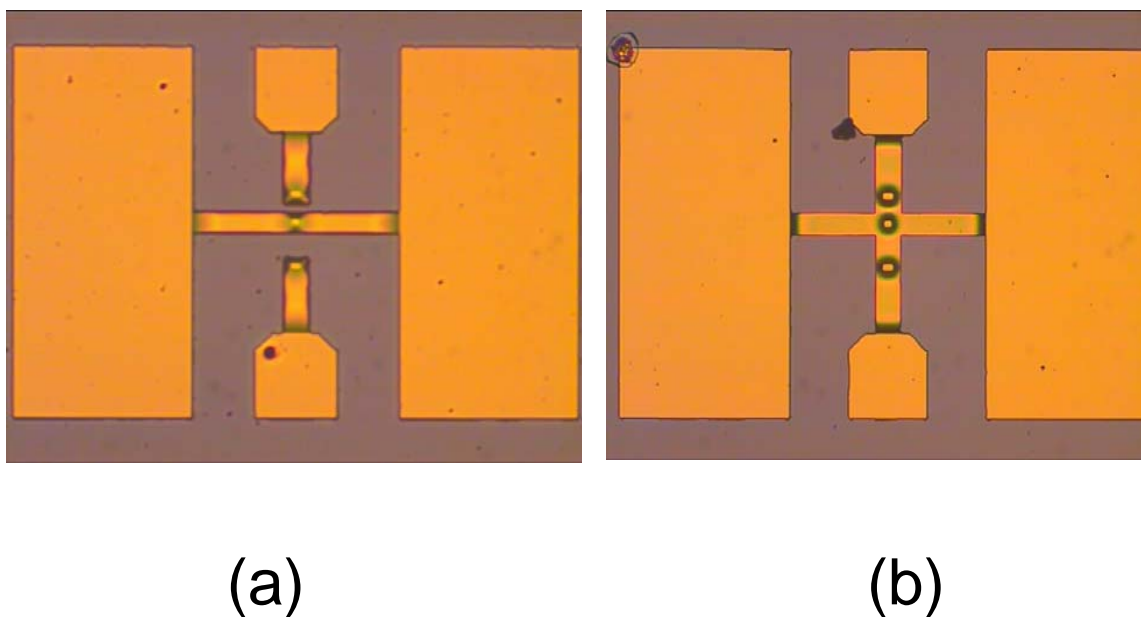


Figure 4.7: Microscope pictures of the open circuit (a) and short circuit (b) devices. These structures are used for the evaluation of the parasitic capacitance ( $C_{ex}$ ) and inductance ( $L_s$ ).

Measurement of the open circuit device gives information about the parasitic stray capacitance (Fig. 4.8a). The measured susceptance of the open structure shows a clear capacitive behavior (Fig. 4.9). Knowing the value of the stray capacitance ( $C_{ex}$ ) along

with the measurement on the short structures (equivalent circuit is shown in Fig. 4.8b) reveals the value of the parasitic inductance ( $L_s$ ). Careful observation shows that the open structure (Fig. 4.8a) and the short structure (Fig. 4.8b) are not exactly same. They differ because of the extra metal line which connects the emitter and the collector contacts. This extra metal line may change the parasitic capacitance ( $C_{ex}$ ) to some extent. Our measured value of  $C_{ex}$  is  $\approx 18$  fF. If  $C_{ex}$  is changed by 2 fF (say), then the extracted value of  $L_s$  differs by less than 1 pH. So, the extra metal line in the short structure should not affect the measured value of parasitic inductance ( $L_s$ ). Moreover, while extracting the RTD admittances at different bias points, we used the same value of the parasitics (i.e.  $C_{ex}$  and  $L_s$ ).

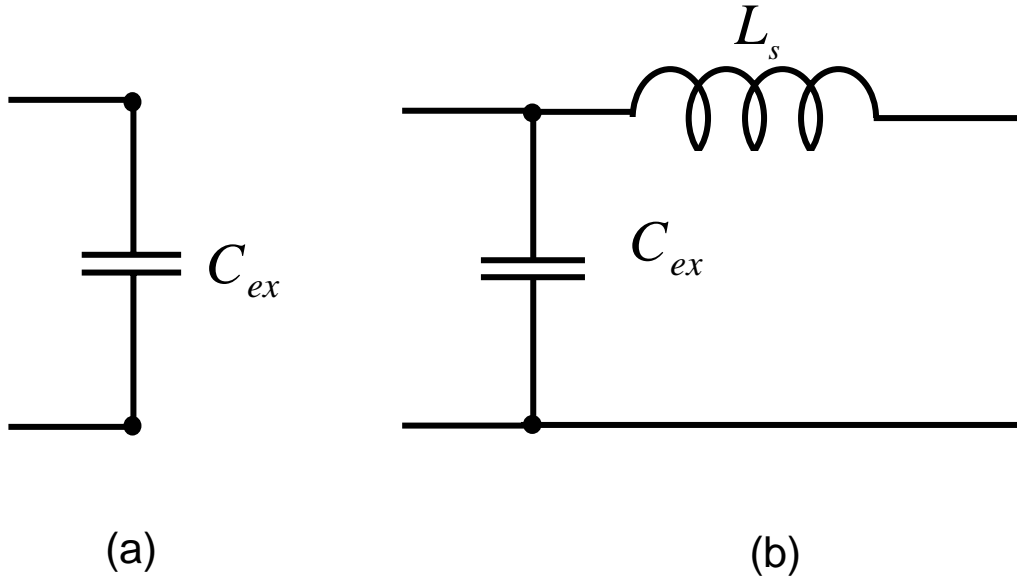


Figure 4.8: Equivalent circuits in case of open (a) and short (b) test devices employed to measure the parasitic capacitance ( $C_{ex}$ ) and inductance ( $L_s$ ).

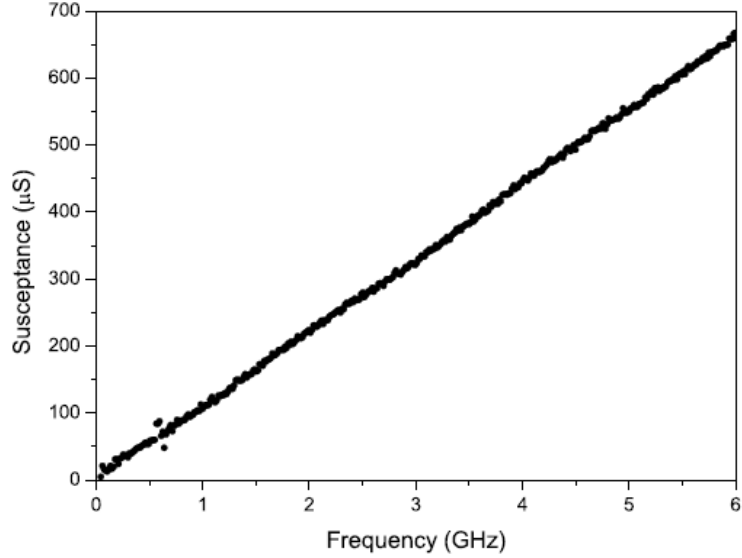


Figure 4.9: susceptance measurement on the open structures to evaluate the parasitic capacitance ( $C_{ex}$ ).

Now we are done with the parasitic capacitance and inductance. Next is the evaluation of the parasitic series resistance ( $R_s$ ). To characterize  $R_s$ , we measured the real device of dimension  $3 \times 15 \mu\text{m}^2$  (this is the same diode on which admittance measurements are done in this work) from 1 GHz upto 20 GHz of frequencies. Since the parasitics  $C_{ex}$  and  $L_s$  are already known, so we extract the admittance of the remaining combination of RTD and the series resistance (in the equivalent circuit in Fig. 4.6, the part excluding the parasitics  $C_{ex}$  and  $L_s$ ). The real and imaginary parts of the impedance show asymptotic behavior at high frequencies (Fig. 4.11) confirming the fact that RTD can be represented as an RC circuit at high frequencies. Since the internal resistance of RTD is very high so the real part of impedance converges to the series resistance at very high frequencies and imaginary part of impedance converges to high frequency capacitance of the diode (Fig. 4.11). Hence the value of impedance at high frequencies is considered as the series resistance ( $R_s$ ). The measured values of the parasitic elements are shown in table (4.2).

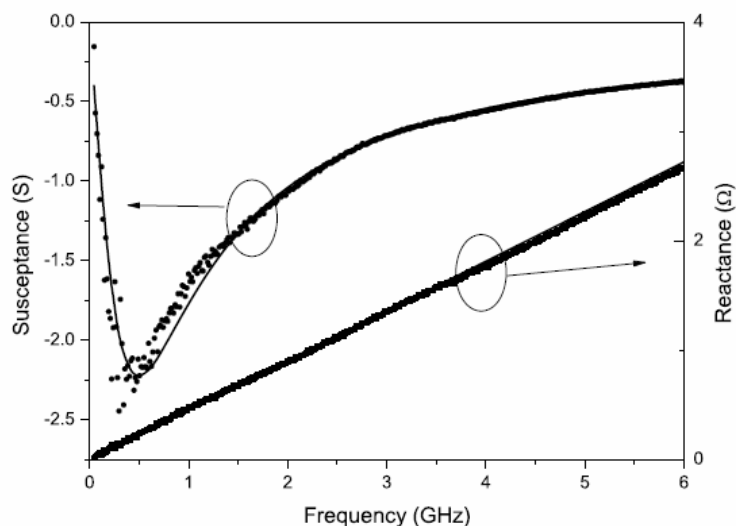


Figure 4.10: Measurement and simulation of the reactance and the susceptance of the short-cut test device. The value of the parasitic inductance is calculated as 76 pF from the reactance plot. The susceptance is simulated (continuous line) considering the lumped equivalent circuit shown in figure (4.8b). Good match of measured and simulated susceptance at low frequency confirms the extracted value of the parasitic inductance ( $L_s$ ).

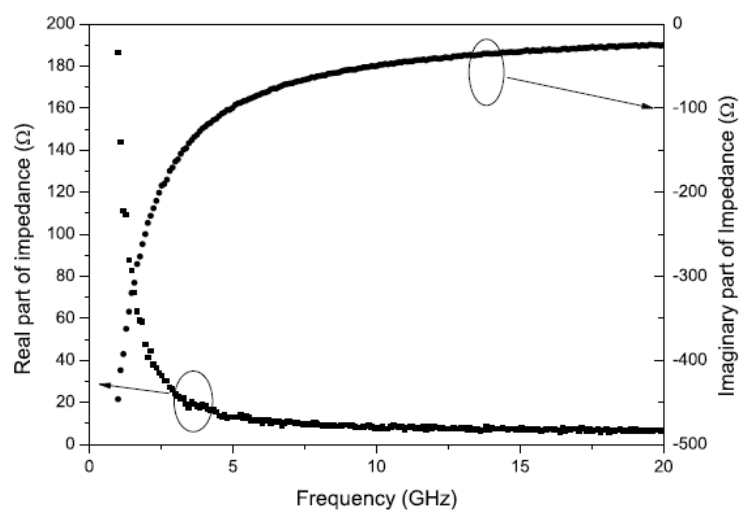


Figure 4.11: The real and imaginary part of the impedance of the combination of series resistance and the RTD under test.



parasitic components	values
capacitance ( $C_{ex}$ )	18 fF
inductance ( $L_s$ )	76 pH
series resistance ( $R_s$ )	6.75 $\Omega$

Table 4.2: The measured values of the parasitic elements around RTD.

### 4.3.2 Simulation of parasitics

So far the parasitics ( $L_s$ ,  $C_{ex}$  and  $R_s$ ) are measured using the test structures and by high frequency measurement of the real device. We have done a quantitative assessment of the parasitics too. We used CST electromagnetic simulator to calculate the values of the parasitic inductance ( $L_s$ ) and capacitance ( $C_{ex}$ ). The solver works on the finite integration technique (FIT) method. Basically, the method numerically solves the integral form of Maxwell's relations in electrodynamics in a finite calculation domain where the domain encloses the considered problem [70]. Four parts of the software are available to us, namely as, electrostatic simulator, magnetostatic simulator, low frequency simulator and static current simulator. First step is to build a model of the fabricated RTD for simulation (Fig. 4.12). Once the replica of the device is build, simulation can be started to solve for the concerned problem. Electrostatic solver is used to calculate the parasitic capacitance ( $C_{ex}$ ) and the derived value is  $\approx 16$  fF. The calculation of inductance ( $L_s$ ) is not straight forward. The software can solve magnetostatics problem with much ease. But our diodes have complicated metal lines and current flows through them which induces a magnetic field around the structure. To solve for inductance first the static current through the device is simulated. By knowing the static current, magnetostatic solver can solve for the magnetic energy ( $W_m$ ) stored inside the system.  $L_s$  is connected to the magnetic energy through the relation  $W_m = (1/2)L_s I^2$ . In the relation  $W_m = (1/2)L_s I^2$ , the magnetic energy ( $W_m$ ) along with the total current ( $I$ ) are known so the parasitic inductance ( $L_s$ ) can be calculated. The value of  $L_s$  calculated in this way comes out to be as  $\approx 36$  pH. Figure 4.13 shows the schematic of our indirect method of parasitic inductance ( $L_s$ ) calculation. The in such a way simulated value of  $L_s$  doesn't match with the measurement ( $L_s \approx 76$  pH). The metal lines made to connect RTD with the contact pads are quite complicated and the thickness of the metallizations are not known accurately. In addition

to that the metallisation thickness is usually non-uniform at different parts of the real device and the metallization consists of different metals with different thicknesses (nominal values are 30 nm Ti/30 nm Pt/360 nm Au). All these geometrical factors can influence the parasitic inductance. So we attribute these uncertain factors for the discrepancy in between the measured and simulated (with the help of CST EM studio) values of the parasitic inductance ( $L_s$ ). Since the way of our measurement of  $L_s$  is direct, so we prefer to rely on our measured values.

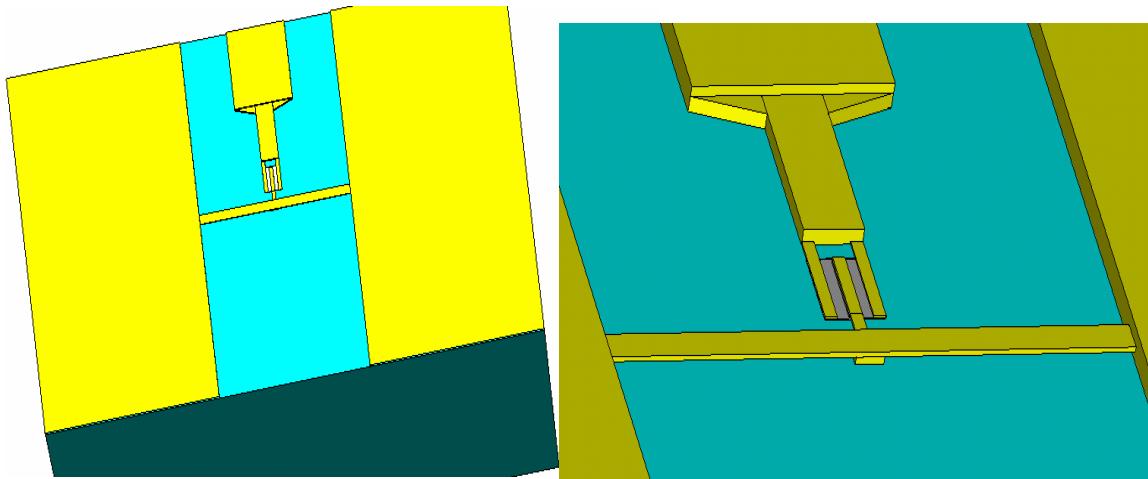


Figure 4.12: Model of the fabricated  $3 \times 15 \mu m^2$  RTD in electro-magnetic studio (EMS). This model is further used for the calculation of parasitics ( $L_s$  and  $C_{ex}$ ).

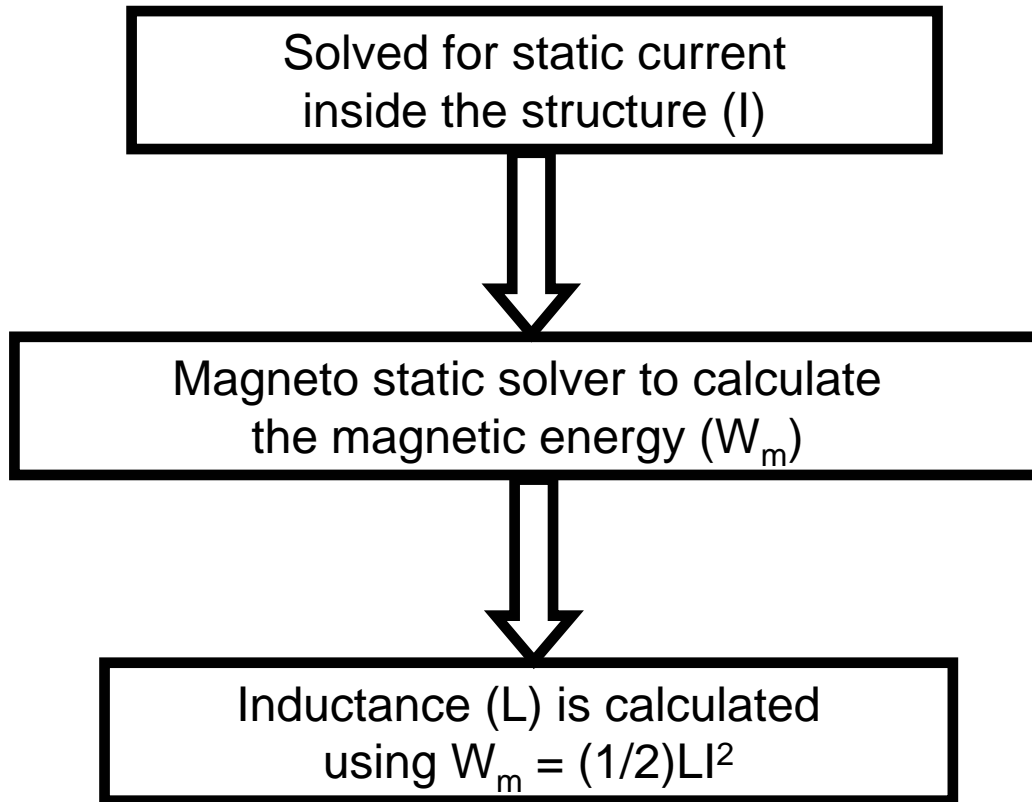


Figure 4.13: The scheme for the parasitic inductance ( $L_s$ ) calculation. Direct measurement of the parasitic inductance isn't possible so we opted for an indirect way.

The series resistance consists of three parts namely: bulk resistance, contact resistance and resistance due to the air bridges. We have done a systematic analysis of all the components of the series resistance. Although the dimension of the air bridges are very small but the contribution from them isn't significant (in total  $\approx 0.2 \Omega$ ).

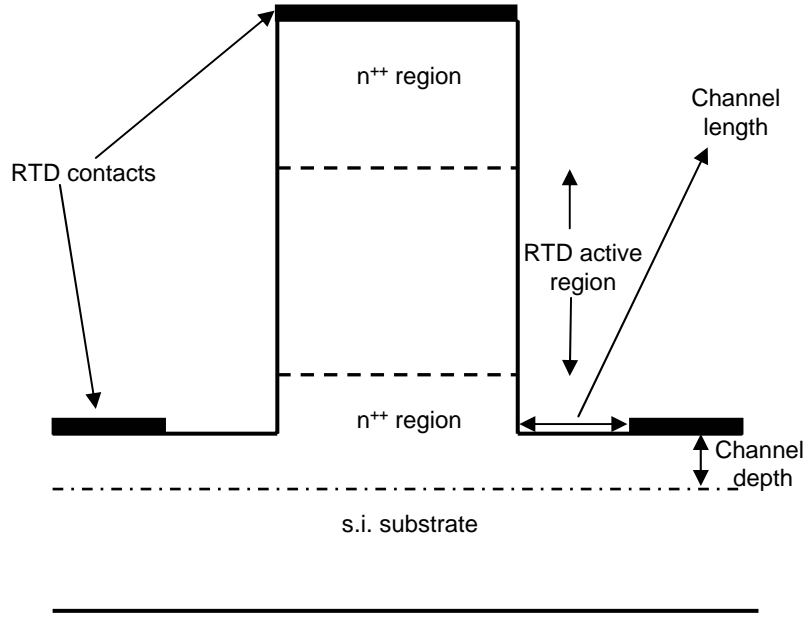


Figure 4.14: The side view of the RTD mesa. The metal contacts and the undepleted channel gives rise to contact resistance and the resistance due to bulk, respectively.

Considering a contact resistivity of  $4 \times 10^{-7} \Omega \text{cm}^2$  [51], the calculated value of contact resistance for  $3 \times 15 \mu\text{m}^2$  contact area of our structure is  $\approx 2 \Omega$ . The resistance due to the bulk semiconductor is contributed mostly from the undepleted channel in between the RTD mesa and the bottom contacts (Fig. 4.14). Considering electron mobility as  $2000 \text{ cm}^2 \text{V}^{-1} \text{S}^{-1}$  at  $1 \times 10^{19} \text{ cm}^{-3}$  doping density, a channel width of  $15 \mu\text{m}$ , channel length of  $2.5 \mu\text{m}$  and channel depth of  $0.1 \mu\text{m}$ , the resistance due to the bulk semiconductor is calculated as  $\approx 3 \Omega$ . So in total the series resistance comes out to be around  $5.2 \Omega$ . The theoretical calculation of  $R_s$  is pretty close to our experimentally obtained value but doesn't match exactly. The exact geometry of the fabricated structure (contact area, channel depth in the bulk, exact doping density etc.) isn't known accurately because of the inherent uncertainties of fabrication technology. The geometry of the fabricated

diodes differ from each other even if they are processed at the same time. So we attribute these uncertainties for the small difference in values of the simulation and measurement of series resistance ( $R_s$ ).

## 4.4 Derivation of RTD admittances

In this part we will discuss the measurement of RTD admittances. Since we have already characterized the parasitics, so the intrinsic admittances can be extracted. The RTD admittance has two parts, real part of admittance is called as conductance and the imaginary part is as susceptance.

RTD susceptance is almost linear (Fig. 4.15). It is because of the dominance of the emitter-collector depletion capacitance ( $C_{ec}$ ). So to examine susceptance more clearly we subtracted off the susceptance due to the emitter-collector ( $C_{ec}$ ) capacitance from the total susceptance ( $B_T$ ) and it is called as excess susceptance ( $B_x$ ).

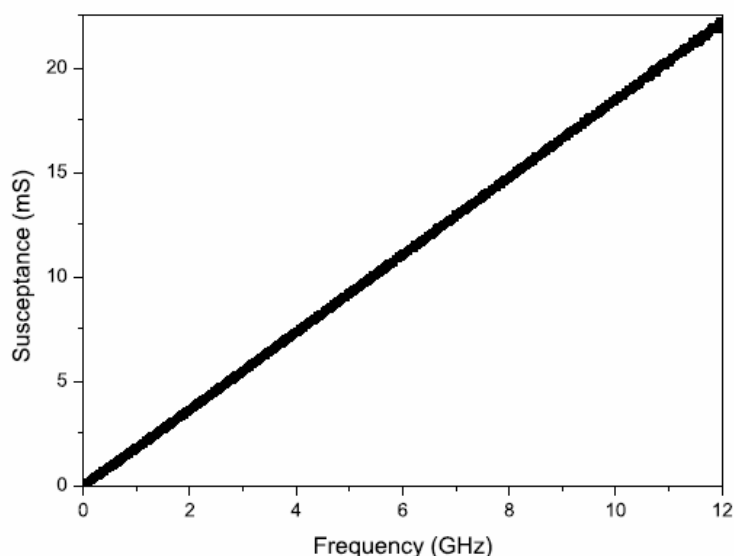


Figure 4.15: Intrinsic susceptance of RTD at 0.38 forward bias. The susceptance appears here linear in frequency although careful observation would show the deviation from linearity at low frequencies.

The emitter-collector ( $C_{ec}$ ) capacitance is calculated by averaging from 10 GHz to 12 GHz of frequencies. So the excess susceptance ( $B_x$ ) is defined as  $B_x = B_T - \omega C_{ec}$ . This excess

susceptance has some special features in its characteristics. It has a peak in frequency response and the peak frequency corresponds to the roll-off frequency of conductance. In addition to that the peak frequency gives information about the RTD response time. The RTD response time is connected with the peak frequency via the following relation (relation 4.1) as it is shown already theoretically [1, 44].

$$\tau_{resp} = 1/(2\pi f_p) \quad (4.1)$$

where  $f_p$  is the peak frequency position of excess susceptance. Close to the high frequency (for our diodes it is 12 GHz) the excess susceptance goes to zero. The extracted excess susceptances at the same bias points as taken for the conductances are shown in the figures (4.16 - 4.23). Careful observations on the excess susceptance plots (for example in the forward biasing conditions the figures are 4.16 - 4.19) show that with the increase in bias the peak frequency of the excess susceptance shifts towards the lower frequency side. The extracted conductance at several bias points taken from forward and reverse biasing conditions and belong to PDC and NDC region are shown in the figures (Fig. 4.16 - 4.23). The conductances have the similar qualitative behaviors. The roll off in conductances at different bias points are taking place around 1.5 GHz of frequency with the fact that the roll off frequency is decreasing with the increase in bias. The low frequency conductance is decreasing as one approach close to the peak biasing voltage and it becomes negative in the NDC region. Not only that the high frequency conductance in the NDC region stays negative (plots 4.18, 4.19, 4.22 and 4.23) which is the consequence of the heavily doped collector [1, 44].

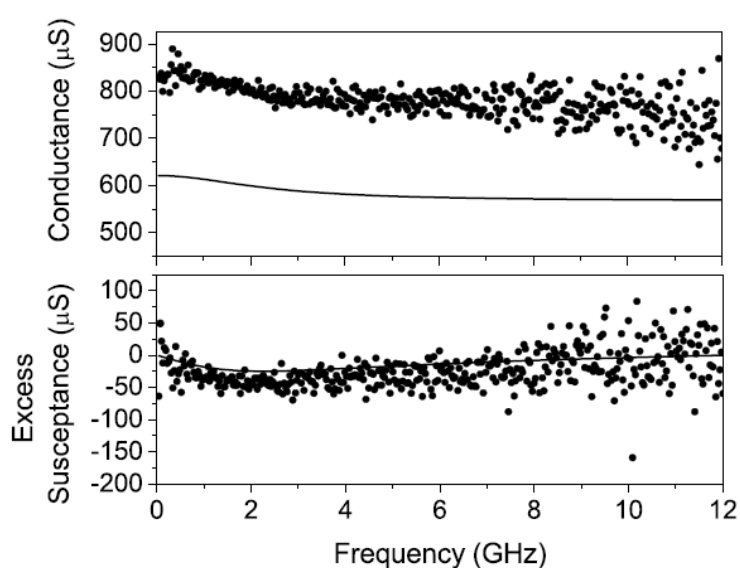


Figure 4.16: Simulated and measured RTD admittances at 0.34 V forward bias (point A in Fig. 4.24). The applied bias point is taken from PDC region of the I-V curve. The solid lines represent the simulation and the dots represent the measurement. The response of device conductances and excess susceptances with frequencies are represented in panel (a) and panel (b) respectively. The AC simulation is done with the same layer parameters as used for the static simulations (Fig. 2.16).

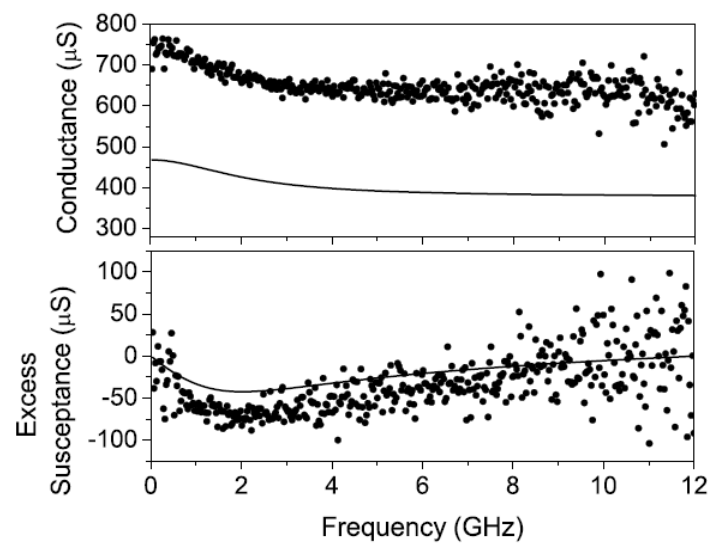


Figure 4.17: Simulated and measured RTD admittances at 0.42 V forward bias (point B in Fig. 4.24). The applied bias point is taken from PDC region of the I-V curve. The solid lines represent the simulation and the dots represent the measurement. The response of device conductances and excess susceptances with frequencies are represented in panel (a) and panel (b) respectively. The AC simulation is done with the same layer parameters as used for static simulations (Fig. 2.16).



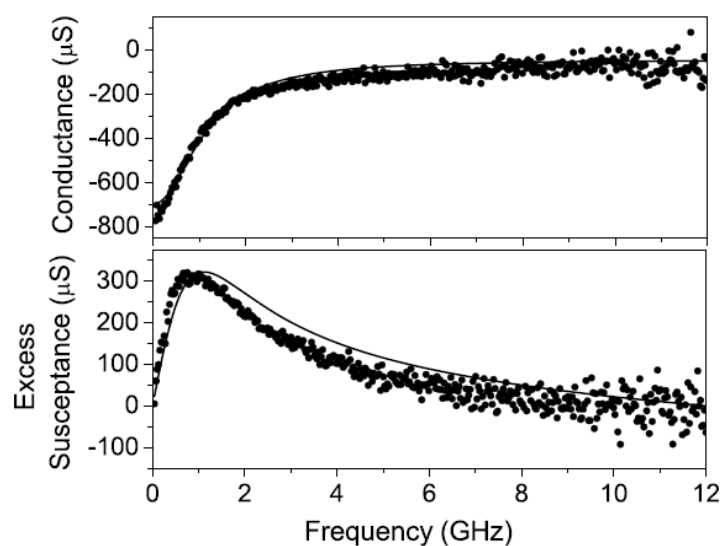


Figure 4.18: Simulated and measured RTD admittances at 0.56 V forward bias (point C in Fig. 4.24). The applied bias point is taken from NDC region of the I-V curve. The solid lines represent the simulation and the dots represent the measurement. The response of device conductances and excess susceptances with frequencies are represented in panel (a) and panel (b) respectively. The AC simulation is done with the same layer parameters as used for static simulations (Fig. 2.16).

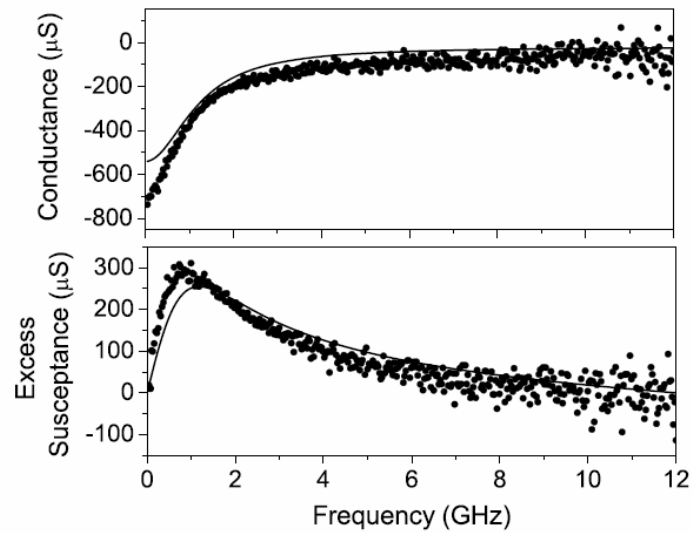


Figure 4.19: Simulated and measured RTD admittances at 0.58 V forward bias (point D in Fig. 4.24). The applied bias point is taken from NDC region of the I-V curve. The solid lines represent the simulation and the dots represent the measurement. The response of device conductances and excess susceptances with frequencies are represented in panel (a) and panel (b) respectively. The AC simulation is done with the same layer parameters as used for static simulations (Fig. 2.16).

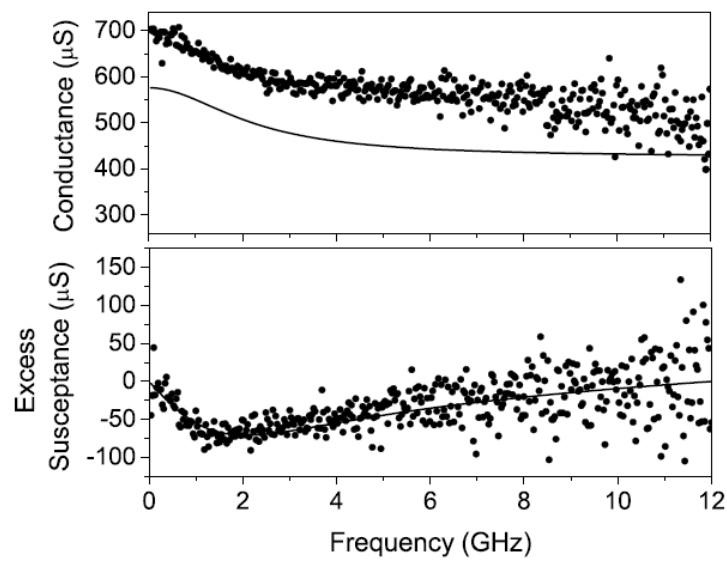


Figure 4.20: Simulated and measured RTD admittances at 0.3 V reverse bias (point E in Fig. 4.24). The applied bias point is taken from PDC region of the I-V curve. The solid lines represent the simulation and the dots represent the measurement. The response of device conductances and excess susceptances with frequencies are represented in panel (a) and panel (b) respectively. The AC simulation is done with the same layer parameters as used for static simulations (Fig. 2.16).

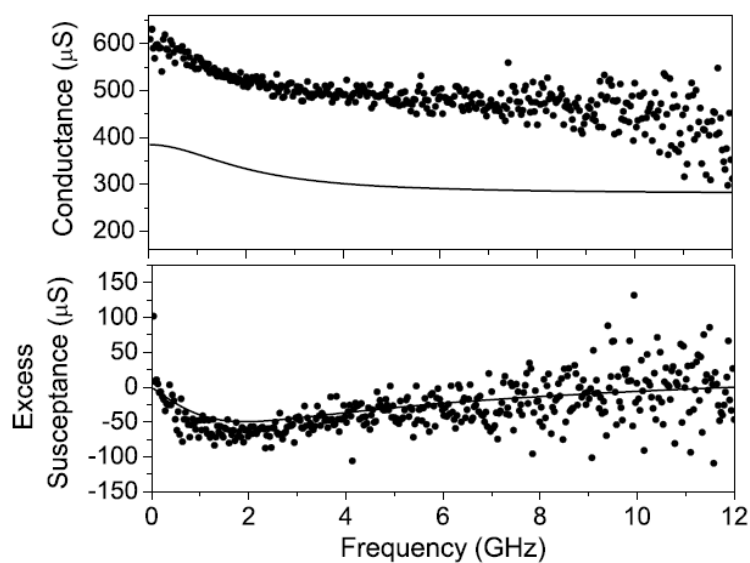


Figure 4.21: Simulated and measured RTD admittances at 0.34 V reverse bias (point F in Fig. 4.24). The applied bias point is taken from PDC region of the I-V curve. The solid lines represent the simulation and the dots represent the measurement. The response of device conductances and excess susceptances with frequencies are represented in panel (a) and panel (b) respectively. The AC simulation is done with the same layer parameters as used for static simulations (Fig. 2.16).

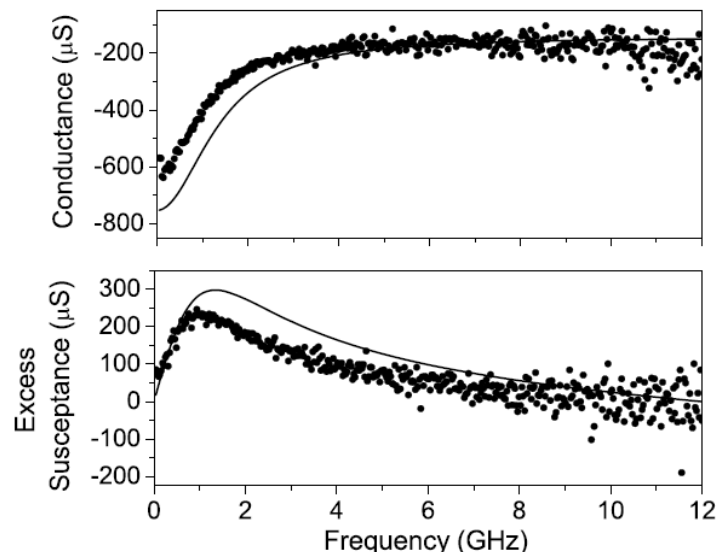


Figure 4.22: Simulated and measured RTD admittances at 0.44 V reverse bias (point G in Fig. 4.24). The applied bias point is taken from NDC region of the I-V curve. The solid lines represent the simulation and the dots represent the measurement. The response of device conductances and excess susceptances with frequencies are represented in panel (a) and panel (b) respectively. The AC simulation is done with the same layer parameters as used for static simulations (Fig. 2.16).

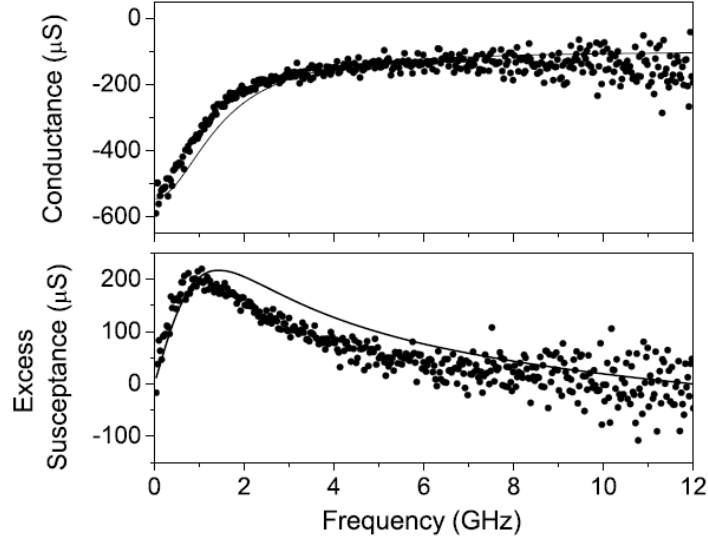


Figure 4.23: Simulated and measured RTD admittances at 0.46 V forward bias (point H in Fig. 4.24). The applied bias point is taken from NDC region of the I-V curve. The solid lines represent the simulation and the dots represent the measurement. The response of device conductances and excess susceptances with frequencies are represented in panel (a) and panel (b) respectively. The AC simulation is done with the same layer parameters as used for static simulations (Fig. 2.16).

## 4.5 Comparison of the measured and simulated AC behaviors

The admittance measurements of the diode for several bias points in the forward as well reverse biasing conditions are done. Next we simulate the RTD conductances and excess susceptances at the different bias points relying on the previously developed AC theory [1, 44]. In this chapter, we will make a comparison in between the simulated and the measured admittances. The nice agreement in between the measured and the simulated static curves (Fig. 2.16) has allowed us to use the same RTD layer parameters (table 2.2) for AC simulation. The bias points at the current-voltage characteristics where the AC measurements are compared with the self-consistent simulations are shown in figure (4.24).

The figures (4.16 - 4.23) represent the comparisons between the theoretical and the ex-

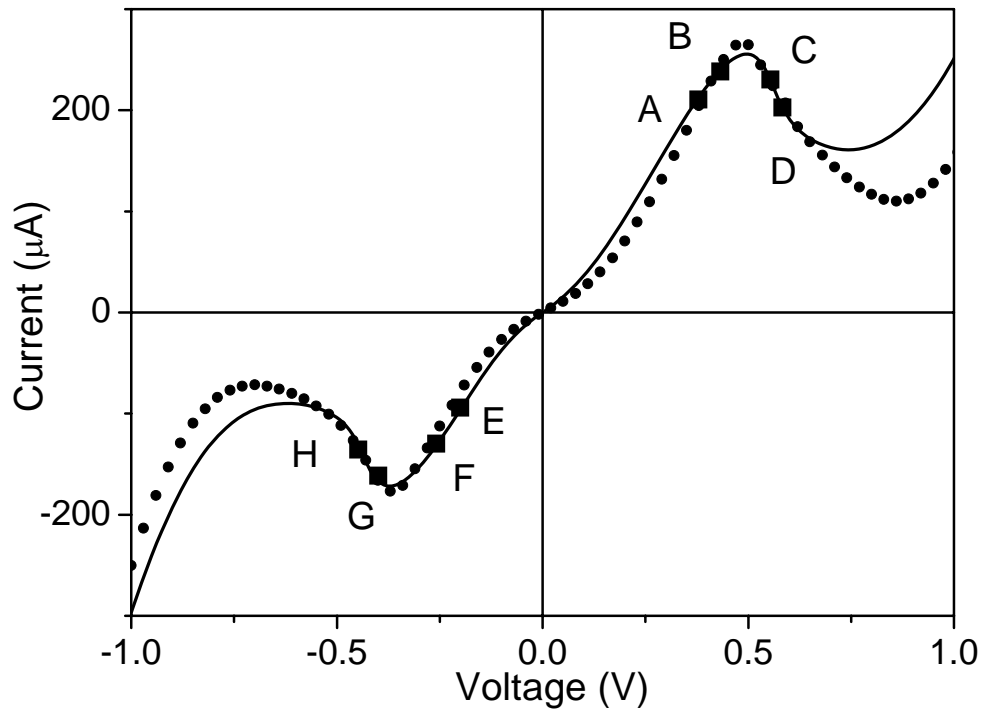


Figure 4.24: The current vs. voltage simulation and measurement of the  $45 \mu\text{m}^2$  diode from the batch of RTD2 (table 2.2). The black squares are the points where the AC measurements are compared with the simulations (figures 4.16 - 4.23). The bias points A, B, E and F are taken from the PDC region whereas the points C, D, G and H belong to the NDC region of the I-V curves.

perimental intrinsic RTD admittances for several bias points (forward and reverse both) taken from both the PDC and NDC regions. Both the simulated and the experimental AC characteristics show very good qualitative agreement for both biasing conditions (Figs. 4.16-4.23). The roll-off frequencies of the conductance, the peak frequencies of the excess susceptance, the nature of the frequency response of the conductances and the excess susceptances all these experimental data are in good agreement with the self-consistent simulation. Quantitatively the simulation has a small mismatch with the measured values of the conductances and the excess susceptances. Carefull observation of the simulated and measured G-V characteristics (Fig. 4.25) show that the static curves donot match

exactly with each other although they are very close. So we attribute the quantitative discrepancy in simulated and measured admittances to the small mismatch of the RTD static curves.

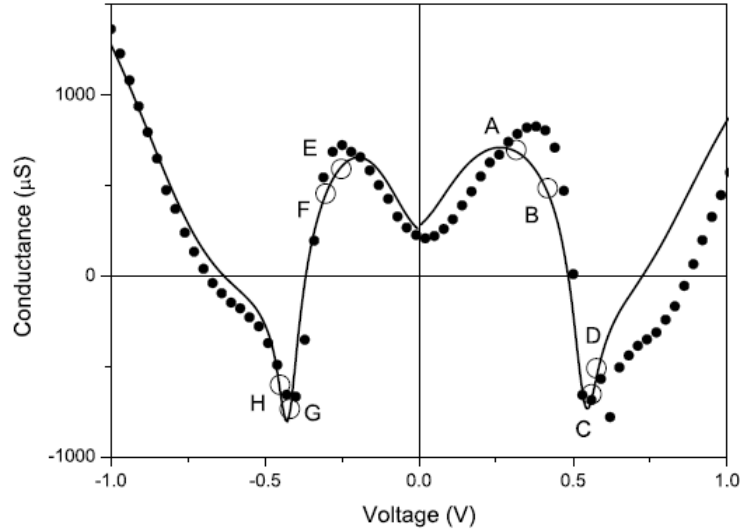


Figure 4.25: The conductance vs. voltage simulation and measurement of the  $45 \mu m^2$  diode from the batch of RTD2 (table 2.2). The simulation is done here using the same parameters as used in the figure 4.24. The circles are the bias points where the AC measurements are compared with the simulations (figures 4.16 - 4.23). The bias points A, B, E and F are taken from the PDC region where as the points C, D, G and H belong to the NDC region of the I-V curves.

The measured AC behavior can be reproduced well using the developed small signal model of RTD [1, 44]. We have used the same layer parameters for AC simulations (figures 4.16 - 4.23) as used for static curves (Fig. 2.16). Although we didn't get a perfect match in between the AC simulations and measurements but several qualitative features were reproduced well. Huge number of equivalent circuits are proposed for RTD to represent it's small signal behaviors [43, 36, 2, 42] but there exist no simple at the same time accurate one which is verified with experimental AC measurements. The theoretically developed simple small signal model [1, 44] is employed here to simulate the AC behaviors of our RTDs (we have studied extensively the batch of RTD2) and the model can reproduce the AC measurements with good enough accuracy. Another consequence of the AC measurements of our specially designed ( $d \approx l$ ) RTDs is its negative differential



conductance at high frequencies. For our diodes the frequency corresponding to the inverse of the quasi-bound-state lifetime is  $\approx 1.2 \text{ GHz}$  where as NDC has been observed till 12 GHz of frequencies for several bias points taken from the forward as well as the reverse biasing conditions (figures 4.18, 4.19, 4.22 and 4.23). So our obtained results clearly show resonant tunneling exists in RTDs at frequencies beyond the resonant state lifetime limit and electron lifetime in the resonant state doesn't impose any limitation to the operating frequency of RTD [37, 38].

## 4.6 Microwave measurement of response time

Theoretically, it has been shown that RTD admittances has a pole in its frequency response and the pole frequency corresponds to the response time of the diode [1, 44]. From the theoretically derived expression for admittance (equation 3.1) it is evident that RTD response time ( $\tau_{resp}$ ) defines a pole in  $G(\omega)$  in complex frequency plane. Precisely speaking the peak frequency of excess susceptance and roll-off frequency of the conductance corresponds to the pole frequency (3.1). Hence the pole frequency is determined from the experimental data on the excess susceptance and conductance at different bias points and transformed them into the corresponding response time. The experimental data at 0.52 V forward bias in order to find the response time are shown in Fig. (4.26) and (4.27).

The values of response times extracted from the frequency response of conductance and susceptance (such typical plot at 0.52 V bias is shown in Fig. 4.26 and 4.27) for forward and reverse biasing conditions, are plotted as the black dots in Fig. (4.28 and 4.29). The nature of the trends as well as the quantitative values of the calculated and measured response times for both biasing conditions are in good agreement with each other (Fig. 4.28 and 4.29).

## 4.7 Coulomb interaction effect on escape rates

In this section, we present our study of resonant state lifetime and intrinsic response time of RTD. The simplicity of RTD structure suggests that its intrinsic response time should be equal to the resonant state lifetime [2, 3, 46]. Previously, it has been shown theoretically [44, 47] that this approximation is not correct and quantum well charge in RTD can

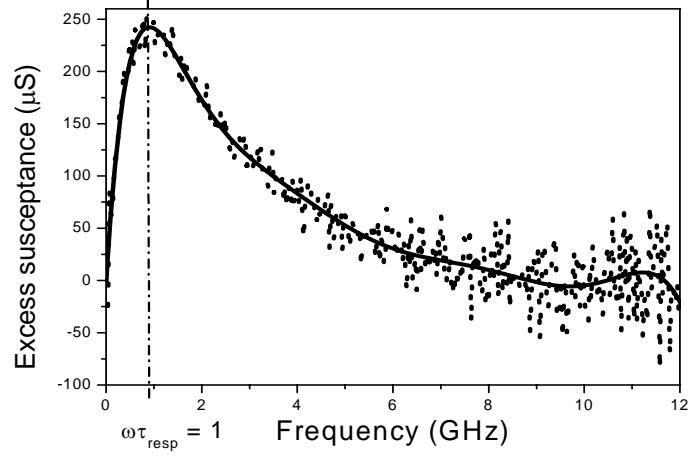


Figure 4.26: Measured excess susceptance for the diode at 0.52 V forward bias is represented here as dotted line. The solid line is a polynomial fitting of the measurement. The purpose of fitting is to find the peak position more precisely.

respond faster or slower than the electron lifetime in the resonant state because of the Coulomb interaction of QW electrons with emitter and collector. We have demonstrated experimentally that RTD response time is different than the resonant state lifetime and quantitatively they can differ by a factor of two [37]. The effect of Coulomb interaction on RTD response time is explained in the introduction (Fig. 1.4 in chapter 1).

The internal RTD parameters (table 2.2) determined on the basis of the static simulation of the I-V characteristics (Fig. 2.16) allow us to calculate  $\tau_{resp}$ ,  $\tau_d$ , and other internal tunnel time constants of RTD at varied applied bias. Along with the RTD time constants, the bias dependent Coulomb interaction effect parameter ( $\beta$ ) is also simulated. The response time is linked [47] to the electron escape rates to emitter and collector in the following way:

$$1/\tau_{resp} = (1 + \beta)/\tau_e + 1/\tau_c, \quad (4.2)$$

The expression for an effective  $\beta$  is complicated and it involves several RTD parameters including the variation of the tunnel transparencies of the barriers [47].

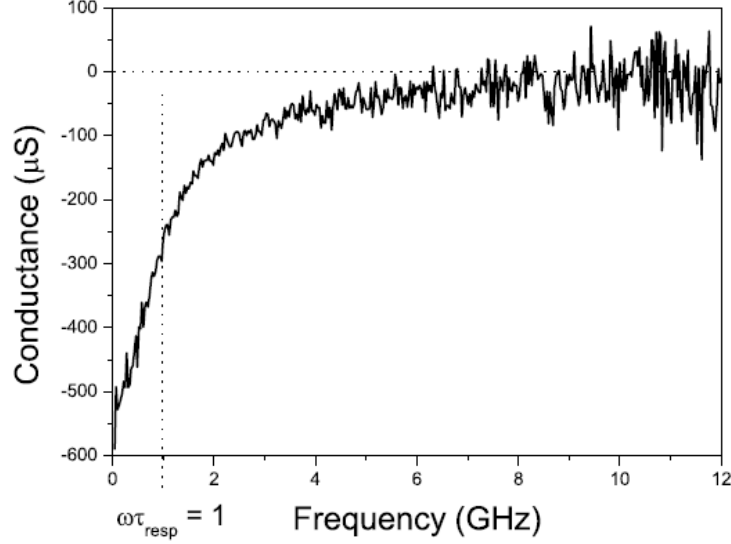


Figure 4.27: The measured RTD conductance as function of the frequency at 0.52 V forward bias. The peak in excess susceptance and the middle point in the roll-off of conductance correspond to the condition  $\omega\tau_{resp} = 1$ . The similar method is used for the other points taken from forward and reverse biasing conditions to extract the response time experimentally.

$$\beta = \frac{e^2 \rho_{2D}}{C} \left( 1 - (E_{fe} - U_w - \frac{N_{2D}}{\rho_{2D}}) \frac{\nu'_e}{\nu_e} + \frac{N_{2D}}{\rho_{2D}} \frac{\nu'_c}{\nu_e} \right), \quad (4.3)$$

In the PDC region the approximations

$$(E_{fe} - U_w - N_{2D}/\rho_{2D})\nu'_e/\nu_e \ll 1, \quad (4.4)$$

and

$$(N_{2D}/\rho_{2D})(\nu'_c/\nu_e) \ll 1, \quad (4.5)$$

are valid well (from chapter 3 and reference [1]). So in the PDC region of the I-V curve the Coulomb interaction effect parameter ( $\beta$ ) can be defined as  $\beta = e^2 \rho_{2D}/C$ . But in the NDC region  $\beta$  is much more complicated and one must consider the variation of the tunnel transparencies with the applied bias (i.e. the terms with the  $\nu'_e$  and  $\nu'_c$  in relation 4.3).

So the Coulomb interaction effect parameter ( $\beta$ ) can take positive or negative values depending upon the variation of the barrier transparencies and other RTD parameters (eqn. 4.3). The positive value of  $\beta$  makes RTD response time ( $\tau_{resp}$ ) shorter compared to the resonant state lifetime ( $\tau_d$ ) in PDC region, the negative value of  $\beta$  makes  $\tau_{resp}$  longer than  $\tau_d$  in the NDC region and at the peak voltage position (i.e. at  $V_p$ )  $\beta \rightarrow 0$  makes  $\tau_{resp} = \tau_d$  (eqn. 4.2). The calculated values of the Coulomb interaction effect parameter ( $\beta$ ) is shown for our RTDs in the figures (4.28) and (4.29). As theoretically predicted  $\beta$  comes out to be positive in the PDC region and negative in the NDC region. Similarly RTD response time is shorter in the PDC region and longer in the NDC region for both the biasing conditions (Fig. 4.28 and 4.29). In addition to them  $\beta = 0$  at the peak voltage  $V_p$  (Fig. 4.28 and 4.29).

The behaviors of response time ( $\tau_{resp}$ ) and quasi-bound-state ( $\tau_d$ ) lifetimes are different. With the increase in bias response time increases where as quasi-bound-state lifetime decreases.  $\tau_{resp}$  increases as a consequence of Coulomb interaction of electrons in the quantum well where as  $\tau_d$  decreases because of the increase in collector barrier tunnel transparency. Theoretical prediction [1, 44] was  $\tau_{resp} < \tau_d$  ( $\tau_{resp} > \tau_d$ ) in the PDC (NDC) region of the I-V curve. Our experiments and simulations (Fig. 4.28 and 4.29) confirms the theoretical results [1, 44].

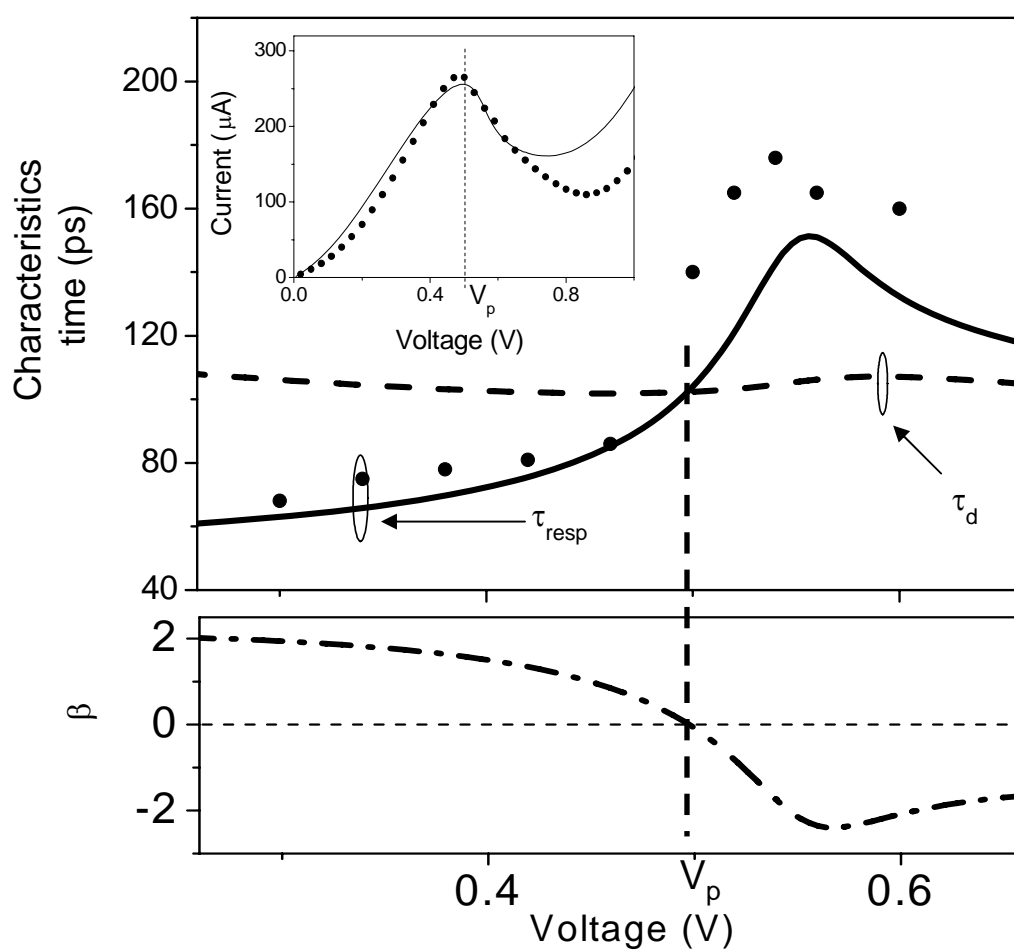


Figure 4.28: Comparison of measured and simulated response time when the device is in forward bias. The continuous lines are the outcome of the self-consistent simulation and the dots are the extracted values of response time by microwave measurement.

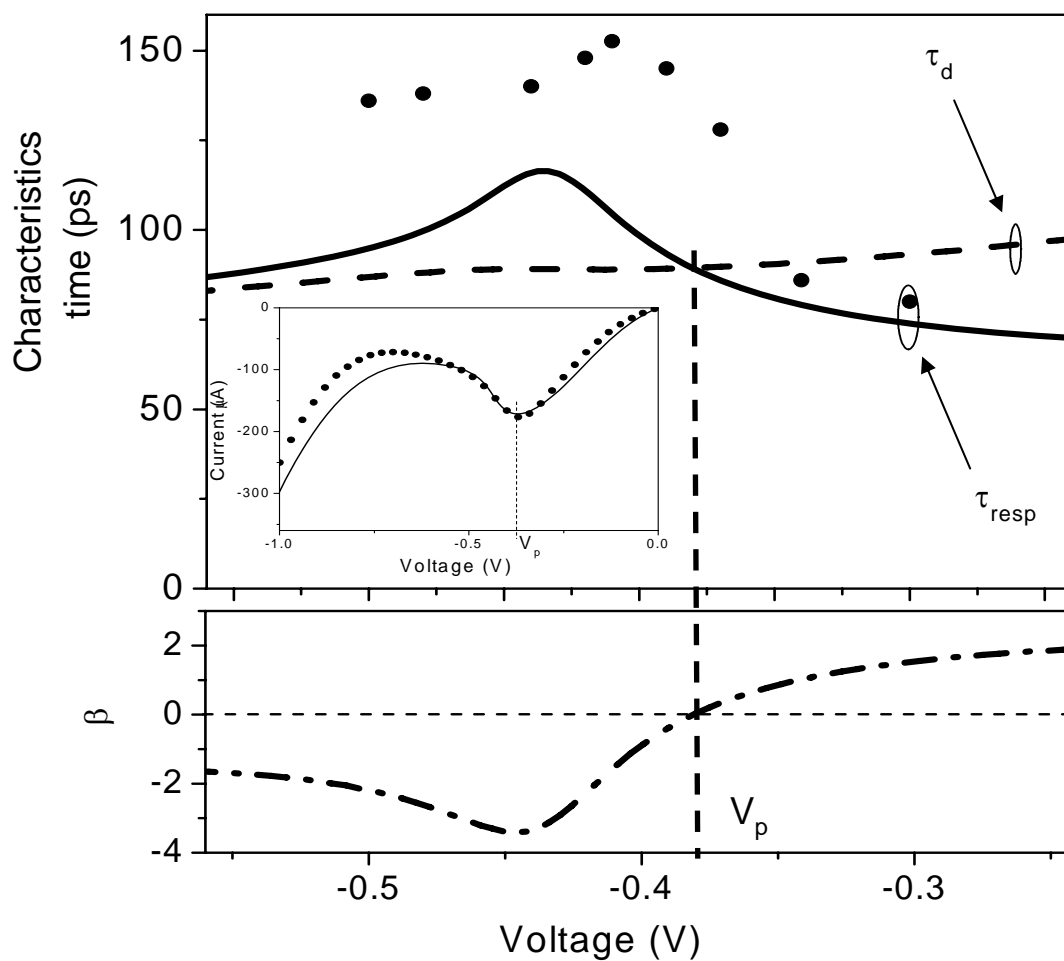


Figure 4.29: Comparison of measured and simulated response time in the reverse biasing conditions. The continuous lines are the outcome of the self-consistent simulation and the dots are measured response times.

## 4.8 RTD power at THz frequencies

The special feature of RTD is the presence of negative differential conductance (NDC) region in its I-V characteristic at room temperature. Because of that RTD can be used as the active element in the oscillator. It has been shown that RTD can produce oscillations at microwave frequencies [2, 22] when included into an RLC contour (a typical example of RLC contour is shown in Fig. 4.30a).

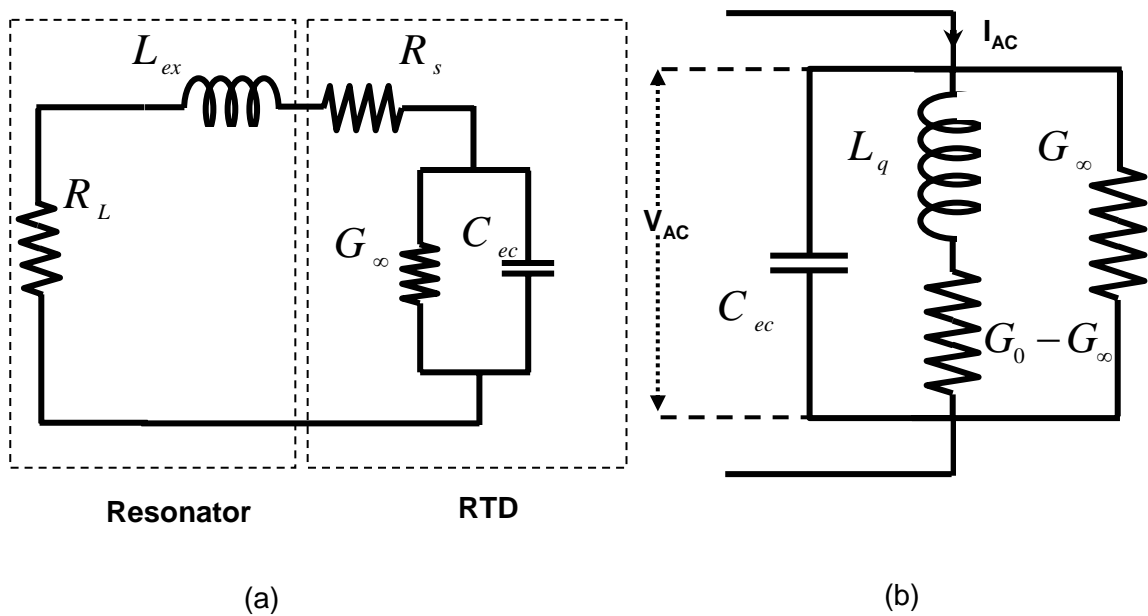


Figure 4.30: (a) Equivalent circuit representation of RTD along with the external resonator at high frequencies. At high frequencies, the external resonator contains inductance ( $L_{ex}$ ) and the load resistance ( $R_L$ ).  $R_s$ ,  $G_\infty$  and  $C_{ec}$  are the series resistance, high frequency conductance and emitter-collector capacitance of RTD respectively. (b) Intrinsic RTD equivalent circuit analytically derived before [1, 44] and used in this work for AC modelling.

Now let us examine the power generation capabilities of RTD. If  $I_{AC}$  is the AC current flowing through the diode and  $V_{AC}$  is the voltage drop across the diode (Fig. 4.30b), then the power generated or absorbed by the diode will be,

$$P_{RTD} = \frac{1}{2} \text{Re}(V_{AC} I_{AC}^*), \quad (4.6)$$

where  $I_{AC}^*$  is the complex conjugate of  $I_{AC}$ . Using the equivalent circuit for RTD (Fig. 4.30b), the obtained RTD power is,

$$P_{RTD} = \frac{1}{2} (\Delta V)^2 \left( \frac{G_0 + (\omega \tau_{resp})^2 G_\infty}{1 + (\omega \tau_{resp})^2} \right), \quad (4.7)$$

here  $\Delta V$  is the half of the peak to valley voltage swing. In the NDC region  $G_0$  is always negative, but  $G_\infty$  can be positive [36] or negative [37, 38] depending upon the RTD layer structures. If  $G_\infty$  is positive then RTD will absorb energy at high frequencies and in case of negative value of  $G_\infty$ , RTD is capable of energy generation at high frequencies.

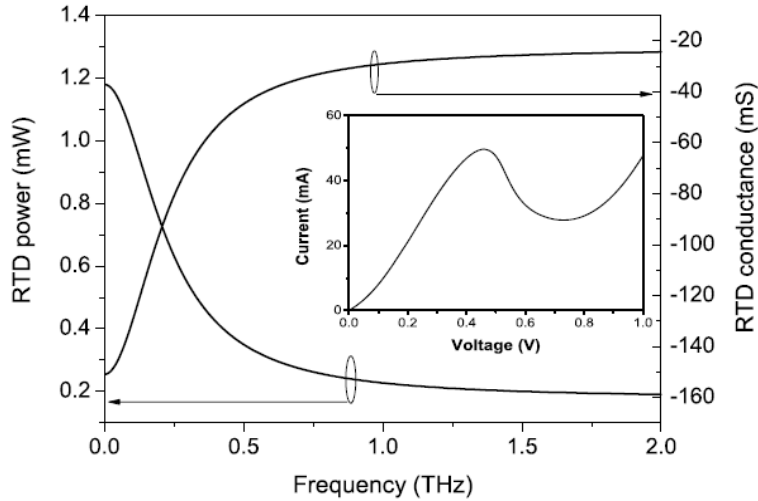


Figure 4.31: The real part of admittance (conductance) and the delivered power of a typical RTD which is similar to our batch of RTD2 except the barriers are 1.5 nm thick. Such diode should be able to deliver power  $\approx 0.2$  mW in the oscillatory mode at high frequencies. The inset shows the simulated current-voltage characteristic for the same diode.



When RTD is included into an RLC contour (a typical RLC contour is shown in Fig. 4.30a), oscillations can be produced if certain conditions are fulfilled. The primary condition for oscillation is the net conductance of RTD with the other circuit elements (the  $R_L$ ,  $L_{ex}$  and  $C_{ec}$  of the equivalent circuit in Fig. 4.30a) should be negative [71]. The resonator can produce oscillation till the conductance remains negative and the frequency beyond which the total conductance goes to positive values is called as resistive cut-off frequency. For the RLC contour shown in Fig. (4.30a), the resistive cut-off frequency is,

$$f_r = \frac{G^\infty}{2\pi C_{ec}} \sqrt{\frac{1}{(R_L + R_s) G^\infty} - 1}, \quad (4.8)$$

The frequency of oscillation ( $f_0$ ) when RTD is inserted into the resonator is the frequency at which the imaginary part of the admittance of the total circuit (i.e. the RLC contour along with the RTD) becomes zero [71]. So, the expression for the oscillatory frequency is,

$$f_o = \frac{1}{2\pi} \sqrt{\frac{1 - G^\infty(R_L + R_s)}{LC_{ec}} - \frac{1}{4} \left( \frac{C_{ec}(R_L + R_s) - G^\infty L}{LC_{ec}} \right)}, \quad (4.9)$$

If the circuit parameters can be reduced to as,  $C_{ec} = 5\text{fF}$ ,  $L_{ex} = 5\text{ pH}$  and  $R_s = 6\Omega$ , then the resistive cut-off frequency for the RTD would be 1.28 THz with the frequency of oscillation  $f_0 = 1.02\text{ THz}$ .

## 4.9 Conclusion

In this chapter, we describe the high frequency measurements of the fabricated RTDs using a conventional vector network analyzer upto 12 GHz of frequencies. Because of the presence of the metal lines around the diodes which lead to several parasitic elements, the actual RTD admittances are hidden. By measurement and simulation of the test structures (we call them as open and short devices) and the real devices, we were able to evaluate the parasitic contributions (i.e.  $C_{ex}$ ,  $L_x$  and  $R_s$  in Fig. 4.6). After knowing the parasitics, the intrinsic RTD admittances are extracted. The part of the measured RTD admittances, i.e. conductances and excess susceptances are reproduced well by simulation using the same RTD layer parameters as used for the static simulations. The dynamic simulations at several bias points taken from PDC and NDC region of both the biasing

conditions are done relying on the AC theory developed before [1, 44]. The measured roll-off frequency of conductances and the peak frequency of excess susceptances are the same for a particular bias point, as per theoretical prediction [1].

For our RTDs in the NDC region, the conductance rolled off from high negative values at low frequencies to low negative values at the high frequencies and remains negative for the whole range of frequencies. Hence the diodes demonstrated NDC at frequencies much higher than the inverse of the resonant state lifetime ( $\omega\tau_d \gg 1$ ) or the inverse of the intrinsic response time ( $\omega\tau_{resp} \gg 1$ ). Depending on the fact that RTD can have NDC beyond resonant state lifetime limit, we have shown by simulation that appropriately designed RTD should allow to achieve higher frequency than the best value obtained till now in the oscillatory mode [22].

We have demonstrated experimentally that it is the response time ( $\tau_{resp}$ ) which determines the AC characteristics of RTD rather than the quasi-bound-state lifetime ( $\tau_d$ ). Comparison of RTD intrinsic response time and quasi-bound-state lifetime reveals that they are changing even qualitatively differently with bias:  $\tau_d$  is decreasing because of the decrease in collector barrier height where as  $\tau_{resp}$  increases because of the Coulomb interaction effects as one goes from PDC to NDC region of the I-V characteristic. We have shown that the Coulomb interaction effect parameter ( $\beta$ ) rolls off from positive values to negative values when one goes from the PDC region to the NDC region of the I-V characteristics and  $\beta \rightarrow 0$ , at the peak voltage. Qualitatively, the positive value of  $\beta$  implies that Coulomb effect blocks electron flow across the emitter-well barrier resulting in  $\tau_{resp}$  shorter than the  $\tau_d$ . Where as negative values of  $\beta$  means enhancement of electron flow across the emitter-well barrier, which causes RTD to respond slowly with the applied bias variation (i.e.  $\tau_{resp} > \tau_d$ ). Intrinsic response time of RTD is experimentally evaluated using the fact that the pole frequency in admittances determines the RTD intrinsic response time and the values of the RTD response time determined in such a way, match well with the self-consistent simulations.

# Chapter 5

## Concluding Summary and Future Works

Finally, the major scientific results obtained during the course of this thesis work are summarized here. In addition to that, the possible scopes of further extension of the present work are also described.

### 5.1 Summary of results

In this thesis we have addressed various unsolved issues related to the working of RTD. The results are summarized as follows,

- We have experimentally demonstrated for the first time, the existence of negative differential conductance (NDC) at frequencies far beyond the resonant state lifetime limit. Our RTDs with frequency corresponding to the inverse of resonant state lifetime ( $1/2\pi\tau_d$ ) as  $\approx 1.2$  GHz, have shown NDC at frequencies upto 12 GHz (where  $\omega\tau_d \approx 10$ ). The existence of NDC at high frequencies clearly proves that resonant tunneling does exist beyond the resonant state lifetime limit and working frequency of RTD isn't limited by the electron lifetime in the QW resonant state. Depending upon the fact that NDC exists beyond resonant state lifetime limit, we have designed RTDs which should be able to deliver power at the THz frequencies.
- We have shown experimentally and using self-consistent simulation that the RTD response time ( $\tau_{resp}$ ) is different than the electron lifetime in the QW resonant state

( $\tau_d$ ) because of the Coulomb interaction effect. We have further shown Coulomb interaction effect parameter ( $\beta$ ) changes its sign from positive (in the PDC region) to negative values (in the NDC region). The bias dependent RTD response time determined by microwave measurements match well with the self-consistent simulations.

- The measured RTD admittances are reproduced well using the simple small signal RTD model theoretically developed before [1]. Since the model can reproduce the measured small signal behaviors of RTD very well at low and high frequencies, so we conclude that the theoretically developed model is correct and appropriate for small signal analysis of RTD. Existence of such simple and correct equivalent circuit for RTD should be highly beneficial to design circuits involving RTDs.
- The special properties of low frequency RTD capacitances are studied experimentally and by self-consistent simulation. We have obtained a simple analytical relationship for RTD capacitance in terms of the RTD parameters for the PDC region of I-V characteristic, depending upon the previously developed AC model [1]. Our simple analytical model at the low frequency limit can reproduce well the deviation of RTD capacitance from its geometrical capacitance. The fact that the deviation of RTD capacitance at low frequencies is reproduced well by the analytically developed AC model [1], once again confirms that the simple dynamic model [1] is correct and appropriate for AC analysis of RTD.
- We have modified the existing dynamic model [1] of RTD by considering the backflow of electron from collector to QW. This backflow of electron is significant in case of some RTDs found in the literatures [46, 51]. For such RTDs, we have shown that the intrinsic response time in the PDC region is even shorter compared to the usual ones. The deviation of effective low frequency RTD capacitance from the geometrical capacitance is always positive compared to the traditional ones because of the back injection of electrons from collector to the QW.

## 5.2 Future Works

Because of the time limitations in a thesis, several ideas for further investigations can not be implemented. At the same time many refinements of the pursued work are kept for future.

In this thesis work, the range of frequencies we have opted for is relatively low so that we can avoid the technical complications in measurements. Our main aim here was to establish the principle that resonant tunnelling is not limited by the electron lifetime in the quantum well. By appropriate arrangements of measurement set ups one should be able to observe the same effects (e.g. NDC at frequencies higher than inverse of resonant state lifetime, faster RTD response than resonant state lifetime etc.) at much higher frequencies and even in the THz range. The fact that the specially designed RTDs (with heavily doped collector) exhibit negative differential conductance beyond the inverse of the resonant state lifetime should allow one to break the maximum achieved oscillation frequency [22] till now. For the similar type of RTDs we have studied in this work, if the barrier thickness is decreased to  $\approx 1.5$  nm (corresponds to  $\tau_d \approx 0.65$  ps), the frequency corresponding to resonant state lifetime would be  $\approx 250$  GHz. Such device could be made to oscillate at frequencies higher than  $\approx 712$  GHz (the maximum oscillation frequency achieved to date [22]) if the technological difficulties and the limitations due to the parasitics are overcome.

In this work, we have extracted intrinsic response time of RTD by microwave measurements. The next step would be to make optical measurements (e.g. photo-response, photo-excitation, etc.) in order to demonstrate the difference in between RTD intrinsic response time ( $\tau_{resp}$ ) with the resonant state lifetime ( $\tau_d$ ). Existing theoretical model [1] for RTD is extended by considering the backflow of electron from collector to quantum well. For such RTDs, the intrinsic response time in the PDC region is even shorter. Further work would be to do the experimental verifications of the modified model and measurement of its intrinsic response time.

# Chapter 6

## Appendix

### 6.1 Derivation of emitter-well forward current

The emitter to well current in the forward direction is evaluated in the following way. In figure 6.1, we have considered that the QW is filled upto  $E_{fe}$ , whereas  $J_{\rightarrow}$  and  $J_{\leftarrow}$  are the current components across the emitter barrier in the forward and reverse directions, respectively.

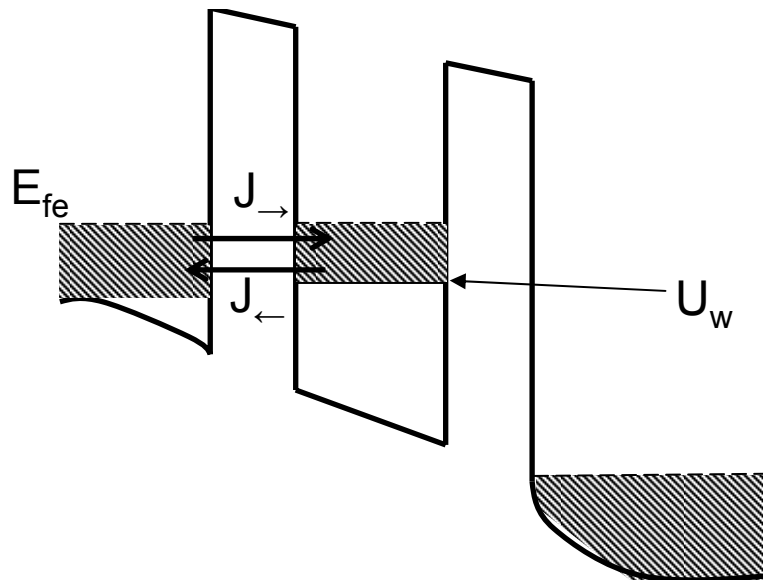


Figure 6.1: In this schematic, the QW is filled with electrons upto the Fermi level at the emitter ( $E_{fe}$ ).  $J_{\rightarrow}$  and  $J_{\leftarrow}$  are the current current components across the emitter-well barrier in the forward and reverse directions considering the QW is filled upto  $E_{fe}$ .

Since, Fermi level in the emitter and in the QW are considered to be the same, so the net current ( $J_T$ ) across the emitter barrier would be zero. That means,  $J_T = J_{\rightarrow} + J_{\leftarrow} = 0$  or  $J_{\rightarrow} = -J_{\leftarrow}$ . But,  $J_{\leftarrow} = eN\nu_e$ , where  $N$  is the number of electronic states in the QW, which are eligible for tunneling. Considering electrons obey Fermi-Dirac distribution function,

$$N = \int_{U_w}^{\infty} \rho_{2D} f_e(E) dE, \quad (6.1)$$

So,  $J_{\leftarrow}$  is,

$$J_{\leftarrow} = e \int_{U_w}^{\infty} \rho_{2D} f_e(E) \nu_e dE, \quad (6.2)$$

By magnitude  $J_{\leftarrow}$  is equal to  $J_{\rightarrow}$ . Hence, the current density in the forward direction across the emitter-well barrier is,

$$J_{ewF} = e \int_{U_w}^{\infty} \rho_{2D} f_e(E) \nu_e dE, \quad (6.3)$$

## 6.2 tunneling co-efficient calculation

Here, the way to calculate the tunneling co-efficient considering conservation of energy and momentum is shown. The conduction band structure of the barrier is shown in the figure (6.2). The expressions for the wave vectors in the z-direction (i.e.  $k_1$ ,  $k_2$  and  $k_3$ ) are as follows,

$$k_1^2 = \frac{2m_1 E_{z1}}{\hbar^2}, \quad (6.4)$$

$$k_2^2 = \frac{2m_2 (V_0 - E_{z2})}{\hbar^2}, \quad (6.5)$$

$$k_3^2 = \frac{2m_1 (E_{z3} + V_a)}{\hbar^2}, \quad (6.6)$$

where,  $E_{z1}$ ,  $E_{z2}$  and  $E_{z3}$  are the kinetic energy of the tunneling electron in the z-direction,  $k_i$  is the wave vector in the i-th region and  $m_i$  is the electron effective mass in the i-th region considering non-parabolicity. In figure (6.2),  $E_0$  is the position of the resonant state,  $V_0$  is the barrier height and  $a$  is the barrier width. We calculate the tunnel transparency of the barrier when an electron in the resonant state ( $E_0$ ) impinges on the barrier. After solving Schroedinger's equation in the z-direction, the expression for the tunneling co-efficient comes out to be,

$$D = \frac{4k_1 k_3 k_2^2}{k_2^2 (k_1 + k_3)^2 \cosh^2(k_2 a) + (k_2^2 - k_1 k_3) \sinh^2(k_2 a)}, \quad (6.7)$$

From the condition of conservation of total energy ( $E_T$ ) for the tunneling electrons,

$$E_T = E_{z1} + \frac{\hbar^2 k_{\perp}^2}{2m_1} = E_{z2} + \frac{\hbar^2 k_{\perp}^2}{2m_2} = E_{z3} + \frac{\hbar^2 k_{\perp}^2}{2m_1}, \quad (6.8)$$

Here, we are calculating tunneling co-efficient for the resonant electrons, that means the electrons for which the total energy (i.e.  $E_T$ ) and the momentum ( $k_{\perp}$ ) perpendicular to the plane of the barrier are conserved. So from equation (6.8) we get,

$$E_{z1} = E_{z3} = E_0, \quad (6.9)$$



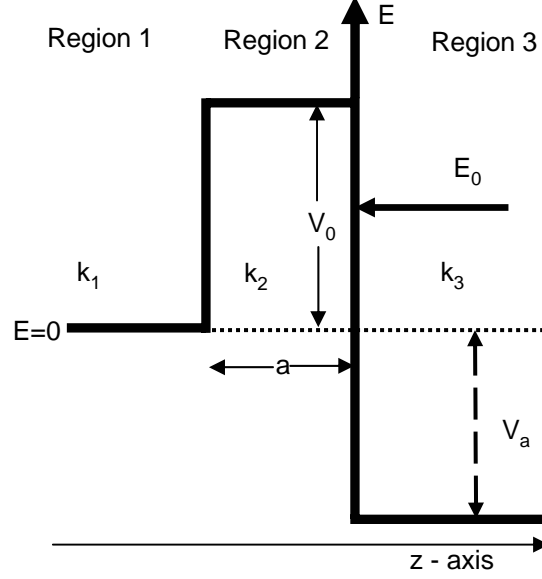


Figure 6.2: Conduction band profile of the barrier under the staircase approximation.  $V_a$  is the applied external bias and  $a$  is the thickness of the barrier.

Since, in region 3, energy of the electron in the  $z$ -direction is  $E_0$ . Using the relations for the wave vectors (equations 6.4, 6.5 and 6.6) and the relations for conservation of energy (i.e. equations 6.8 and 6.9), we get,

$$k_1^2 = \frac{2m_1 E_0}{\hbar^2}, \quad (6.10)$$

$$k_2^2 = \frac{2m_2 \left( V_0 - \left( E_0 + \frac{\hbar^2 k_1^2}{2} \left( \frac{1}{m_1} - \frac{1}{m_2} \right) \right) \right)}{\hbar^2}, \quad (6.11)$$

$$k_3^2 = \frac{2m_1 (E_0 + V_a)}{\hbar^2}, \quad (6.12)$$

The relation for  $k_2$  (6.11) can further be written using the condition for conservation of energy (i.e.  $E_T = E_0 + \frac{\hbar^2 k_{\perp}^2}{2m_1}$ ) as,

$$k_2^2 = \frac{2m_2}{\hbar^2} (V_0 - E_0) - \left( \frac{m_2}{m_1} - 1 \right) \frac{2m_1}{\hbar^2} (E_T - E_0), \quad (6.13)$$

Now let us check, if relation (6.13) can be approximated and represented by a simpler form. If for the tunneling electrons,  $k_{\perp} = 0$  (that means  $E_T = E_0$  in the barrier region),

the second term in the relation 6.13 goes to zero. For the electrons with total energy ( $E_T$ ) higher than  $E_0$ , the dispersion curve in the barrier region and at the emitter or well region (i.e. in the 1st or 3rd region in Fig. 6.2) deviates. The deviation is more as  $E_T$  increases from  $E_0$ . We further analyze the importance of this deviation on the wave vector at the barrier region (i.e.  $k_2$ ). For our structures  $E_{fe} = 0.08$  eV and the typical values of  $m_1$  and  $m_2$  are approximately 0.05 and 0.11 (considering non-parabolicity), respectively. So, in relation (6.13), the ratio of the second to the first term for the electron whose total energy is equal to  $E_{fe}$  (Fig. 6.3) is  $\approx 0.04$ .

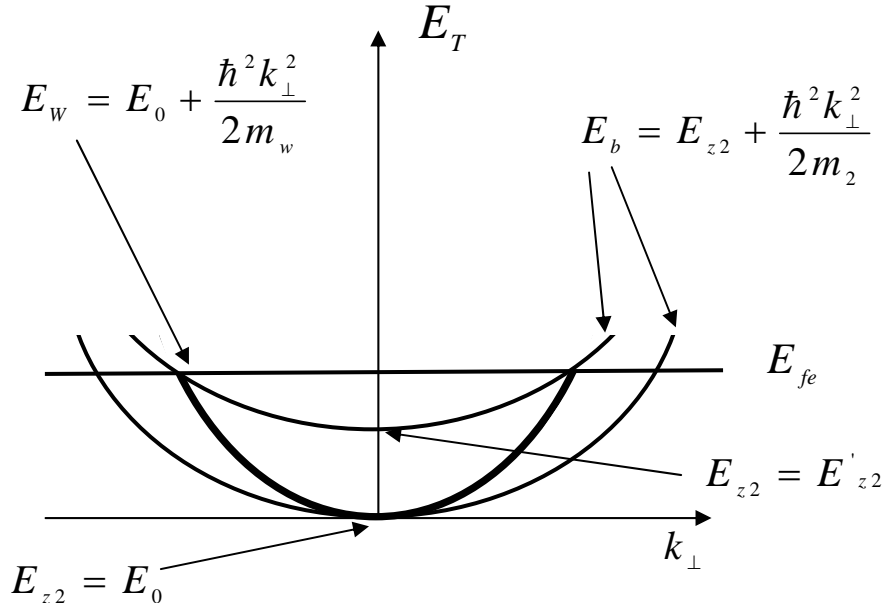


Figure 6.3: The energy dispersion curves for the QW and the barrier region. The bold line is the resonant states in the QW through which resonant tunneling is permissible. The thin lines are the energy dispersion curves for electrons inside the barrier. The kinetic energy of the tunneling electrons in the  $z$ -direction in the barrier region (i.e.  $E_{z2}$ ) differ as total energy ( $E_T$ ) changes.

In this scenario, if one neglects the second term in the relation for  $k_2$ , then the wave vector in the barrier region can be represented as,

$$k_2^2 = \frac{2m_2}{\hbar^2} (V_0 - E_0), \quad (6.14)$$

Next task is to determine, how much the barrier tunnel transparency is affected due to the different energy dispersion relations at the QW and barrier (Fig. 6.3). The calculated tunnel transparency (i.e.  $D$  in relation 6.7) for the electron whose total energy  $E_T$  is equal to  $E_{fe}$  using the general expression for  $k_2$  (relation (6.13) is  $\approx 2.48 \times 10^{-5}$ . For the same electron, the calculated tunnel transparency ( $D$ ) using the simplified expression for  $k_2$  (i.e. relation 6.14) is  $2.34 \times 10^{-5}$ . So, the difference in tunneling co-efficient is  $\approx 6\%$  for the tunneling electrons whose total energy deviate maximum (i.e.  $E_T = E_{fe}$ ) from the bottom of the 2D subband in the QW ( $E_0$ ).

In this work, the analytical relations 6.10, 6.12 and 6.14 are used to calculate the tunneling co-efficient across the barrier. For more precise calculation one should use the relation 6.13 for  $k_2$ . In that case the tunneling co-efficient calculation should be done by using numerical method.

### 6.3 tunneling co-efficient when effective masses are different

In this section, we calculate the tunneling co-efficient of emitter barrier when the electron effective mass in the emitter ( $m_e$ ), barrier ( $m_b$ ) and well ( $m_w$ ) are different. The one dimensional (i.e. in the z-direction) Schroedinger's equation for the above mentioned three regions are as follows,

$$\frac{\partial^2 \phi_{1z}}{\partial z^2} + k_{1z}^2 \phi_{1z} = 0, \quad (6.15)$$

$$\frac{\partial^2 \phi_{2z}}{\partial z^2} + k_{2z}^2 \phi_{2z} = 0, \quad (6.16)$$

$$\frac{\partial^2 \phi_{3z}}{\partial z^2} + k_{3z}^2 \phi_{3z} = 0, \quad (6.17)$$

$\phi_{iz}$  and  $k_{iz}$  are the wave-function and the wave vector in the z-direction at the i-th region. The wave vectors (i.e.  $k_{iz}$ ) are,

$$k_{1z}^2 = \frac{2m_1 E_{1z}}{\hbar^2}, \quad (6.18)$$

$$k_{2z}^2 = \frac{2m_2 (V_0 - E_{2z})}{\hbar^2}, \quad (6.19)$$

$$k_{3z}^2 = \frac{2m_3 (U_w + V_a)}{\hbar^2}, \quad (6.20)$$

$E_{1z}$ ,  $E_{2z}$  and  $U_w$  are the energy in the z-direction in the i-th region.  $V_0$  is the barrier height and  $V_a$  is the applied voltage across the barrier (Fig. 6.4).

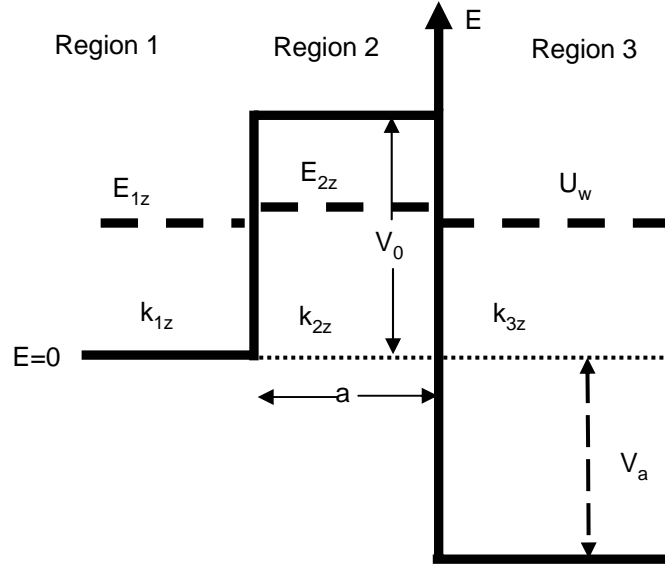


Figure 6.4: Conduction band profile of the barrier under the staircase approximation.  $V_a$  is the applied external bias and  $a$  is the thickness of the barrier.

After solving Schroedinger's equation at the three regions, the expression for tunneling co-efficient is derived as,

$$D = \frac{4k_1 k_3 k_2^2}{k_2^2 (k_1 + k_3)^2 \cosh^2(k_2 a) + (k_2^2 - k_1 k_3) \sinh^2(k_2 a)}, \quad (6.21)$$

The wave vectors  $k_{iz}$ s depend on the energy at the three regions. Now we will do some algebra and will use the resonant conditions to represent the wave vectors in terms of the total energy ( $E$ ).

From the condition of total energy,

$$E_{1z} + \frac{\hbar^2 k_{\perp}^2}{2m_1} = E_{2z} + \frac{\hbar^2 k_{\perp}^2}{2m_2} = U_w + \frac{\hbar^2 k_{\perp}^2}{2m_3}, \quad (6.22)$$

With the help of the relation 6.22, the relations for the wave vectors (i.e. 6.18 - 6.20) can further be represented as,

$$k_{1z}^2 = \frac{2m_1 \left( U_w + \frac{\hbar^2 k_{\perp}^2}{2} \left( \frac{1}{m_3} - \frac{1}{m_1} \right) \right)}{\hbar^2}, \quad (6.23)$$

$$k_{2z}^2 = \frac{2m_2 \left( V_0 - \left( U_w + \frac{\hbar^2 k_{\perp}^2}{2} \left( \frac{1}{m_3} - \frac{1}{m_2} \right) \right) \right)}{\hbar^2}, \quad (6.24)$$

$$k_{3z}^2 = \frac{2m_3(U_w + V_a)}{\hbar^2}, \quad (6.25)$$

But the total energy ( $E$ ) is related to  $U_w$  with the following dispersion relation,

$$E = U_w + \frac{\hbar^2 k_{\perp}^2}{2m_3}, \quad (6.26)$$

So, the relations for wave vector in the  $i$ -th region (i.e.  $k_i$ ) can be further represented in terms of total energy ( $E$ ) using relation 6.26 as,

$$k_{1z}^2 = \frac{2m_1}{\hbar^2} \left( E \left( 1 - \frac{m_3}{m_1} \right) + U_w \frac{m_3}{m_1} \right), \quad (6.27)$$

$$k_{2z}^2 = \frac{2m_2}{\hbar^2} \left( V_0 - \left( U_w \frac{m_3}{m_2} + E \left( 1 - \frac{m_3}{m_2} \right) \right) \right), \quad (6.28)$$

$$k_{3z}^2 = \frac{2m_3(U_w + V_a)}{\hbar^2}, \quad (6.29)$$

So, in this way the wave vectors are transformed in terms of total energy ( $E$ ). And used in relation (6.21) to calculate the tunneling co-efficient.

# List of Symbols

$C_{ew}$	emitter-well capacitance of RTD
$C_{wc}$	well-collector capacitance of RTD
$C_{ec}$	emitter-collector capacitance
$C_{ex}$	Parasitic external capacitance
$E_c$	Bottom energy level of the conduction band
$E_F$	Fermi level
$E_{fe}$	Fermi level position in the emitter
$E_{fw}$	Fermi level position in the quantum well
$E_{fc}$	Fermi level position in the collector
$E_g$	Band gap in a semiconductor
$E_v$	Top energy level of the valence band
$k_B$	Boltzmann constant
$L_s$	Parasitic series inductance around the diode
$N_D$	Doping concentration of a donor-doped semiconductor
$Q_e$	2 degree Charge density in the emitter
$Q_w$	2 degree Charge density in the quantum well
$Q_c$	2 degree Charge density in the collector
$R_s$	Series resistance of the diode
$q$	Electron charge
$T$	Absolute temperature
$\epsilon_0$	Permittivity of free space
$\epsilon_r$	Relative permittivity of a material

# List of Abbreviations

<i>3D</i>	Three Dimensional
<i>2DEG</i>	Two Dimensional Electron Gas
<i>C – V</i>	Capacitance-Voltage
<i>CST</i>	Computer Software Technology
<i>EMS</i>	Electro Magnetic Studio
<i>I – V</i>	Current-Voltage
<i>IHF</i>	Department of Microwave Engineering at TUD
<i>LO – phonon</i>	Longitudinal-Optical Phonon
<i>MBE</i>	Molecular Beam Epitaxy
<i>MWS</i>	Microwave Studio
<i>AlGaAs</i>	Aluminium Gallium Arsenide
<i>GaAs</i>	Gallium Arsenide
<i>GHz</i>	Giga Hertz
<i>InAs</i>	Indium Arsenide
<i>InP</i>	Indium Phosphide
<i>PVCR</i>	Peak to Valley Current Ratio
<i>RF</i>	Radio Frequency
<i>RT</i>	Room Temperature
<i>RTD</i>	Resonant Tunneling Diode
<i>TE</i>	Thermionic Emission
<i>THz</i>	Tera Hertz
<i>TUD</i>	Technical University of Darmstadt
<i>XRD</i>	X-Ray Diffraction Study

# Bibliography

- [1] M. N. Feiginov, “Displacement currents and the real part of high-frequency conductance of the resonant-tunneling diode,” *Applied Physics Letters*, vol. 78, p. 3301, 2001.
- [2] E. R. Brown, C. D. Parker, and T. C. L. G. Sollner, “Effect of quasibound-state lifetime on the oscillation power of resonant tunneling diodes,” *Applied Physics Letters*, vol. 54, p. 934, 1989.
- [3] T. C. L. G. Sollner, E. R. Brown, W. D. Goodhue, and H. Q. Le *Physics of Quantum Electron Devices ed. F Capasso (New York:Springer)*, p. 147, 1989.
- [4] J. P. Sun, G. I. Haddad, P. Mazumder, and J. N. Schulman, “Resonant tunneling diodes: Models and properties,” *Proceedings of the IEEE*, vol. 86, p. 641, 1998.
- [5] H. Mizuta and T. Tanoue *The physics and applications of Resonant Tunnelling Diodes*, 2005.
- [6] S. Datta *Electronic Transport in Mesoscopic Systems*, 1995.
- [7] S. Luryi, “Frequency limit of double-barrier resonant-tunneling oscillators,” *Applied Physics Letters*, vol. 47, p. 490, 1985.
- [8] R. Tsu and L. Esaki, “Tunneling in a finite superlattice,” *Applied Physics Letters*, vol. 22, p. 562, 1973.
- [9] T. C. L. G. Sollner, P. E. Tannenwald, D. D. Peck, and W. D. Goodhue, “Quantum well oscillators,” *Applied Physics Letters*, vol. 45, 1984.



- [10] K. Mutumba, A. Sigurdardottir, A. Vogt, H. L. Hartnagel, and E. H. Li, "A comparative study of uniaxial," *Applied Physics Letters*, vol. 72, 1998.
- [11] D. B. Janes, K. J. Webb, M. S. Carroll, G. E. Starnes, K. C. Huang, J. Shenoy, and M. R. Melloch, "Direct current and microwave characterization of integrated resonant tunneling diodes," *Journal of Applied Physics*, vol. 78, 1998.
- [12] E. R. Brown, T. C. L. G. Sollner, C. D. Parker, W. D. Goodhue, and C. L. Chen, "Oscillations up to 420 ghz in gaas/alas resonant tunneling diodes," *Applied Physics Letters*, vol. 55, p. 1777, 1989.
- [13] T. Daniels-Race and S. Yu *Solid state Electronics*, vol. 38, 1995.
- [14] R. C. Bowen, G. Klimeck, R. K. Lake, W. R. Frensley, and T. Moise, "Quantitative simulation of a resonant tunneling diode," *Journal of Applied Physics*, vol. 81, 1997.
- [15] W. Y., N. Y., I. K., and T. M. *International Electron Devices Meeting, Technical Digest*, p. 475, 1992.
- [16] T. P. E. Broekaert, W. Lee, and C. G. Fonstad, "Pseudomorphic  $\text{in}_{0.53}\text{ga}_{0.47}\text{as}/\text{alas}/\text{inas}$  resonant tunneling diodes with peak-to-valley ratios of 30 at room temperature," *Applied Physics Letters*, vol. 53, p. 1545, 1988.
- [17] J. H. Smet, T. P. E. Broekaert, and C. G. Fonstad, "Peak-to-valley current ratios as high as 50:1 at room temperature in pseudomorphic  $\text{in}_{0.53}\text{ga}_{0.47}\text{as}/\text{alas}/\text{inas}$  resonant tunneling diodes," *Journal of Applied Physics*, vol. 71, 1992.
- [18] T. S. Moise, Y. C. Kao, A. J. Katz, T. P. E. Broekaert, and F. G. Celli, "Experimental sensitivity analysis of pseudomorphic ingaas/alas resonant-tunneling diodes," *Journal of Applied Physics*, vol. 78, 1995.
- [19] J. R. Söderström, D. H. Chow, and T. C. McGill, "New negative differential resistance device based on resonant interband tunneling," *Applied Physics Letters*, vol. 55, p. 1094, 1989.
- [20] J. R. Söderström, E. R. Brown, C. D. Parker, L. J. Mahoney, J. Y. Hao, T. G. Andersson, and T. C. McGill, "Growth and characterization of high current density,

- high-speed inas/alsb resonant tunneling diodes,” *Applied Physics Letters*, vol. 58, p. 275, 1991.
- [21] E. R. Brown, W. D. Goodhue, and T. C. L. G. Sollner, “Fundamental oscillations up to 200 ghz in resonant tunneling diodes and new estimates of their maximum oscillation frequency from stationary-state tunneling theory,” *Journal of Applied Physics*, vol. 64, p. 1519, 1988.
- [22] E. R. Brown, J. R. Söderström, C. D. Parker, L. J. Mahoney, K. M. Molvar, and T. C. McGill, “Oscillations up to 712 ghz in inas/alsb resonant-tunneling diodes,” *Applied Physics Letters*, vol. 58, p. 2291, 1991.
- [23] N. Orihashi, S. Hattori, and M. Asada, “Millimeter and submillimeter oscillators using resonant tunneling diodes with stacked-layer slot antennas,” *Japanese Journal of Applied Physics*, vol. 43, p. L1309, 2004.
- [24] N. Orihashi, S. Hattori, S. Suzuki, and M. Asada, “Voltage-controlled sub-terahertz oscillation of resonant tunnelling diode integrated with slot antenna,” *Electronics Letters*, vol. 41, p. 872, 2005.
- [25] N. Orihashi, S. Suzuki, and M. Asada, “One thz harmonic oscillation of resonant tunnelling diodes,” *Applied Physics Letters*, vol. 87, p. 233501, 2005.
- [26] T. C. L. G. Sollner, E. R. Brown, W. D. Goodhue, and C. A. Correa, “Harmonic multiplication using resonant tunneling,” *journal of applied physics*, vol. 64, p. 4248, 1988.
- [27] A. Rydberg and H. Grönqvist, “Quantum-well high-efficiency millimetre-wave frequency tripler,” *IEE Electronics letters*, vol. 25, p. 348, 1989.
- [28] S. K. Diamond, E. özbey, M. J. W. Rodwell, D. M. Bloom, Y. C. Pao, and J. S. Harris, “Resonant tunneling diodes for switching applications,” *Applied Physics Letters*, vol. 54, p. 153, 1988.
- [29] E. özbey, D. M. Bloom, D. H. Chow, and J. N. Schulman, “1.7-ps, microwave, integrated-circuit-compatible inas/alsb resonant tunneling diodes,” *IEEE Electron Device Letters*, vol. 14, p. 400, 1993.

- [30] J. F. Whitaker, G. A. Mourou, T. C. L. G. Sollner, and W. D. Goodhue, "Picosecond switching time measurement of a resonant tunneling diode," *Applied Physics Letters*, vol. 53, p. 385, 1988.
- [31] J. Robertson, T. Ytterdal, W. C. B. Peatman, R. S. Tsai, E. R. Brown, and M. Shur, "Rtd/2-d mesfet/rtd logic elements for compact, ultra low-power electronics," *IEEE Transactions on Electron Devices*, vol. 44, p. 1033, 1997.
- [32] F. Capasso and R. A. Kiehl, "Resonant tunneling transistor with quantum well base and high-energy injection: A new negative differential resistance device," *Journal of Applied Physics*, vol. 58, p. 1366, 1985.
- [33] F. Capasso, S. Sen, A. Y. Cho, and D. Sivco, "Resonant tunneling devices with multiple negative differential resistance and demonstration of a three-state memory cell for multiple-valued logic applications," *IEEE Electron Device Letters*, vol. EDL-8, p. 297, 1987.
- [34] J. P. A. V. D. Wagt, A. Seabaugh, and E. A. Beam, "Rtd/hfet low standby power sram gain cell," *IEEE Electron Devices Letters*, vol. 19, p. 7, 1998.
- [35] A. A. Lakhani, R. C. Potter, and H. S. Hier, "11-bit parity generator with a single, vertically integrated resonant tunnelling device," *Electronics Letters*, vol. 24, p. 681, 1988.
- [36] J. P. Mattia, A. L. Mcwhorter, R. J. Aggarwal, F. Rana, E. R. Brown, and P. Maki, "Comparison of a rate-equation model with experiment for the resonant-tunneling diode in the scattering-dominated regime," *Journal of Applied Physics*, vol. 84, p. 1140, 1998.
- [37] D. R. Chowdhury and M. Feiginov, "Resonant tunneling diode: intrinsic response time vs. quasi-bound-state lifetime," *Workshop on Compound Semiconductor Devices and Integrated Circuits (WOCSDICE)*, p. 195, 2007.
- [38] M. Feiginov and D. R. Chowdhury, "Operation of resonant-tunneling diodes beyond resonant-state-lifetime limit," *Applied Physics Letters*, vol. 91, p. 203501, 2007.

- [39] J. M. Gering, D. A. Crim, D. G. Morgan, P. D. Coleman, W. Kopp, and H. Morkoc, "A small-signal equivalent-circuit model for  $\text{GaAs-Al}_x\text{Ga}_{1-x}\text{As}$  resonant tunneling heterostructures at microwave frequencies," *Journal of Applied Physics*, vol. 61, p. 271, 1987.
- [40] T. Wei, S. Stepleton, and O. Berolo, "Scattering parameter measurements of resonant tunneling diodes up to 40 GHz," *IEEE Transactions on Electron Devices*, vol. 42, p. 1378, 1995.
- [41] L. Eaves, M. L. Leadbeater, D. G. Hayes, E. Alves, F. W. Sheard, G. A. Toombs, P. E. Simmonds, M. S. Skolnick, M. Henini, and O. H. Hughes, "Electrical and spectroscopic studies of space-charge buildup, energy relaxation and magnetically enhanced bistability in resonant tunneling structures," *Solid-state Electronics*, vol. 32, p. 1101, 1989.
- [42] F. W. Sheard and G. A. Toomb, "Space charge effects and ac response of resonant tunneling double-barrier diodes," *Solid-state Electronics*, vol. 32, p. 1443, 1989.
- [43] J. Genoe, C. Van Hoof, W. Van Roy, J. H. Smet, K. Fobelets, R. P. Mertens, and G. Borghs, "Capacitances in double-barrier tunneling structures," *IEEE Transaction on Electron Devices*, vol. 38, p. 2006, 1991.
- [44] M. N. Feiginov, "Does the quasibound-state lifetime restrict the high-frequency operation of resonant-tunnelling diodes?," *Nanotechnology*, vol. 11, p. 359, 2001.
- [45] J. S. Scott, J. P. Kaminski, M. Wanke, S. J. Allen, D. H. Chow, M. Lui, and T. Y. Liu, "Terahertz frequency response of an  $\text{In}_{0.53}\text{Ga}_{0.47}\text{As}/\text{AlAs}$  resonant-tunneling diode," *Applied Physics Letters*, vol. 64, p. 1995, 1994.
- [46] Q. Liu, A. Seabaugh, P. Chahal, and F. J. Morris, "Unified ac model for the resonant tunneling diode," *IEEE Transaction on Electron Devices*, vol. 51, p. 653, 2004.
- [47] M. N. Feiginov, "Effect of coulomb interaction on the response time and impedance of the resonant-tunneling diodes," *Applied Physics Letters*, vol. 76, p. 2904, 2000.
- [48] W. Shockley, "Currents to conductors induced by a moving point charge," *Journal of Applied Physics*, vol. 9, p. 635, 1938.

- [49] S. Ramo, "Currents induced by electron motion," *Proceedings of the I.R.E.*, vol. 27, p. 584, 1939.
- [50] J. P. Mattia, E. R. Brown, A. R. Calawa, and M. J. Manfra, "Small-signal admittance and switching measurements of the resonant-tunneling diode," *Applied Physics Letters*, vol. 63, p. 521, 1993.
- [51] U. Auer, W. Prost, G. Janssen, M. Agethen, R. Reuter, and F. J. Tegude, "A novel 3-d integrated hfet/rtd frequency multiplier," *IEEE Journal of selected topics in Quantum Electronics*, vol. 2, p. 650, 1996.
- [52] L. L. Chang, L. Esaki, and R. Tsu, "Resonant tunneling in semiconductor double barriers," *Applied Physics Letters*, vol. 24, p. 593, 1974.
- [53] J. N. Schulman, H. J. D. L. Santos, and D. H. Chow, "Physics-based rtd current-voltage equation," *IEEE Electron Device Letters*, vol. 17, p. 220, 1996.
- [54] H. C. Liu, "Resonant tunneling through single layer heterostructures," *Applied Physics Letters*, vol. 51, p. 1019, 1987.
- [55] V. J. Goldman, D. C. Tsui, and J. E. Cunningham, "Evidence of lo-phonon-emission-assisted tunneling in double-barrier heterostructures," *Physical Review B*, vol. 36, p. 7635, 1987.
- [56] E. R. Brown, O. B. McMahon, L. J. Mahoney, and K. M. Molvar, "Spice model of the resonant-tunnelling diode," *Electronics Letters*, vol. 32, 1996.
- [57] Z. Yan and M. J. Deen, "New rtd large-signal dc model suitable for pspice," *IEEE Transaction On Computer-aided Design of Integrated Circuits and Systems*, vol. 14, p. 167, 1995.
- [58] C. E. Chang, P. M. Asbeck, K.-C. Wang, , and E. R. Brown, "Analysis of heterojunction bipolar transistor/resonant tunneling diode logic for low-power and high-speed digital applications," *IEEE Transactions on Electron Devices*, vol. 40, p. 685, 1993.
- [59] J. W. Matthews and A. E. Blakeslee, "Defects in epitaxial multilayers. i. misfit dislocations," *Journal of Crystal Growth*, vol. 27, p. 118, 1974.

- [60] O. Madelung *Semiconductors-Basic Data*, 1996.
- [61] D. J. Paul, "Si/sige heterostructures: from material and physics to devices and circuits," *Semiconductor Science and Technology*, vol. 19, p. R75, 2004.
- [62] I. Vurgaftman, J. R. Meyer, and L. R. Ram-Mohan, "Band parameters for *iii - v* compound semiconductors and their alloys," *Journal of Applied Physics*, vol. 89, p. 5815, 2001.
- [63] M. Cahay, M. McLennan, S. Datta, and M. S. Lundstrom, "Importance of space-charge effects in resonant tunneling devices," *Applied Physics Letter*, vol. 50, p. 612, 1987.
- [64] F. W. Sheard and G. A. Toomb, "Space-charge buildup and bistability in resonant-tunneling double-barrier structures," *Applied Physics Letters*, vol. 52, 1988.
- [65] E. Tourne, P. Grunberg, C. Fouillant, A. Baranov, A. Joullie, and K. H. Ploog *Solid-State Electronics*, vol. 37, 1994.
- [66] H. Ohno, E. E. Mendez, and W. I. Wang, "Effects of carrier mass differences on the current-voltage characteristics of resonant tunneling structures," *Applied Physics Letters*, vol. 56, p. 1793, 1990.
- [67] J. N. Schulman, "Extension of tsu-esaki model for effective mass effects in resonant tunneling," *Applied Physics Letters*, vol. 72, p. 2829, 1998.
- [68] N. V. Alkeev, S. V. Averin, A. A. Dorofeev, P. Velling, E. Khorenko, W. Prost, and F. J. Tegude *Semiconductors*, vol. 41, 2007.
- [69] M. Feiginov and D. R. Chowdhury, "Resonant tunnelling diodes beyond quasi-bound-state lifetime limit," *SPIE Proceedings*, vol. 6892, p. 68920D, 2008.
- [70] T. A. Weiland, "A numerical method for the solution of the eigenwave problem of longitudinally homogeneous waveguides," *Electronics and Communication*, vol. 31, p. 308, 1977.
- [71] W. F. Chow *Principles of Tunnel Diode Circuits*, 1964.

## Own publications

- Dibakar Roy Chowdhury and Michael Feiginov: "Resonant Tunnelling Diodes: intrinsic response time vs. quasi-bound-state lifetime", 31<sup>st</sup> Workshop on Compound Semiconductor Device and Integrated Circuits held in Europe (WOCSDICE-2007), Venice, Italy, May 20-23, 2007.
- Michael Feiginov and Dibakar Roy Chowdhury: "Operation of Resonant Tunnelling Diode beyond resonant state lifetime limit", Applied Physics Letters, 91, 203501 (2007);
- Michael Feiginov and Dibakar Roy Chowdhury: "Resonant Tunnelling Diode beyond Quasi-bound-state lifetime limit", SPIE Symposium on Integrated Optoelectronic Devices 2008, 19-24 January 2008;
- Michael Feiginov and Dibakar Roy Chowdhury: "Resonant-Tunelling diodes beyond quasi-bound lifetime limit", Proceedings SPIE, 6892, 68920D (2008);
- Michael Feiginov and Dibakar Roy Chowdhury: "Experimental demonstration of Resonant Tunnelling Diode operation beyond resonant state lifetime limit", International Conference on the Physics of Semiconductors, 27th July - 1st August 2008;
- Dibakar Roy Chowdhury and Michael Feiginov: "Study of small signal behavior of Resonant Tunneling Diode", Manuscript under preparation

# Curriculum Vitae

## Personal Data

Name: Dibakar Roy Chowdhury

Date of Birth: 06.08.1976

Place of Birth: India

## Occupation History

1984-1995: Middle School, India

1995-1998: Durgapur Government College, India

1998-2000: Department of Physics  
Rani Durgavati Vishwavidyalaya, Jabalpur University, India.

2000-2001: Indian Institute of Technology, Bombay, India.

2001-2003: Indian Institute of Technology, Madras, India.

2002-2003: studentship with DAAD scholarship  
Technical University of Darmstadt, Darmstadt, Germany.

2003-2008: PhD-student at Dept. of Microwave Engineering  
Technical University of Darmstadt, Germany.